

THREE-DIMENSIONAL OUTCROP MODELLING, SEDIMENTOLOGY, AND
LITHOLOGY OF THE FALHER D MEMBER, NORTHEAST BRITISH COLUMBIA,
CANADA

by

Arzu Acikelli

A thesis submitted in partial fulfillment of the requirements for the degree of

Master of Science

Department of Earth and Atmospheric Sciences
University of Alberta

© Arzu Acikelli, 2022

ABSTRACT

The Lower Cretaceous Falher Member is an important hydrocarbon reservoir in the Deep Basin of Alberta and British Columbia. Owing to its economic importance, it has been the subject of many studies. However, there remains contention on the depositional interpretation of individual Falher Member conglomerate units. Both shoreface and wave-dominated deltaic models have been proposed. As such, the Falher Member is an ideal outcrop analogue that can be used to assess the spatial distribution of component lithofacies and sedimentary features of shoreface and wave-dominated delta deposits.

The present research uses sedimentology and ichnology, within the context of 3D photogrammetric models, of several Falher-equivalent outcrop successions on Mount Spieker in northeastern British Columbia. Facies distributions and relationships are assessed through 3D outcrop models and collected field data. The presence of fluid mud lenses, terrestrial fossil fragments, and impoverished suites of trace fossils confirm that the study interval was deposited proximal to a fluvial sediment source. The abundance of HCS sandstone units and pebbly storm lags indicates robust storm-wave reworking at the time of deposition. The along-strike heterogeneity in facies distribution is interpreted as evidence for delta asymmetry. The proposed depositional model suggests that strong longshore currents were the main reason for delta asymmetry. In this wave-dominated deltaic setting, the updrift side presents better reservoir targets including thick, clast-supported conglomerate units. The downdrift side consists of finer grained argillaceous deposits representing poorer reservoir quality. This study documents the sedimentology of the studied outcrops and discusses the depositional processes causing the heterogeneity in facies type and distribution in a wave-dominated, gravel-dominated delta setting.

PREFACE

This thesis is an original work by Arzu Acikelli. No part of this thesis has been previously published.

DEDICATION

This thesis is dedicated to my family; Bülent Açıkkelli, Gönül Açıkkelli, Günay Açıkkelli Uzuner, Çisil Açıkkelli and Gökhan Uzuner. I am thankful for your endless love, support, and encouragement.

Thank you for giving me wings to fly after my dreams.

“There are no facts, only interpretations.”

- Friedrich Nietzsche

ACKNOWLEDGEMENT

I feel blessed with the people who accompanied me during my Canada journey. First I would like to thank my supervisors Drs Murray Gingras and John-Paul Zonneveld for accepting me as a student in the Ichnology Research Group. In addition thank them for creating a team environment within the group, and encouraging us to share our cultural backgrounds (i.e. baklavas). Also, it was a huge pleasure to learn about Canadian culture (crib tournaments, Christmas events, Halloween treats, casseroles, camping under the snow, eggnogs, smores, raisin tarts ...), I enjoyed it all. Even though I became a competitive skunked in crib games...I learned a lot in geology from my supervisors, but also thanks to their patience in teaching me academic writing. Specifically thanks to Murray for never making us feel alone and JP for the understanding of any issue I came up with. I was also so lucky to do my fieldwork with an amazing geologist crew including Sara Biddle, Skye Lybbert, Scott Melnyk, and Brette Harris. Thank you all so much for taking the time to help me to collect data. I would like to thank my first Canadian friend here Maya Lagrange Rao for always taking time for fun stuff, having tea times and walks, always being available to share happy and sad moments, and being on my side when I needed. You helped me a lot during my adaptation to this new environment, I am so thankful for that. Also thank you for understanding “What I do not understand” all the time, you are very smart no doubt. My friends and officemates Maria Rodriguez and Riley Morton are also very special to me thank you for all dinners, night-outs, listening to my worries, and geology discussions that I could have with you without any hesitation. Our office will be my favorite office forever. The newly developed IGOD group members made my Canada journey colorful as well so I thank each member. Thanks to Dr. Carolyn Furlong for giving me positive feedback and supervising me whenever I needed it. Thanks, Mark Labbe and Igor Jakab for helping me with any subject whenever I needed it. Thanks to Marilyn Huff for helping me with how to use a microscope camera on different computers. Thanks to Melissa Dhillon for all the support and information that she provided me. Also thanks to Sana Quarishi, and Dean Zaragoza for the fun time that I had during front desk duties. Thanks to my committee members Drs Sasha Wilson and Jeffrey Kavanaugh. Thanks to the Ministry of Education of Turkey for awarding me with this generous scholarship. The last and big thank is to my family; without their unconditional love and support, I could not achieve any of my goals, I am so lucky to have you.

TABLE OF CONTENTS

ABSTRACT	ii
PREFACE	iii
DEDICATION	iv
ACKNOWLEDGEMENT	vi
CHAPTER 1 : Introduction	1
1.1 General Overview	1
1.2 Palaeogeographic Setting	5
1.3 Study Area and Data Set	6
1.4 Organization of Thesis	7
CHAPTER 2 : Wave Dominated Delta Architecture Refined with Photogrammetric Models	8
2.1 Introduction	8
2.2 Regional Stratigraphy and Study Area	9
2.3 Methodology	14
2.4 Results	20
2.4.1 West Ridge	27
2.4.2 East Ridge	33
2.4.3 South Ridge	37
2.5 Interpretations	41
2.5.1 Facies Associations	41
2.5.2 Facies Interpretations	45

Facies 1	45
Facies 2	46
Facies 3	46
Facies 4	47
Facies 5	47
Facies 6	48
Facies 7	49
Facies 8	50
Facies 9	50
Facies 10	51
2.6 Ichnofacies Interpretations -West, East, and South Ridges	51
2.6.1 Ichnofacies Interpretation of Distributary Mouth Facies Association (FA1)	54
2.6.2 Ichnofacies Interpretation of Delta Front Facies Association (FA2)	54
2.6.3 Ichnofacies Interpretation of Prodelta Facies Association (FA3)	55
2.6.4 Overall Ichnofacies Distribution	57
2.7 Orientation Interpretations	60
2.7.1 West Ridge	60
2.7.2 East Ridge	60
2.7.3 South Ridge	60
2.8 Discussion -Wave-dominated delta asymmetry	61
2.9 Conclusion	65
 CHAPTER 3 : Storm-Wave Orbital Diameter Calculations from Photogrammetric Datasets	66
3.1 Introduction	66

3.2 Study Area and Methods	66
3.3 Results and Interpretation.....	68
3.4 Discussion	73
3.5 Conclusion.....	74
CHAPTER 4: Conclusion.....	75
BIBLIOGRAPHY	76
APPENDIX I: X-RAY DIFFRACTION RESULTS – IRONSTONE	96
APPENDIX II: ORIENTATION MEASUREMENTS M&K VALUES	100
APPENDIX III: PHOTOMOSAICS	105

LIST OF TABLES

CHAPTER 1

Table 1.1. Study locations GPS Coordinates.....	7
--	---

CHAPTER 2

Table 2.1. Study locations-GPS Coordinates	14
Table 2.2. Summary of facies described in Falher D parasequence observed at Mount Spieker outcrops. ((a): abundant, (m): moderate, (r): rare)	22
Table 2.3. Summary of facies associations described in Falher D parasequence observed at Mount Spieker outcrops.	42
Table 2.4. <i>List of trace fossils, morphologies, ethologies, and environmental indications and observed on Falher D outcrops.</i>	52

CHAPTER 3

Table 3.1. Study locations GPS Coordinates.....	68
Table 3.2. <i>West Ridge– Hummocky cross-stratification wavelength and amplitude measurements in low-angle planar-laminated silty-sandstone facies (F7) and highly bioturbated silty-sandstone (F6).</i>	70
Table 3.3. <i>East Ridge – Hummocky cross-stratification wavelength and amplitude measurements in low-angle planar-laminated silty-sandstone facies (F7) and highly bioturbated silty-sandstone (F6).</i>	71
Table 3.4. <i>South Ridge – Hummocky cross-stratification wavelength and amplitude measurements in low-angle planar-laminated silty-sandstone facies (F7) and muddy sandstone facies (F8).</i>	72

LIST OF FIGURES

CHAPTER 1

Figure 1.1. Lower Cretaceous Albian stratigraphic chart (Smith et al., 1984). 10-1-70-11W6 gamma-ray log on the right shows coarsening upward parasequences separated by coal spikes from Falher A through H (after Smith et al., 1984; Zonneveld and Moslow, 2004).2

Figure 1.2. The location map showing outcrop study area. The Cordilleran terranes shown on the map. The stratigraphic chart presents the Gates Formation equivalent Members (modified from Leckie, 1985).3

Figure 1.3. Google Earth satellite image of study area; measurement locations are labelled with yellow stars (W: West Ridge, E: East Ridge, S: South Ridge)6

CHAPTER 2

Figure 2.1. Lower Cretaceous Albian stratigraphic chart (Smith et al., 1984). 10-1-70-11W6 gamma-ray log on the right shows coarsening upward parasequences separated by coal spikes from Falher A through H (after Smith et al., 1984; Zonneveld and Moslow, 2004). 12

Figure 2.2. Location map showing the Deep Basin and the location of the outcrop study area at Mount Spieker (Caddel and Moslow, 2004). Note that excellent exposure of Falher C, D and F equivalent stratigraphic successions occurs are Mount Spieker, and mounts Bullmoose, Chamberlin (Leckie and Walker, 1982; Leckie, 1985b; Moslow and Schink, 1995; Moslow, 1998; Caddel, 1999; Caddel and Moslow, 2004; Zonneveld and Moslow, 2004). 13

Figure 2.3. Google Earth satellite image of study area; measurement locations are labelled with yellow stars (W: West Ridge, E: East Ridge, S: South Ridge). 13

Figure 2.4. Flow chart presents stages of building a 3D model via Agisoft Metashape Software. SfM and MVS algorithm-based stages are indicated (modified from Hayes et al., 2017). 16

Figure 2.5. T matrix is used to calculate coordinates of best-fit center of mass of plane, proposed by Woodcock, 1997. 18

Figure 2.6. Table shows varying **M** and **K** values and corresponding α and θ values. In figure (a) there are evenly distributed nodes (marker points) around a center of mass which represents a best fit plane. α and θ values are representing alignment of best fit plane in two different directions. Table (b) shows corresponding **M** to varying θ values; if all marker points are distributed homogenously below and above mean plane which corresponds case of $\alpha=180^\circ$, Table (c) shows **K** value correlation with varying α values in case of all points are equidistant from center of mass and distributed homogenously with angle of $\theta=2^\circ$ (Fernandez, 2005). 19

Figure 2.7. Lithofacies photographs and under PPL photomicrographs of facies listed on Table 1. **A)** Photograph of polymodal, poorly-sorted, sand-matrix-supported conglomerate (**F1**), white bar scale 1.50 cm in length. **B)** Photograph of bimodal grain-supported, open-framework, conglomerate facies (**F2**), black Jacob’s staff: each part is 10.00 cm in length. **C)** Photomicrograph of upper-fine to medium-grained, well-sorted sandstone facies with coal

fragments (F3), arrow points the coal fragment (Co) D) Photomicrograph of locally conglomeratic, well-sorted, upper-fine to medium-grained sandstone facies showing cross stratification (F4) E) Photomicrograph of very well-sorted, medium-grained, swaley cross-stratified, sandstone facies (F5) F) Photomicrograph of highly-bioturbated very fine- to fine-grained sandstone (F6), arrow points clean quartz lining of Schaubcylindrichnus isp. Burrow (Sch). G) Photomicrograph of low-angle planar-laminated, moderately-sorted, very fine- to fine-grained sandstone facies (F7) H) Moderately-sorted, fine-grained sandstone facies (F8), arrow points organic laminae (OL). I) Mudstone facies (F9), arrow points abundant micro plant fragments (PF) J) Brownish, reddish-colored ironstone nodule (F10). The bar scale for photomicrographs is 1.00 mm.20

Figure 2.8. Rose and equal area stereonet plots representing palaeoflow directions for West, East and South ridges respectively. West and East Ridge measurements indicate eastwards dominant palaeoflow on the other hand South Ridge measurements indicate westwards dominant palaeoflow.27

Figure 2.9. Lithologic strip logs representing facies thicknesses measured on West Ridge. From section A (basinward) to section B (landward) decrease in the abundance of sandy facies is observable.29

Figure 2.10. Photomosaics of West Ridge which are ~ 180m in width. A) West Ridge photomosaic with tadpole plots (see Appendix II) indicating dominantly NW dip direction. Landward decrease in the average dip amount is observable. B-C) Facies shading and interpretation of photomosaic; orange-dashed lines represent lithofacies contacts (FC), green-lines representing master bedding planes (MB), red-dashed lines representing foreset laminae (FL), and. Orange arrows indicating delta clinofolds dip direction and yellow lines represents fault plane. D) Close-up image of the area shown by rectangle; the contact between the cross bedded conglomerate facies (F2) and the massive conglomerate facies (F1), foreset laminae are traced with red-dashed lines and clinofold dip directions are indicated with orange arrows. Note that sandstone facies abundance slightly increasing basinward (North).30

Figure 2.11. Outcrop photos and interpreted sketches of facies observed on the West Ridge. A-A') Low angle planar laminated (HCS) silty-sandstone facies with high angle internal truncation surfaces (ITS), pebbly-storm lags aligned through swale laminae. B-B') Swale (Sw) and hummock (Hm) structures indicating HCS deposited under storm conditions. Pebbly-laminae interpreted as storm lags (SL) deposited at peak energy levels of storm events. C-C') shows scoured bottom contact (SB) of conglomerate facies (F1) with underlying bioturbated sandstone facies. Abundant soft sedimentary deformational structures (SSDS) due to sudden deposition of conglomeratic units caused fluid escape and remobilization of underlying sandstones (F7). D-D') Abundant soft sedimentary deformational structures and gutter casts at F1-F7 contact indicating deposition under sediment gravity flows. E-E') Massively bedded conglomerate facies (F1) interbedded with swaley sandstone facies (F5) interpreted as tempestite couplets each representing a single storm event. Upper conglomerate bed (F1) shows inverse grading representing wax stage of storm event. F) Abundant fossil wood fragments preserved at sandstone (F7) and conglomerate facies (F1) contact. G) Discontinuous lenses of poorly sorted

storm lags. **H-H'**) Planar laminated to massive bedded structure of conglomerate facies (**F1**). Zebra stick is 20.00 cm and black Jacob's staff is 10.00 cm each part in length.....32

Figure 2.12. Lithologic strip log representing facies thicknesses measured on East Ridge outcrop. Compared to West Ridge increase in the abundance of sandy facies is observable (Symbols and lithofacies patterns as in legend in Fig. 2.9).....34

Figure 2.13. Photomosaics of East Ridge outcrop. **A)** Photomosaic shows tadpole measurements indicating SE and NW directed dip directions. This measurements inconsistency resulted by folding of the ridge. **B)** Facies shading of East Ridge outcrop, eastwards increasing abundance of sandstone lenses is observable. Gray hatched parts are covered with vegetation. The legend indicating facies colors is provided on the right. **C)** Interpreted photomosaic of East Ridge; green lines represent bedding contacts, orange dashed line represents facies contacts and red lines showing foreset laminae. Conglomerate facies thicknesses decreased compared to west ridge on the other hand sandstone facies (**F6-F7**) show an increase in thickness (**FC:** Facies Contacts, **FL:** Foreset Laminae, **MB:** Master Bedding surfaces)35

Figure 2.14. Photograph and sketch of Lam-scam bedding observed on East Ridge indicating fair-weather or waning storm conditions (scam) prevailing after strong storm events (lam). Scoured contact surface between conglomerate facies (**F1**) and bioturbated sandstone facies indicating deposition by sediment laden gravity flows formed during major storms resulted in river flooding. Soft sedimentary deformational structures and gutter casts are observable locally along contact surface. Orange dashed line represents facies contacts. Stick is 1.50 meters in length.....36

Figure 2.15. Lithologic strip logs representing facies thicknesses measured on South ridge outcrops. On South Ridge, conglomerate abundance is lowest. This site is different than the west and east outcrop successions. Mudstone, ironstone lenses and the stratigraphic section is capped by terminal distributary channel deposits. Overall facies showing low to no bioturbation unless cryptically bioturbated (Symbols and lithofacies patterns as in legend in Figure 2.9).38

Figure 2.16. Photomosaics of South Ridge outcrops. **A)** Tadpole plots located on ridge indicating measurements taken from masterbedding surfaces. **B)** Facies shading observed on South Ridge. Legends are provided on right. gray hatch represents vegetation cover and fragmented block of rocks. **C)** Interpreted version of photomosaic master bedding planes are indicated with green lines, red lines show foreset laminae and orange dashed line represents facies contacts.39

Figure 2.17. Selected facies photos and interpretation sketches from South Ridge outcrop. **A-A')** Swaley cross stratified sandstone (**F5**) overlain by conglomeratic sandstone dunes (**F4**), **F4** is half a meter in thickness. Conglomeratic sandstone dunes are overlain by subaqueous terminal distributary channel sandstone (**F3**) with a scoured contact. **B-B')** Swaley cross stratified sandstones with pebbly storm lags and internal erosion surfaces due to erosional storm bed amalgamation. Zebra stick is 10.00 cm in length. **C-C')** Massive conglomerate facies (**F1**) erosively overlies muddy sandstone facies (**F8**); ironstone lens is observable within delta front conglomerate facies (**F1**) overlain by **HCS** sandstones (**F7**) black Jacob's stick is 10.00 cm in length for each part.....40

Figure 2.18. Selected trace fossils observed on outcrop. **A)** Bedding plane perpendicular view of selective deposit feeding polychaete burrow *Macaronichnus* isp. (Clifton and Thompson, 1978). (Ma) Burrows showing monospecific assemblage locally. **B)** Truncated vertical cone of clay-silt material filled burrow of *Rosselia* isp. (Ro) in sandy substrate, burrow truncation indicate erosive storm amalgamation. **C)** *Macaronichnus* isp. burrows (Ma) (or *Paramacaronichnus*), organic laminae (OgL), *Schaubcylindrichnus* isp. burrows. **D-E)** *Diplocraterion* isp. (Di) vertical U-shaped spreiten burrows. *Diplocraterion* isp.; dwelling burrow of a suspension-feeding organism (Fürsich, 1947). **F)** *Macaronichnus* isp. (Ma) (or *Paramacaronichnus*), and *Diplocraterion* isp. (Di) burrows.58

Figure 2.19. Selected photomicrographs and interpretations of facies representing *Cryptic*-bioturbated intervals with less than a mm thick, sinuous, vertical to horizontally aligned and quartz filled (grain selective) burrows. Bar scale is 1.00 mm in length.59

Figure 2.20. Tripartite model showing delta geometries changing related to relative energies of shallow marine processes (Galloway, 1975).63

Figure 2.21. Model shows deflection of river mouth from symmetric to asymmetric due to strong longshore transport outpacing groin effect of river (Li et al., 2011).63

Figure 2.22. Model shows deflection of river mouth from symmetric to asymmetric due to longshore transport. Vertical sections representing hypothetical palaeo-depositional locations of West, East, and South ridges (modified from Bhattacharya et al., 2003) Downdrift deflection of river mouth is caused by longshore currents. Gray facies represent conglomerate and yellow represents sandstone.64

CHAPTER 3

Figure 3.1. Location map showing the Deep Basin and the location of the outcrop study area at Mount Spieker (Caddel et al., 2004). Note that excellent exposure of Falher C, D and F equivalent stratigraphic successions occurs are Mounts Spieker, Bullmoose and Chamberlin (Leckie and Walker, 1982; Leckie 1985b; Moslow and Schink, 1995; Moslow, 1998; Caddel, 2000; Caddel and Moslow, 2004; Zonneveld and Moslow, 2004).67

Figure 3.2. Google Earth satellite image of study area; measurement locations are labelled with yellow stars (W: West Ridge, E: East Ridge, S: South Ridge).68

Figure 3.3. HCS illustration showing order of surfaces (modified from Harms et al., 1975).69

Figure 3.4. Figure shows the measurements performed on West Ridge facies **F7** and **F6** (M1: Measurement 1, M2: Measurement 2).70

Figure 3.5. Figure shows the measurements performed on East Ridge facies **F7** and **F6** (M1: Measurement 1, M2: Measurement 2, M3: Measurement 3).71

Figure 3.6. Figure shows the measurements performed on South Ridge facies **F8** and **F7** (M1: Measurement 1, M2: Measurement 2, M3: Measurement 3).72

Figure 3.7. Diagram shows wave orbital diameter vs. HCS wavelength change (Yang and Dalrymple et al., 2006).73

Figure 3.8. Graph showing wave orbital diameter values (x-axis) plotted against elevation (y-axis) values. Measurement elevations increase corresponds to shallowing in depth. The shallower depths represent higher wave orbital diameter values. Red line: East Ridge measurements, Blue line: West Ridge measurements, Green line: South Ridge measurements. ...74

CHAPTER 1 : Introduction

1.1 General Overview

During the Early Mesozoic, convergence along the western margin of North America was initiated and several composite terranes were accreted to the ancient continental margin (Price, 1981; Porter et al., 1982; Monger, 1989; Leckie and Smith, 1992). The resultant thrust sheets loaded the western edge of the North America craton resulting in flexural subsidence and a foreland basin that formed on the eastern margin of the orogen (Wright et al., 1994). The foreland basin, which forms the most recent phase of the Western Canadian Sedimentary Basin (WCSB) consists of a series of eastward thinning, westerly sourced, clastic wedges representing periods of tectonic reactivation of rising Cordillera (Monger and Price, 2002). The sedimentary fill of the basin is up to 4000 m thick, with the thickest sedimentary fill occurring near the western margin closest to the Cordillera. The sediment filling is dominantly terrigenous with shale, fine to medium sandstone and granule-pebble conglomerate facies (Cant, 1983). In the WCSB, two tectonic structures affected regional sedimentation patterns via uplift and subsidence: (1) the northwesterly positioned Peace River Arch (DeMille, 1958; Cant 1988; O'Connell et al., 1990) and the southerly Sweetgrass Arch (Lorenz, 1982; Podruski, 1988).

The Gates Formation, which is the stratigraphic outcrop equivalent of the Falher and Notikewin members of the Spirit River Formation (Fig. 1.1), comprises a major part of one of the clastic wedges that formed during Early to Middle Cretaceous (Bullhead and Fort. St John groups). The Gates Formation consists of a series of laterally continuous transgressive- regressive cycles (Leckie, 1985). Palaeoshoreline trends of Gates Formation were approximately northwest - southeast with a northward dipping palaeoslope. Within the Gates interval fluvial sources are evident given the abundance of conglomeratic facies.

The Gates Formation is further subdivided into the Torrens and Grand Cache Members and some authors have informally assigned outcrop units of the Gates Formation to the Falher A through H and Notikewin Members (Leckie, 1983; Zonneveld and Moslow, 2004).

Leckie (1985), investigated the provenance of the Gates Formation with petrographic methods. Moosebar-Gates sandstone beds are described as litharenites to felspathic arenites sourced by clastic, carbonate sedimentary rocks and plutonic, volcanic, and igneous rocks. The

sediment source area is defined as Omineca Crystalline Belt to eastern Margins of the Intermontane Belt (Figure 1.2) (Leckie, 1985).

The Falher Member of the Spirit River Formation is one of the most important natural gas reservoirs of Deep Basin of west-central Alberta (Masters, 1984; AEUB, 1999). Outcrop analyses of the Gates Formation aid in understanding the depositional history of the Falher Member in the subsurface of western Alberta (Leckie and Walker, 1982; Leckie 1985; Moslow and Schink, 1995; Moslow, 1998; Caddell, 1999; Caddell and Moslow, 2004; Zonneveld and Moslow, 2004).

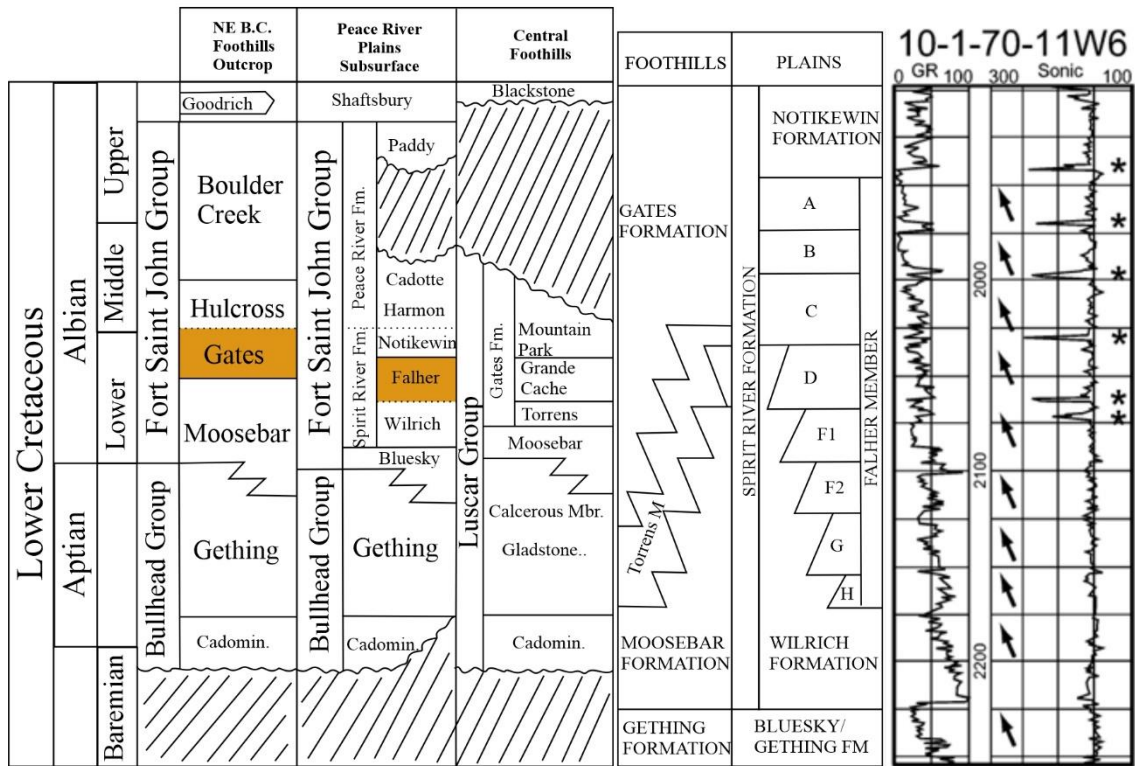


Figure 1.1. Lower Cretaceous Albian stratigraphic chart (Smith et al., 1984). 10-1-70-11W6 gamma-ray log on the right shows coarsening upward parasequences separated by coal spikes from Falher A through H (after Smith et al., 1984; Zonneveld and Moslow, 2004).

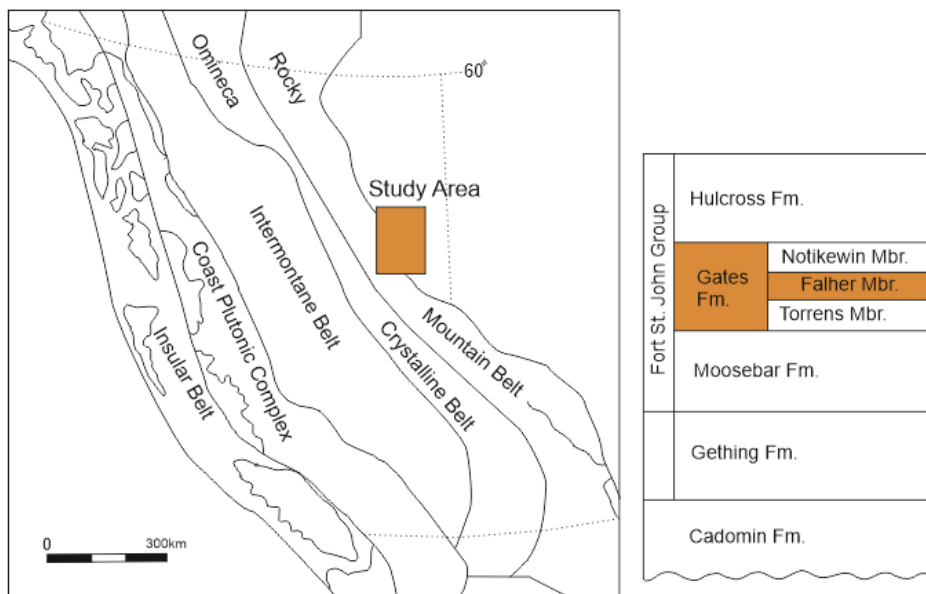


Figure 1.2. The location map showing outcrop study area. The Cordilleran terranes shown on the map. The stratigraphic chart presents the Gates Formation equivalent Members (modified from Leckie, 1985).

The Falher Member was first described by Badgely (1952) and the Alberta Study Group (1954) as a shaly, silty, sandy unit with thin coal bed and conglomeratic intervals. The Falher Member was subdivided into 5 units as Falher A to F (Cant, 1984; Leckie, 1986; Casas and Walker, 1997) and later older (stratigraphically lower) Falher trends were identified as Falher G-I (Zonneveld and Moslow, 2004). More recently, the letter terminology has been extended to include the Falher, which represents a number of lower, older and more southern shoreline successions (Newitt, 2017; Newitt and Pedersen, in press). Each unit represents a coarsening upward progradational succession (Cant, 1984) and they are accepted as related groups of parasequences or parasequence sets (i.e., Arnott, 1993; Casas and Walker, 1997).

Owing to the economic importance of the Falher D Member, it has been the subject of many investigations. Leckie, 1982 investigated sedimentology and proposed a depositional model for Falher sandstones and conglomerates outcropping south of Fort St. John. Leckie used orientation, geometry and texture data to differentiate fluvial, beach, offshore bars and storm conglomerates of the Gates Formation (Leckie, 1982). The sequence stratigraphy and sedimentology of Falher D was documented by Casas and Walker, 1997 where the unit was divided into D1 through D5

sub-cycles. Hoffman, 2008 investigated the Falher D sedimentology and proposed an asymmetrical delta model using subsurface dataset.

The paleogeographic interpretations agree that the deposition occurred along an arcuate, east-west trending palaeo-shoreline of a shallow epeiric sea situated to the north (Stott, 1968; Leckie and Walker, 1982). Although shoreface (Cassas and Walker, 1997) and deltaic (Leckie and Walker, 1982; Arnott, 1983; Hoffman, 2008) interpretations of conglomerate facies are still subject to debate, and in fact are both likely correct in different areas.

The reservoir characteristic of the sandstone and conglomerate facies have also been presented in several studies. The gas prone Falher Member presents moderate porosity and permeability values (Leckie and Walker, 1982; Cant and Ethier, 1984). The sandstone facies porosity ranges between 9-12% and permeability values between 0.001 to 0.1mD (Cant, 1983; Cant and Ethier, 1984). The major reasons for low porosity and permeability values of sandstone facies documented are (1) quartz overgrowths, (2) mechanical compaction of rock fragments, (3) clay and carbonate cementation. The sandstone reservoir facies are accordingly thought to be tight - unconventional due to their low porosity and permeability values.

Additionally, there are 3 types of conglomerate intervals reported: (1) unimodal open framework, (2) bimodal clast supported, and (3) bimodal sandy matrix supported (Cant and Ethier, 1984). The textural differences in between conglomerate units were considered as the main reason for variation in porosity and permeability values. For example, unimodal-open framework conglomeratic intervals locally constitute conventional reservoirs and are associated with high permeability values. The presence of drusy quartz cement has in some instances prevented the occlusion of pore throats (Cant and Ethier, 1984) due to compaction. However, in practice reservoir performance of facies depends on (1) depositional process-controlled lithology variations and (2) the diagenetic processes that accompanied sediment burial (Cant, 1984).

The specific objectives of this study are (1) to develop and analyze 3D models supported with field observations to interpret facies, and facies variations, (2) to propose a depositional model, and (3) predict reservoir distribution for Falher D Member in light of the depositional model considered. The proposed model and interpretations should contribute to a better understanding of reservoir facies distributions in the Falher Member and help to better understand the palaeogeography of this economically important unit.

1.2 Palaeogeographic Setting

In the early Cretaceous, the tectonic uplift of the Cordillera, and concomitant flexural subsidence to the east, formed the asymmetrical Western Canada Foreland Basin of western Alberta and northeast British Columbia (Wright et al., 1994; Monger and Price, 2002). The associated foredeep is informally referred to as the Alberta “Deep Basin” (Wright et al., 1994; Monger and Price, 2002) and produced a unique, inverted hydrocarbon trap. During the Barremian, alluvial fan and braided fluvial deposits, preserved as the Cadomin Formation, were deposited in the axially-drained Deep Basin, west of the Fox Creek Escarpment (McLean, 1977; Schultheis and Mountjoy, 1978). Erosional lowering of the Cordillera, combined with continued basin subsidence, allowed for deposition and preservation of a thick succession of heterolithic sediments deposited in meandering fluvial and deltaic settings, preserved as the Aptian to Albian Gething formation (Stott 1973; Smith et al., 1984).

Marine transgressions towards the south and regressions towards the north during the Albian resulted from expansion and contraction of the shallow epeiric Boreal Sea, which covered north-eastern British Columbia, much of Alberta, and west-central Saskatchewan (Williams and Stelck, 1975). These flooding events are evidenced by the coastal and marine-deposited sandstone units of the Gething Formation and the overlying Bluesky and Moosebar Formation / Wilrich Member of the Spirit River Formation. The Moosebar / Wilrich transgression resulted in deposition of a thick succession of dark, organic-rich silty shale deposited during the interval of maximum depth and southward extent of the Boreal Sea (Stelck and Kramers, 1980). Increased sediment input outpaced the rise of sea level / basin subsidence during the middle-early Albian resulting in rapid regional progradation of the south shore of the Boreal Sea towards the north (Jackson, 1984; Smith et al., 1984). During middle-early Albian time, coastal/deltaic sediments of the Falher Member downlapped onto and interfingered with Moosebar / Wilrich Formation shales (Stelck and Kramers, 1980; Smith et al., 1984). Each Falher sub-member represents an apparent marine transgression followed by a regression caused by combined effect of basin subsidence and intermittent sediment supply changes. The overall architecture of the lower Falher members (Falher R through H) is strongly progradational, whereas the Falher G through A and Notikewin members comprise an overall aggradational succession (Zonneveld and Moslow, 2000; Newitt, 2017; Newitt and Pedersen in press).

1.3 Study Area and Data Set

This study focusses on medial Gates Formation outcrop located at Mount Spieker in northeastern British Columbia. Three different outcrop sections were studied, and these are referred to as the West, East, and South ridges (Fig. 1.3) (Table 1.1). In addition to conventional field techniques including measuring sections and lithological descriptions, UAV-Based photogrammetry was used to document the outcrops in detail and produce 3D models in this study. This technique is helpful to visualize large outcrops and collecting large numbers of orientation data (e.g., Tavani et al., 2013; Hayes et al., 2018; Nesbit et al., 2018; Bilmes et al., 2019).

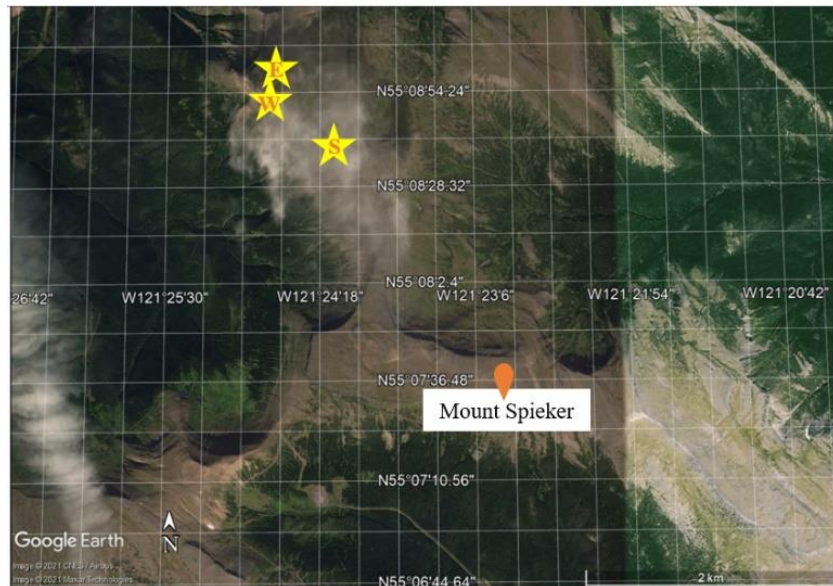


Figure 1.3. Google Earth satellite image of study area; measurement locations are labelled with yellow stars (W: West Ridge, E: East Ridge, S: South Ridge)

Table 1.1. Study locations GPS Coordinates

Ridge	GPS Coordinates
West Ridge	N55° 08' 53.0" W121° 24' 41.2"
East Ridge	N55° 08' 58.3" W121° 24' 38.0"
South Ridge	N55° 08' 36.4" W121° 24' 09.0"

1.4 Organization of Thesis

Thesis is subdivided into 4 chapters including the Conclusion and the Introduction.

The subject and the content of each part are summarized below:

- **Chapter 2** focuses on sedimentology and ichnology interpretation of outcrop intervals within the context of UAV-based photogrammetry method. Dip and strike measurements from different intervals of stratigraphic section were performed. The rose plots indicating palaeocurrent flow were constructed based on data collected from foreset laminae orientation measurements. The delta clinofolds representing northward progradation are traces on photomosaics. Ten individual lithofacies described and depositional processes are interpreted. The evidences of deltaic interpretation of Falher D deposits were documented. The reasons of facies heterogeneity and impoverished to absent distribution of trace fossils along the palaeoshoreline are discussed. A depositional model explaining the facies distribution along Falher D shoreline is proposed.

- **Chapter 3** focuses on shallowing upwards variation of HCS- wavelength and amplitude in a deltaic setting. The wave orbital diameters were calculated by formula by inserting wavelength and amplitude values obtained through measurements performed on photomosaics.

CHAPTER 2 : Wave Dominated Delta Architecture Refined with Photogrammetric Models

2.1 Introduction

Fluvial and marine-sourced sediment influx are modified by fair-weather and storm-wave reworking and transport of those sediments resulting in distinct shoreline geometries (Galloway, 1975; Coleman and Wright, 1975; Bhattacharya and Giosan, 2003). Interpretation of palaeo-shoreline morphology requires lateral and vertical understanding of facies patterns including lithofacies distribution and geometry (Bhattacharya, 2006). This paper focuses on facies interpretation and reconstruction of depositional environments to investigate the processes causing lateral facies variation in a palaeo-shoreline setting.

The Spirit River Formation is a prolific gas reservoir of Alberta and the British Columbia Deep Basin. The Falher Member is the main hydrocarbon-producing part of this formation, and it has been formally subdivided into genetically related parasequences / parasequence sets that have informally been designated the Falher A through G (Cant, 1984; Jackson, 1984; Leckie, 1986; Casas and Walker, 1997; Zonneveld and Moslow, 2004; Adani, 2019; Newitt and Pedersen, 2022). Individual Falher Member cycles are interpreted as prograding shoreface units grading from fine-grained offshore to lower shoreface sandstone to upper shoreface to foreshore conglomeratic sandstone and/or conglomerate (Cant, 1983; Jackson, 1984).

The Falher D Member comprises several conventional, clast-supported, conglomeratic, and unconventional (tight) sandstone / sand-matrix conglomerate reservoirs (Cant, 1984). Due to its economic importance, it has been the subject of several studies and several depositional models have been proposed to explain the reservoir quality and distribution of Falher D reservoir geobodies (Leckie and Walker, 1982; Cant, 1983; 1984; Arnott, 1993; Casas and Walker, 1997; Hoffman, 2008). Most paleogeographic proposals agree that deposition occurred along an arcuate, generally, east-west trending palaeo-shoreline of a shallow epeiric sea situated to the north (Stott 1968; Leckie and Walker, 1982). Importantly, contrasting shoreface (Casas and Walker, 1997) and deltaic (Leckie and Walker 1982; Arnott 1993; Hoffman 2008) interpretations of observed conglomerate facies are still subject to debate.

This study uses sedimentological and ichnological observations in the context of a UAV (Unmanned Aerial Vehicle)-based photogrammetry method for further investigation of

depositional affinities of sandstone and conglomerate lithosomes of Falher D Member. The photogrammetric method has been used to analyze outcrops with visualization and quantitative data collection (e.g., Tavani et al., 2014; Hayes et al., 2018; Bilmes et al., 2019). Advantages of using this method are being able to perform multiple measurements promptly, calculate measurement errors and observe the outcrop in its entirety. Environmental- and instrument-sourced distortions during image acquisition and lack of ability to interpret small-scale sedimentary features that are below model resolution are disadvantages (Hayes et al., 2017).

This research focusses on the Falher Member outcrops at Mount Spieker, British Columbia to facilitate better understanding of the facies distribution and refining depositional models of Lower Cretaceous reservoir units in western Canada. Three-dimensional photogrammetric models were procured with a large series of overlapping georeferenced and compass oriented drone images from Falher D equivalent deposits crop out at Mount Spieker, British Columbia region. Dip-strike orientations, palaeocurrent directions, and bedding thicknesses were calculated from the model. Descriptions of lithology, bedding contacts, ichnofossil distributions, and sedimentary structures were recorded in the field and used along with the model as bases for the interpretations.

The objectives of this study are 1) developing and analyzing 3D models supported with field observations to interpret facies, facies variations, 2) proposing a depositional model, and 3) evaluating reservoir quality and distribution for the Falher D Member. The proposed model and interpretations will contribute to a better understanding of reservoir facies distribution in the Falher Member and help to better understand the architecture of this economically important unit.

2.2 Regional Stratigraphy and Study Area

In the early Cretaceous the Cordillera was tectonically uplifted. This combined with flexural subsidence to the east, formed the asymmetrical Western Canada Foreland Basin of western Alberta and northeast British Columbia. The associated foredeep is informally referred to as the “Deep Basin” (Wright et al., 1994; Monger and Price, 2002). During the Barremian, alluvial fan and braided fluvial deposits, preserved as the Cadomin Formation, were deposited in the axially-drained Deep Basin (McLean, 1977; Schultheis and Mountjoy, 1978). Erosional lowering of the Cordillera, combined with continued basin subsidence allowed for deposition and preservation of

a thick succession of heterolithic sediments deposited in meandering fluvial and deltaic settings, preserved as the Aptian to Albian Gething formation (Stott, 1973; Smith et al., 1984).

Iterative marine transgressions and regressions from the north during the Albian resulted in expansion and contraction of the shallow epeiric Boreal Sea, which covered north-eastern British Columbia, northern Alberta and west-central Saskatchewan (Williams and Stelck, 1975) (Fig. 2.1). These flooding events are evidenced by coastal and marine-deposited sandstone units of the Gething Formation and the overlying Bluesky and Moosebar Formation / Wilrich Member of the Spirit River Formation. The Moosebar / Wilrich transgression resulted in deposition of a thick succession of dark, organic-rich shale, deposited during the interval of maximum depth and southward extent of the Boreal Sea (Stelck and Kramers, 1980). Increased sediment input outpaced the rise of sea level during middle-early Albian, resulting in rapid regional progradation of the south shore of the Boreal Sea towards the north (Jackson, 1984; Smith et al., 1984).

The Lower Cretaceous Spirit River Formation was deposited as a northward prograding siliciclastic wedge (Williams and Stelck, 1975; Smith et al., 1984). In the Deep Basin this unit has been subdivided into (from bottom to top) the Wilrich, Falher and the Notikewin members (Fig. 2.1). The sandstone and conglomerate-dominated Falher Member hosts the major gas reservoirs within the Spirit River Formation. The Falher Member conformably overlies, and interfingers with, the Wilrich Member, which comprises a coarsening upward succession of shale, siltstone and very-fine-grained sandstone deposited primarily in distal to proximal offshore, offshore transition and lower shoreface environments (MacDonald et al., 1988; Newitt et al., 2015). The Notikewin Member conformably overlies the Falher-Wilrich succession (Cant, 1984).

The Gates Formation is the outcrop stratigraphic equivalent to the Falher and Notikewin Members that crops out in north-east British Columbia (Leckie and Walker, 1982; Leckie, 1985b; Moslow and Schink, 1995; Moslow, 1998; Caddel, 1999; Caddel and Moslow, 2004; Zonneveld and Moslow, 2004). The Gates Formation is further subdivided into the Torrens and Grand Cache Members (Leckie 1982; 1985). Some authors have informally assigned outcrop units of the Gates Formation to the Falher A through H and Notikewin Members (Leckie 1983; Zonneveld and Moslow 2004) although, *sensu stricto*, the Falher and Notikewin are stratigraphic terms restricted to the subsurface of the WCSB.

The Falher Member consists of sets of coarsening-upwards depositional successions, which exhibit overall fining towards the North (Stott, 1968; Leckie and Walker, 1982; Cassas and Walker, 1997). Falher parasequences / parasequence sets, are referred to, from top to base as the A to F (Jackson, 1984; Cassas and Walker, 1997; Caddell and Moslow, 2004; Zonneveld and Moslow, 2004; Armitage et al., 2004; Nodwell and Hart, 2006). Zonneveld and Moslow (2004) identified a conglomeratic fairway as an outcrop equivalent to the Falher G in the Gates Formation which underlies the Falher A-E Member trends. Older parasequence sets that are laterally correlatable with the lower shale/siltstone succession of the Wilrich Formation occur between the Bluesky and the Falher G (Fig. 2.1) and have been informally assigned to the Falher H, I, etc. (Jackson, 1984; Zonneveld and Moslow, 2004; Newitt, 2015; Zonneveld, 2018).

Individual Falher Member parasequences have been described as prograding shoreface units consisting of fine-grained sandstone beds representing offshore to lower shoreface deposition, grading upwards into conglomeratic sandstone, and matrix- to grain-supported conglomerate representing upper shoreface to foreshore and washover fan depositional environments (Cant, 1984; Wadsworth et al., 2003; Armitage et al., 2004; Caddell and Moslow, 2004; Zonneveld and Moslow, 2004). On gamma-ray and sonic well logs, units are typically separated by the distinctive spikes of coal beds (Fig. 2.1). The rough cyclicity of the Falher Member is attributed to sedimentation rates periodically outpacing, and being outpaced by, relative sea level rise; caused by episodic tectonic activation of Cordillera (Cant, 1983; 1984) now they are accepted as genetically related groups of parasequences and/or parasequence sets (i.e., Arnott, 1993; Cassas and Walker, 1997).

The Falher A, B, C, D and F trends include open framework texture strand plain conglomerate facies interpreted as main conventional reservoir units (Cassas and Walker, 1997; Caddell and Moslow, 2004; Zonneveld and Moslow, 2004; Armitage et al., 2004; Nodwell and Hart, 2006). On the other hand, matrix supported conglomerate and sandstone facies included within those Falher cycles are interpreted as unconventional reservoirs due to their low permeability and porosity (Zonneveld et al., 2017). Low values of porosity and permeability are caused by burial diagenesis and quartz cementation (Cant and Ethier, 1984). The Falher D Member in subsurface was discussed in terms of sequence stratigraphy and sedimentology by Cassas and Walker (1997) and subdivided into D1 through D5 sub-cycles. Detailed sedimentology and depositional environment interpretations were discussed, and an asymmetrical



Figure 2.2. Location map showing the Deep Basin and the location of the outcrop study area at Mount Spieker (Caddel and Moslow, 2004). Note that excellent exposure of Falher C, D and F equivalent stratigraphic successions occurs are Mount Spieker, and mounts Bullmoose, Chamberlin (Leckie and Walker, 1982; Leckie, 1985b; Moslow and Schink, 1995; Moslow, 1998; Caddel, 1999; Caddel and Moslow, 2004; Zonneveld and Moslow, 2004).



Figure 2.3. Google Earth satellite image of study area; measurement locations are labelled with yellow stars (W: West Ridge, E: East Ridge, S: South Ridge).

Table 2.1. *Study locations-GPS Coordinates*

Ridge	GPS Coordinate
West Ridge	N55° 08' 53.0" W121° 24' 41.2"
East Ridge	N55° 08' 58.3" W121° 24' 38.0"
South Ridge	N55° 08' 36.4" W121° 24' 09.0"

2.3 Methodology

The study focuses on facies interpretations of the Falher D Member to propose a depositional model to explain the processes which caused lateral facies variations. Within the scope of this study, 3D models of West, East and South ridges were assembled using software that integrates structure from motion (SfM) and multiview-stereo (MVS) algorithms. Five stratigraphic sections were measured on field, and master bedding orientations and palaeocurrent direction measurements were obtained from dune scale cross-lamina sets on 3D models. Vertical stratigraphic section measurements were obtained in the field.

Facies classifications include description of grain size, sedimentary structures, and bedding contacts. Also, the Falher D facies are evaluated in terms of trace fossil assemblages.

The assessment of bioturbation intensity for each facies is quantified by Bioturbation Index (**BI**) values ranging between 0-6, **BI** 0 reflecting no bioturbation and **BI** 6 total biogenic reworking (Taylor and Goldring, 1993; Bann et al., 2008).

Lithologs were digitized and are presented herein as strip logs in Corel Draw format. Each facies were evaluated using petrography of 65 thin sections, which were from rock samples that were collected every half-meter in vertical section.

3D Outcrop Modeling with UAV-Based Photogrammetry Method

Unmanned Aerial Vehicle (UAV) - based photogrammetry method enables the acquisition of high spatial-resolution data, which support and are supported by field observations. UAV-based 3D photogrammetry models were built using software that used structure from motion (SfM) output linked with multiview-stereo (MVS) matching algorithms (e.g., James et al., 2012;

Westoby et al., 2012; Hayes et al., 2017; 2018). SfM-MVS algorithms are based on matching image textures in different images and interpolating the 3D geometry for static scenes (Seitz et al. 2006). Structure from Motion (SfM) (SfM: Ullman 1979) is a photogrammetry method used to build the 3D models and 2D photomosaics from a series of overlapping offset images. With the SfM method, camera location and geometry are automatically acquired without known 3D points (Westoby 2012). Matching features of multiple images enables acquisition of camera locations and object coordinates to build a sparse 3D point cloud (Snavely, 2008; James et al., 2012). MVS algorithms increase the number of reconstructed points by two orders of magnitude by eliminating data noise, resulting in a dense point cloud that can generate digital elevation models (Seitz et al., 2006).

In this study the 3D outcrop models were built using Agisoft Metashape software using algorithms of structure from motion (SfM) photogrammetry linked with multi-view stereo MVS method. Image data were gathered via DJI Mavic Pro-2 drone type UAV with a Hasselblad 20MP camera at Mount Spieker. Collected drone data consists of a series of images with at least 60% sidelap and vertically-overlapping georeferenced images taken approximately 5 to 10 meters from the outcrop. To minimize data acquisition sourced errors, overlapping images should be taken from multiple points of view by using same camera and lenses and focal length should be fixed (Tavani et al., 2014). Drone images are processed prior to modelling with Agisoft Metashape by using Adobe Photoshop to remove 'noise' such as shadows, balance image brightness, and balance color contrast. Enhancement of images provided more visibility for small scale sedimentary structures like laminae sets.

Modelling stages are presented in Figure 2.4. Processing of acquired images is required prior to work on software. Photo alignment is the first stage, wherein camera position and image orientations are calculated through detection of matching points on the images to build a sparse cloud model. Incorrectly positioned camera locations are detected and either realigned or removed at this stage. Subsequent to this, dense point cloud stage depth information is calculated based on estimated camera positions and image orientations at the previous stage. Matching points are used to build a geometry (polygonal model) by triangular mesh and a texture map draped onto the triangular mesh. U and V coordinates are given to each vertex of the triangle of the mesh. This permit cropping a triangle in the texture map to paste it onto the corresponding mesh-face (Tavani et al., 2014). The higher the number of faces, the better the model's spatial

resolution. The texture generating stage involves color calibration which improves texture quality. Modelling work is finalized by generation of high resolution 2D imagery called “orthomosaic” based on source and reconstructed 3D models.

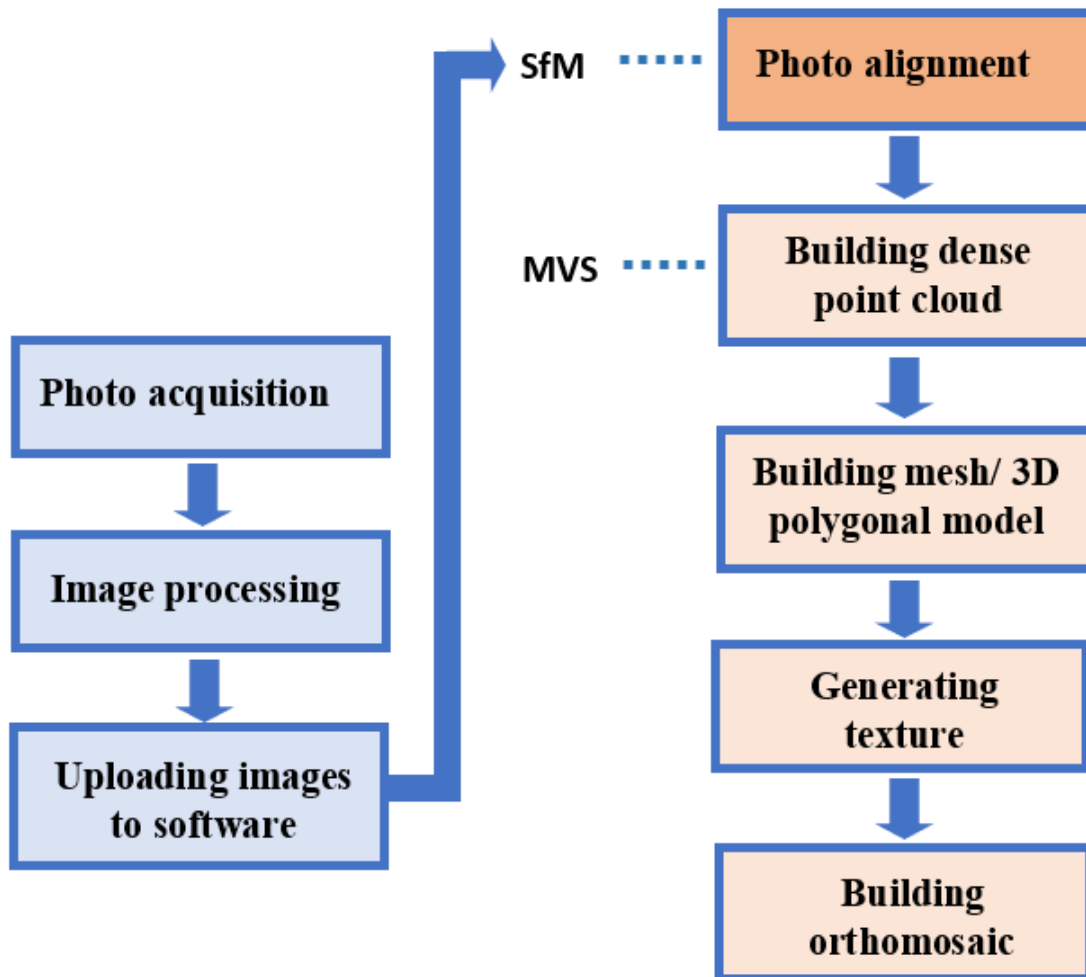


Figure 2.4. Flow chart presents stages of building a 3D model via Agisoft Metashape Software. SfM and MVS algorithm-based stages are indicated (modified from Hayes et al., 2017).

After completion of modelling, stage 2D photomosaics are exported from software and scaled in Photoshop to measure vertical facies thicknesses, hummock and swale wavelengths and amplitudes for different intervals in the depositional succession. The ridges are interpreted in terms of their lithofacies, and each lithofacies unit is traced on 2D photomosaics via Adobe Illustrator depending on grain size variations and the succession of large-scale sedimentary

structures (e.g., hummocky cross-stratification (HCS) and dune size cross-stratification). Vertical thicknesses of lithofacies were calculated on 3D models by subtracting the elevation (z) values of upper and lower contacts of each unit. Exposed master bedding planes and cross-laminae are used to measure the strike and dip direction (discussed below).

In short, the 3D model enables the documentation of lateral and vertical facies variations over large outcrops. In addition, both 3D models and 2D photomosaics provide valuable numerical observations for orientations, large scale sedimentary structures such as hummocky cross-stratification and dune-scale cross-lamina sets.

Orientation Calculations

Python script is used to calculate orientations (strike, dip amount, dip azimuth) of bedding and foreset laminae planes by processing marker-point coordinate data consisting of longitude (x), latitude (y) and altitude (z) values. Marker points are individual nodes which are located on bedding plane and foreset laminae as clusters to obtain x , y , z value for each point located on surface.

Three-point method is commonly used to calculate dip and strike orientations for best fit planes aligned with those coordinates. On 3D model there are more than three points available for each bedding plane and foreset laminae which provides more accurate results.

The Python script uses moment of inertia method to fit a plane passes through points which are more than three (Fernández, 2005). This method calculates coordinates of moments of inertia and axis of maximum moment of inertia of point clusters as the pole to the best fit plane (Fernández, 2005) by assuming that best fit plane passes through a point of average (x_{avg} , y_{avg} , z_{avg}) coordinates of marker points (marker point's center of mass). Orientation matrix is built by calculation of vectors connecting the center of mass from marker point data. Matrix **T** is given below (Fig. 5) l_i , m_i and n_i values are corresponding to x , y , z coordinates obtained from marker points. Matrix **T** is solved with inserting coordinates and eigen values (λ_1 , λ_2 , λ_3) and eigen vectors (v_1 , v_2 , v_3) are calculated (Woodcock, 1977) (Fig. 2.5). For more information regarding orientation measurement method with **T** matrix (Orientation Tensor Method) please refer to Woodcock (1997) and Fernández (2005).

$$\mathbf{T} = \begin{pmatrix} \sum l_i^2 & \sum l_i m_i & \sum l_i n_i \\ \sum m_i l_i & \sum m_i^2 & \sum m_i n_i \\ \sum n_i l_i & \sum n_i m_i & \sum n_i^2 \end{pmatrix}$$

Figure 2.5. **T** matrix is used to calculate coordinates of best-fit center of mass of plane, proposed by Woodcock, 1997.

Calculated eigen values are used to calculate **M** and **K** values for each orientation result in Figure 2.6 regarding formula for eigen values are provided. **M** and **K** values determine the accuracy of calculations. Depending on chart below; orientation results are considered as reliable if **M** is greater than 4, means marker points are distributed homogenously with less than 6 ° to best-fit plane. If **K** is below 0.8, that means marker points are widely distributed more than 30 °.

Obtaining accurate results (results within the reliable limit of **M** and **K** values) depends on the distribution of points on bedding planes. Evenly distributed marker points around a center of mass results in calculation of more reliable best fit plane orientation rather than co-linear distributed marker points (Fernández, 2005).

$$M = \ln(\lambda_1/\lambda_3)$$

$$K = \ln(\lambda_1/\lambda_2)/\ln(\lambda_2/\lambda_3)$$

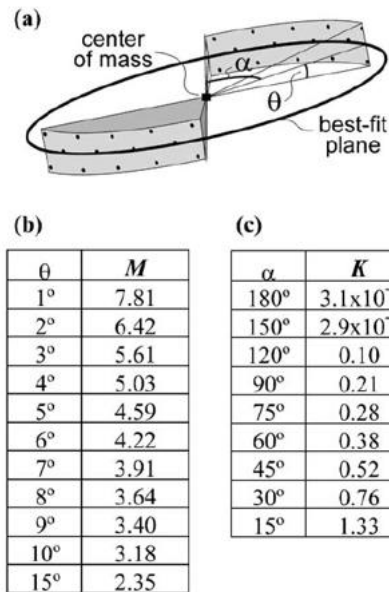


Figure 2.6. Table shows varying **M** and **K** values and corresponding α and θ values. In figure (a) there are evenly distributed nodes (marker points) around a center of mass which represents a best fit plane. α and θ values are representing alignment of best fit plane in two different directions. Table (b) shows corresponding **M** to varying θ values; if all marker points are distributed homogenously below and above mean plane which corresponds case of $\alpha=180^\circ$, Table (c) shows **K** value correlation with varying α values in case of all points are equidistant from center of mass and distributed homogenously with angle of $\theta=2^\circ$ (Fernandez, 2005).

Calculations provided dip, strike values and dip direction for the best fit plane passes center of mass of marker points given for bedding surfaces and foreset laminae. Results are represented as tadpole and rose plot diagrams, which shows dip and palaeoflow direction variations through investigated parts of parasequences. Many measurements performed at different ridges and different bedding planes within same ridge provide information regarding north to south and east to west variations and causing palaeogeographic and palaeoenvironmental conditions.

2.4 Results

Ten depositional facies are described herein (Fig. 2.7). Their sedimentological characteristics and corresponding interpretations are presented on Table 2.2. Palaeocurrent measurements were represented as equal area stereonet plots (Fig. 2.8).

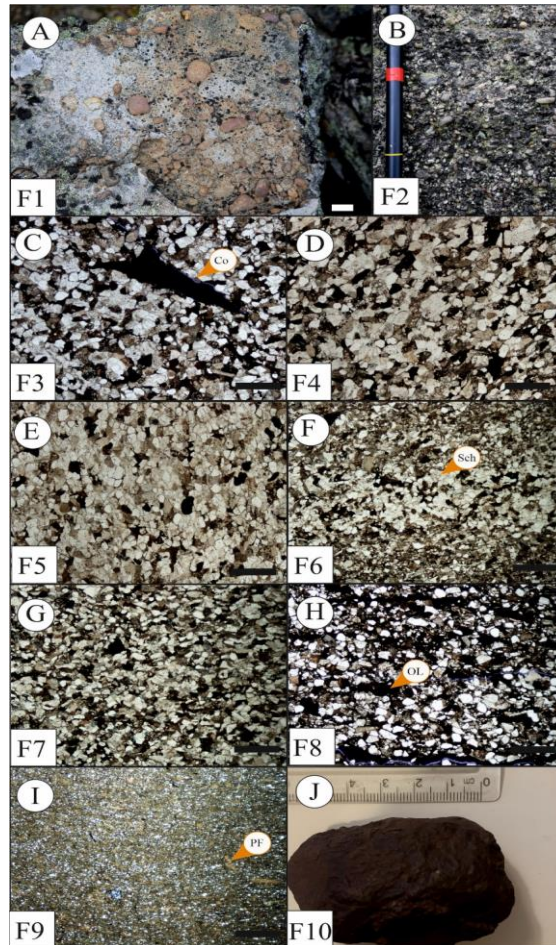


Figure 2.7. Lithofacies photographs and under PPL photomicrographs of facies listed on Table 1. **A)** Photograph of polymodal, poorly-sorted, sand-matrix-supported conglomerate (**F1**), white bar scale 1.50 cm in length. **B)** Photograph of bimodal grain-supported, open-framework, conglomerate facies (**F2**), black Jacob's staff: each part is 10.00 cm in length. **C)** Photomicrograph of upper-fine to medium-grained, well-sorted sandstone facies with coal fragments (**F3**), arrow points the coal fragment (**Co**) **D)** Photomicrograph of locally conglomeratic, well-sorted, upper-fine to medium-grained sandstone facies showing cross stratification (**F4**) **E)** Photomicrograph of

very well-sorted, medium-grained, swaley cross-stratified, sandstone facies (**F5**) **F** Photomicrograph of highly-bioturbated very fine- to fine-grained sandstone (**F6**), arrow points clean quartz lining of *Schaubcylindrichnus* isp. Burrow (**Sch**). **G** Photomicrograph of low-angle planar-laminated, moderately-sorted, very fine- to fine-grained sandstone facies (**F7**) **H** Moderately-sorted, fine-grained sandstone facies (**F8**), arrow points organic laminae (**OL**). **I** Mudstone facies (**F9**), arrow points abundant micro plant fragments (**PF**) **J** Brownish, reddish-colored ironstone nodule (**F10**). The bar scale for photomicrographs is 1.00 mm.

Table 2.2. Summary of facies described in Falher D parasequence observed at Mount Spieker outcrops. ((a): abundant, (m): moderate, (r): rare)

Description	Occurrence and Contacts	Sedimentology/ Accessories	Ichnology / Fossils
<p>F1 Massive to planar stratified conglomerate</p>	<ul style="list-style-type: none"> • Observed on all ridges. • Irregular erosive to sharp bottom contacts overlies F5 and F6. • Palaeolandward (south) decreasing structural dip amount measured on West Ridge dip section. • Eastwards thinning of this unit observed. 	<ul style="list-style-type: none"> • Moderately to poorly sorted rounded, locally clast or medium-grained sand matrix supported polymodal to bimodal conglomerate with dominant granule to pebble size chert framework grains • Massively bedded to planar stratified bed-sets • Local cross-stratification at upper parts • Scoured base with gutter casts. • Spherulitic siderite was observed on South Ridge exposure • Upwards increasing sand matrix content within a single bed • Inverse and normal graded alternating beddings • Upward increasing bedding thickness' 	<ul style="list-style-type: none"> • Absent

<p>F2 Cross-stratified conglomerate</p>	<ul style="list-style-type: none"> • Observed on West and East Ridge outcrops at the top part of the measured sections. • Overlies F1-F5 tempestite couplets with irregular erosive contacts. 	<ul style="list-style-type: none"> • Moderately sorted rounded, locally clast or medium-grained sand matrix supported polymodal to bimodal conglomerate with granule to cobble size dominant chert framework grains • Local unimodal distribution of granular framework grains • Trough cross-stratification • Clast supported bimodal parts show open framework texture • Tabular cross bedded sets are common with rare bidirectional pattern • Foreset laminae measurement 25-35° dip amounts towards east (West Ridge) to southeast (on East Ridge) 	<ul style="list-style-type: none"> • Absent
<p>F3 Cross-stratified sandstone with coal fragments</p>	<ul style="list-style-type: none"> • Observed on upper part of the South Ridge section, has sharp to erosive bottom contacts with pebbly laminae. • Overlies F4. 	<ul style="list-style-type: none"> • Well-sorted upper fine- medium grained sandstone with evenly scattered granule to pebble size clasts • Tabular cross-stratified to planar parallel stratified bed-sets • Locally bidirectional pattern • Current ripple laminae • Coal fragments 	<ul style="list-style-type: none"> • <i>Cryptic</i> • Vertical and horizontal sinuous quartz backfilled less than a mm scale thick burrows. Trace fossil disturbance of micro scale grading of the sand grains observed.
<p>F4 Locally conglomeratic</p>	<ul style="list-style-type: none"> • Observed on South Ridge has erosive internal bedding contacts with pebbly layers. 	<ul style="list-style-type: none"> • Well-sorted upper fine to medium-grained sandstone • Large scale planar cross-stratification (with 30-35 ° dip) with 	<ul style="list-style-type: none"> • <i>Cryptic</i> • Vertical and horizontal sinuous quartz

cross-stratified sandstone		low-angle internal truncation surfaces <ul style="list-style-type: none"> • Abundant scattered pebbles 	backfilled less than a mm thick burrows <ul style="list-style-type: none"> • <i>Macaronichnus</i> isp. (<i>r</i>) burrows • BI (0-1)
F5 Low-angle planar cross-stratified sandstone	<ul style="list-style-type: none"> • Observed on West and East ridges. • Overlies F1 with a sharp contact and forms tempestite couplets. • Appears as locally discontinuous sand lenses on West Ridge. • Northwards (palaeobasinward) and Eastwards thickens. 	<ul style="list-style-type: none"> • Very well-sorted upper fine to medium-grained sandstone • Gently dipping (10-15 °) cross-stratified, convex down to planar parallel laminae interpreted as swaley cross-stratification • On East Ridge rare HCS observed within these facies • N-S oriented westwards migrating pebbly channelized structures cross cutting, cross-stratified bed-sets 	<ul style="list-style-type: none"> • <i>Cryptic</i> • Vertical and horizontal sinuous quartz backfilled less than a mm thick burrows.

<p>F6 Highly bioturbated silty-sandstone</p>	<ul style="list-style-type: none"> • Observed on West and East Ridges. • Scoured upper contact with F1 and gradational contact underlying with F7 	<ul style="list-style-type: none"> • Highly bioturbated well sorted very fine to fine-grained silty-sandstone. • Low-angle sub-parallel HCS to wavy laminated bed-sets • Soft sediment deformation structures • Bioturbation and soft sedimentary deformational structures obscure sedimentary structures • Carbonaceous laminae • Pyrite nodules (r) • Terrigenous plant fragments (a) observed at the contact with overlying F1 • Conglomerate lenses up to a meter long and less than a cm thick (a) • At high BI valued parts pebbles are scattered conversely in non-bioturbated parts pebble laminae observed • Lam-scam bedding 	<ul style="list-style-type: none"> • <i>Cryptic</i> • Vertical and horizontal sinuous quartz backfilled mm scale thick burrows. • BI values are ranging between 0-3-4 with an increasing upward trend within same facies. • <i>Diplocraterion</i> isp. (a), <i>Skolithos</i> isp. (r), <i>Planolites</i> isp. (r), <i>Rhizocorallium</i> isp. (m), <i>Schaubcylindrichnus</i> isp. (m), <i>Rossellia</i> isp. (r), <i>Teichichnus</i> isp. (m), <i>Macaronichnus</i> isp. (a) • Fossil wood
<p>F7 Low-angle parallel laminated silty-sandstone</p>	<ul style="list-style-type: none"> • Observed on all ridges has a gradational contact with F6 on West and, East ridges 	<ul style="list-style-type: none"> • Low-angle planar parallel to quasi planar lamination with abundant internal low-angle truncation surfaces (HCS) • Ripple laminae • Conglomerate lenses or stringers up to a meter long and less than a centimeter thick • Scour and fill bedding are common. • Silty laminae 	<ul style="list-style-type: none"> • <i>Cryptic</i> • Vertical and horizontal sinuous quartz backfilled mm scale thick burrows. • <i>Schaubcylindrichnus</i> isp. (m)

<p>F8 Muddy sandstone</p>	<ul style="list-style-type: none"> • Observed on South Ridge. • Forms the basal part of the measured section. 	<ul style="list-style-type: none"> • Moderately sorted angular to subrounded-grained argillaceous very fine to fine sandstone • Low-angle sub-parallel HCS laminated bed-sets with scattered pebbles • Organic laminae (a) • Pyrite 	<ul style="list-style-type: none"> • Absent
<p>F9 Organic rich mudstone</p>	<ul style="list-style-type: none"> • Observed on South Ridge. • Intercalated with F7 as discontinuous lenses and has sharp contacts. 	<ul style="list-style-type: none"> • Planar laminae • Abundant organics • Micro plant fragments • High siderite content 	<ul style="list-style-type: none"> • Absent
<p>F10 Ironstone</p>	<ul style="list-style-type: none"> • Observed on South Ridge interbedded with F4 and F1 as discontinuous lenses. 	<ul style="list-style-type: none"> • Exists as couple of cm up to 15 cm thick lenses • Concretion observed • Goethite is the major iron bearing mineral 	<ul style="list-style-type: none"> • Absent

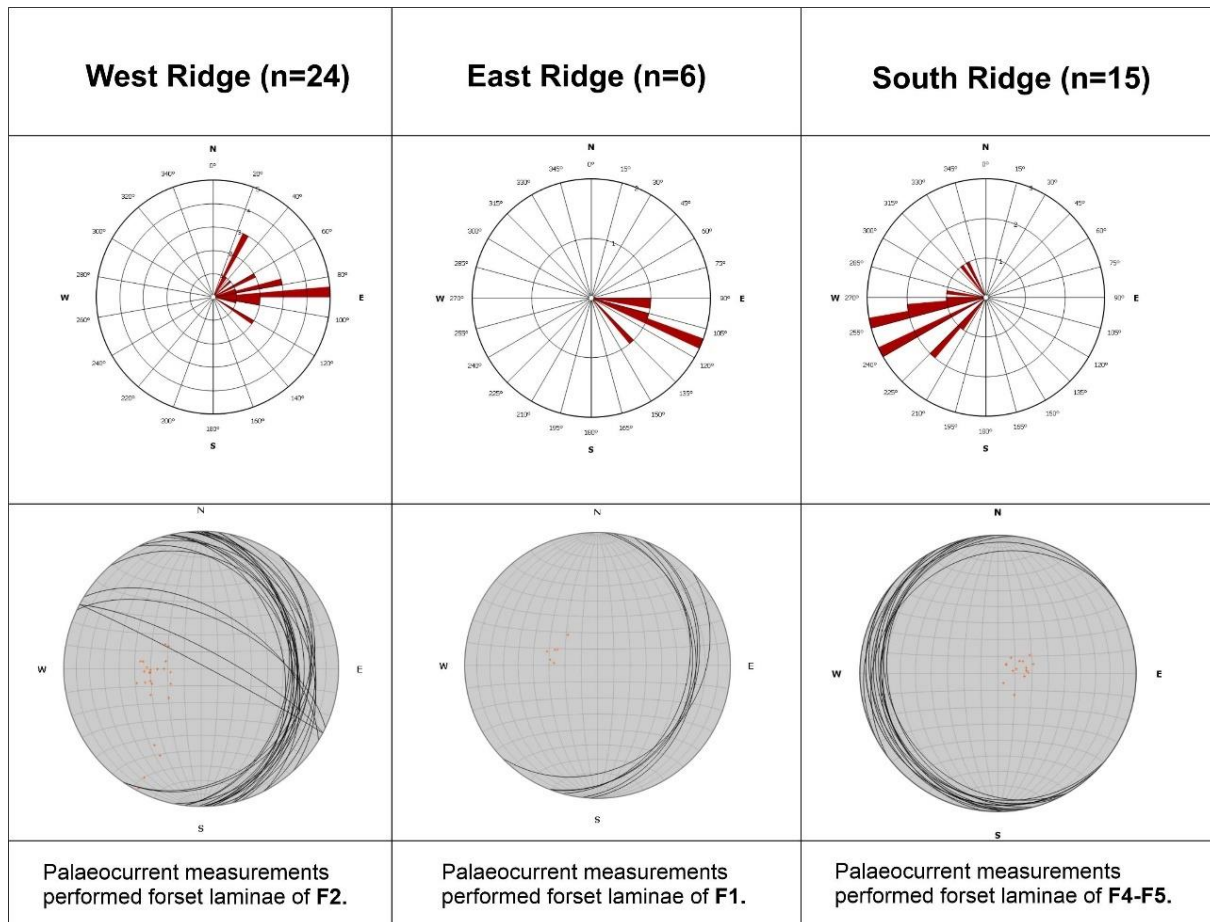


Figure 2.8. Rose and equal area stereonet plots representing palaeoflow directions for West, East and South ridges respectively. West and East Ridge measurements indicate eastwards dominant palaeoflow on the other hand South Ridge measurements indicate westwards dominant palaeoflow.

2.4.1 West Ridge

This ridge is at the westernmost part of the study area, and the outcrop is oriented north-south (Fig. 2.10A). Master bedding plane orientation measurements indicate 2-8 ° north-northwest dip and foreset laminae measurements indicate dominantly east-oriented palaeocurrent flow directions (Figs. 2.8, 2.10A). Northwards downlapping clinofolds are observable on photomosaic (Figs. 2.10B, C, and D). Master bedding plane dips show a gentle increase towards the north (Fig. 2.10).

Four different facies are observed on the West Ridge (Table 2.2), (Fig. 2.7, 2.9). *Cryptically*-bioturbated, low-angle, parallel laminated, very fine-grained silty-sandstone facies with common

internal truncation surfaces aligned with pebbly lags and rare oscillation ripples (**F7**) occur at the base of the measured outcrop section (Figs. 2.7G, 2.11A). Laminated silty-sandstone facies (**F7**) are overlain by highly bioturbated very fine-grained silty-sandstone beds (**F6**) (Fig. 2.7F). Trace fossils in this unit include abundant *Macaronichnus* isp., *Diplocraterion* isp., moderately abundant *Schaubcylindrichnus* isp., and rare *Planolites* isp., *Skolithos* isp., *Teichichnus* isp. and *Rhizocorallium* isp. traces. Other physical sedimentary structures and accessories recorded in bioturbated silty-sandstone facies (**F6**) are carbonaceous laminae, pebble laminae, scattered pebbles, pyrite nodules, and common soft sedimentary deformational structures near the contact with the overlying conglomerate facies (**F1**) (Figs. 2.11A, C, D). The contact between the thickly planar stratified to massively bedded conglomerate facies (**F1**) and the underlying highly bioturbated silty-sandstone facies (**F6**) is sharp and erosive with moderate scale 5-15 cm gutter casts (Figs. 2.11C, D). **F6-F1** facies contact changes into **F7-F1** contact southwards and preserved fossil wood clasts are observed near the contact (Fig. 2.11F). These locally massive to planar stratified conglomerate beds (**F1**) (Fig. 2.7A) also exhibit normal or inverse grading (Figs. 2.11E, H). Upper level bedsets of conglomerate facies locally exhibit cross stratified patterns. Massive to planar stratified conglomerate beds (**F1**) occur interbedded with low-angle cross-stratified fine to upper fine-grained sandstone beds (**F5**) (Fig. 2.11E). These low-angle cross-stratified beds (**F5**) are interpreted as swaley cross-stratification (SCS) (Fig. 2.10B). The SCS sandstone beds occur as discontinuous lenses in 2 to 15 cm thickness with a decreasing upwards trend in vertical section. Swaley cross-stratified sandstone beds locally contain cryptic bioturbation and rare *Schaubcylindrichnus* isp. This intercalated conglomerate facies (**F1**), and medium-grained sandstone facies (**F5**) are overlain by tabular to trough cross-stratified conglomerate facies (**F2**) as the uppermost part of the depositional section (**F2**) (Fig. 2.7B). Two vertical sections were measured on the West Ridge referred as Section A and Section B. Section A is situated further north (palaeobasinward) in comparison to section B. Detailed lithologic logs built for sections are presented in Figure 2.9.

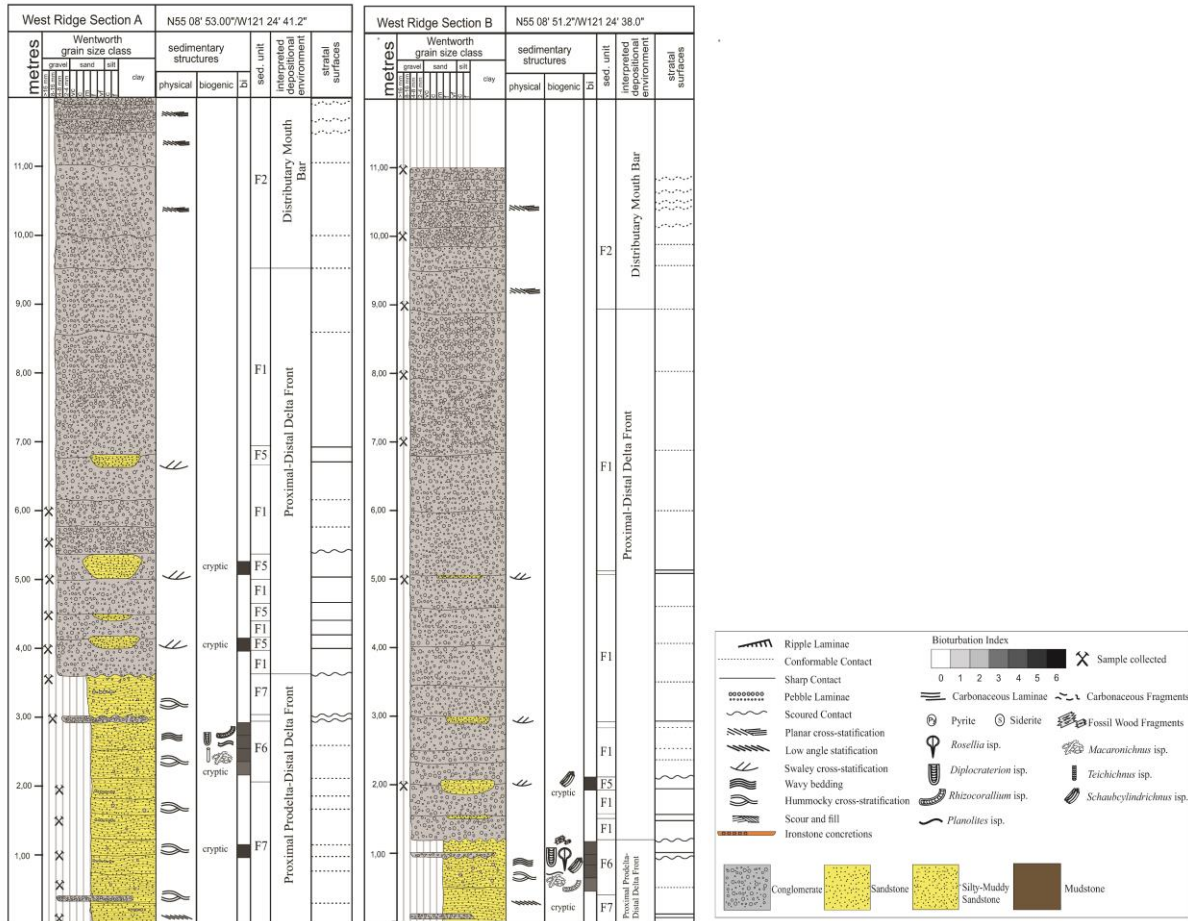


Figure 2.9. Lithologic strip logs representing facies thicknesses measured on West Ridge. From section A (basinward) to section B (landward) decrease in the abundance of sandy facies is observable.

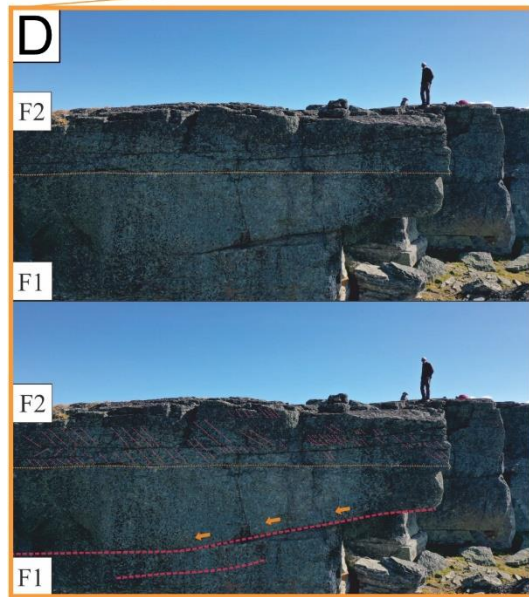
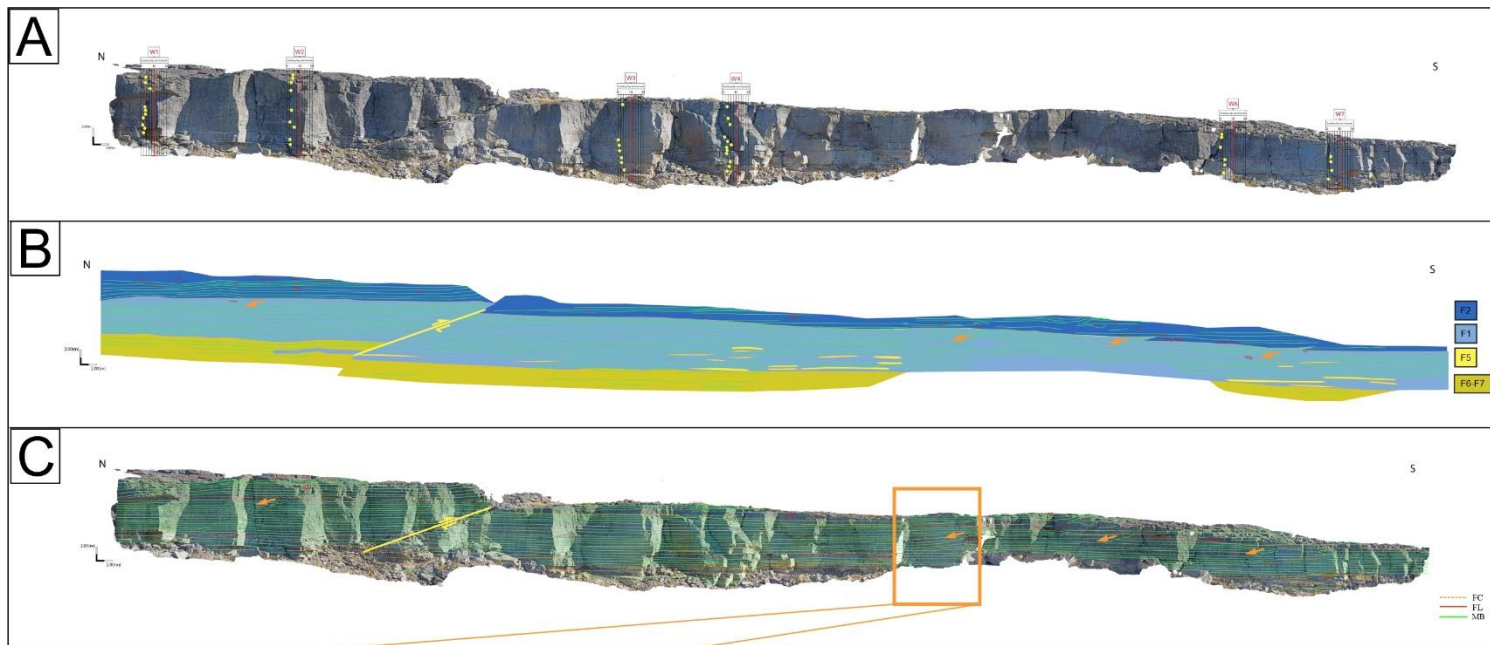
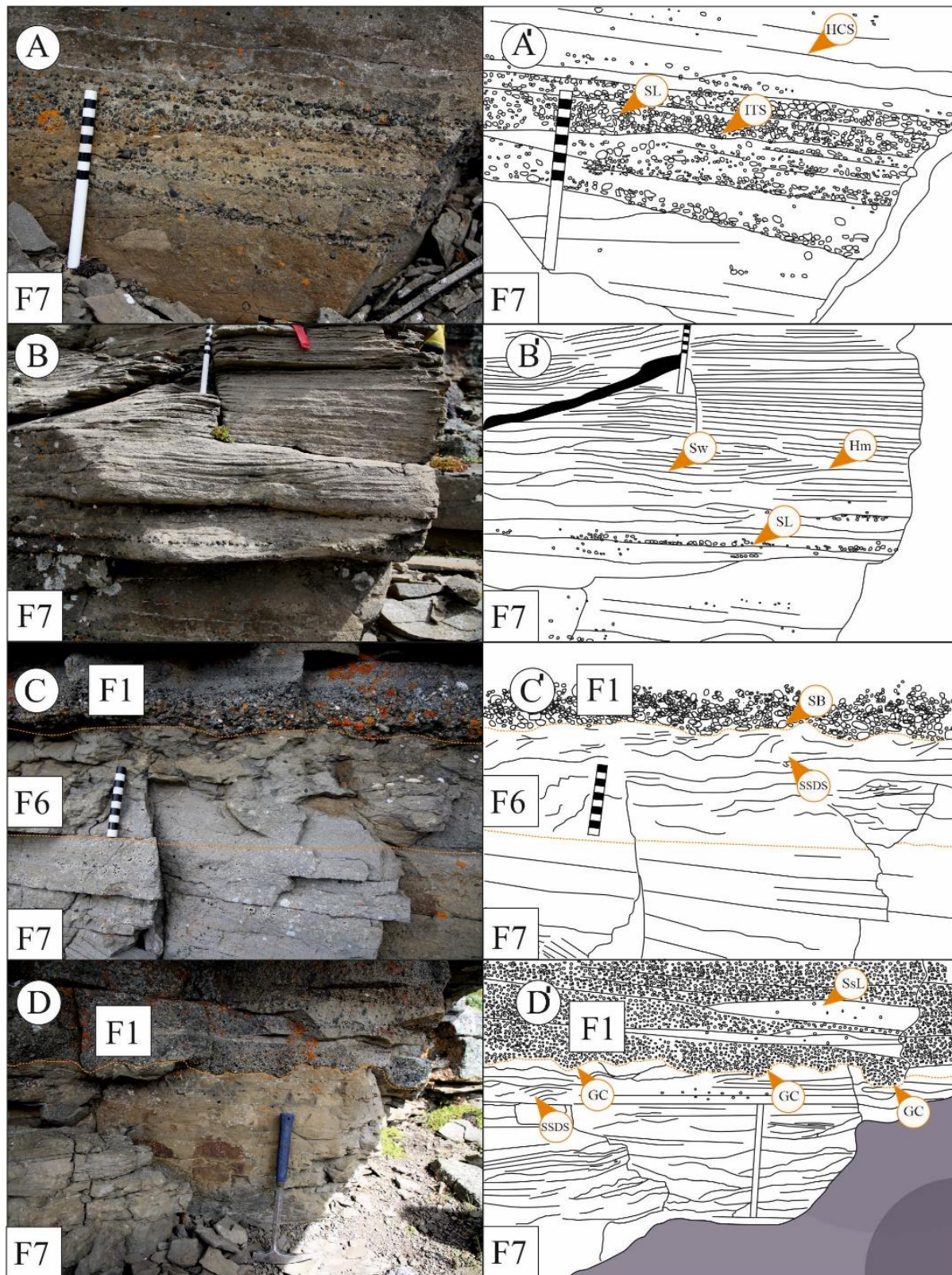


Figure 2.10. Photomosaics of West Ridge which are ~ 180m in width. **A)** West Ridge photomosaic with tadpole plots (see Appendix III) indicating dominantly NW dip direction. Landward decrease in the average dip amount is observable. **B-C)** Facies shading and interpretation of photomosaic; orange-dashed lines represent lithofacies contacts (**FC**), green-lines representing master bedding planes (**MB**), red-dashed lines representing foreset laminae (**FL**), and. Orange arrows indicating delta clinoforms dip direction and yellow lines represents fault plane. **D)** Close-up image of the area shown by rectangle; the contact between the cross bedded conglomerate facies (**F2**) and the massive conglomerate facies (**F1**), foreset laminae are traced with red-dashed lines and clinoform dip directions are indicated with orange arrows. Note that sandstone facies abundance slightly increasing basinward (North).



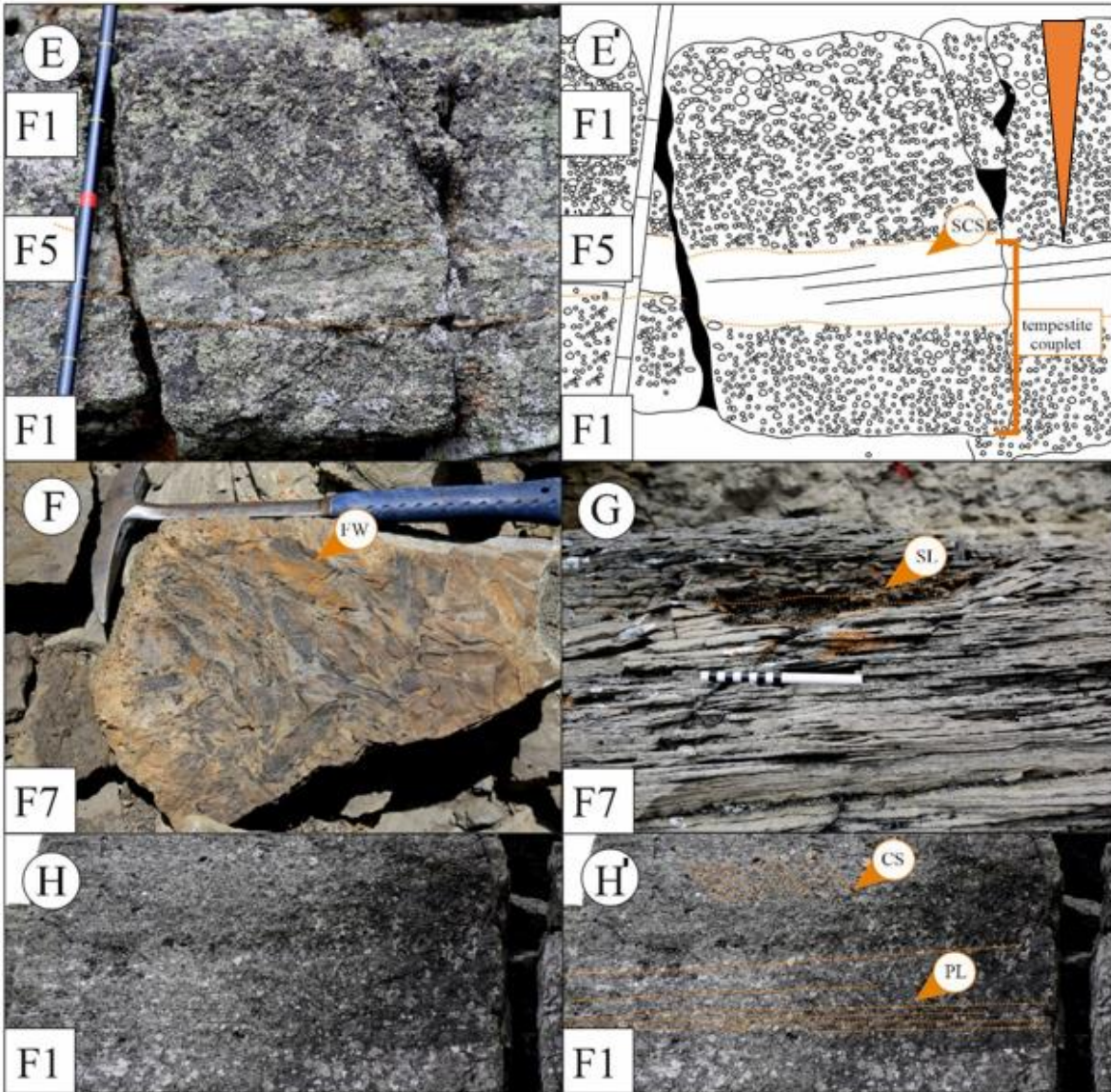


Figure 2.11. Outcrop photos and interpreted sketches of facies observed on the West Ridge. **A-A')** Low angle planar laminated (**HCS**) silty-sandstone facies with high angle internal truncation surfaces (**ITS**), pebbly-storm lags aligned through swale laminae. **B-B')** Swale (**Sw**) and hummock (**Hm**) structures indicating HCS deposited under storm conditions. Pebbly-laminae interpreted as storm lags (**SL**) deposited at peak energy levels of storm events. **C-C')** shows scoured bottom contact (**SB**) of conglomerate facies (**F1**) with underlying bioturbated sandstone facies. Abundant soft sedimentary deformational structures (**SSDS**) due to sudden deposition of conglomeratic units caused fluid escape and remobilization of underlying sandstones (**F7**). **D-D')** Abundant soft sedimentary deformational structures and gutter casts at **F1-F7** contact indicating deposition under sediment gravity flows. **E-E')** Massively bedded conglomerate facies (**F1**)

interbedded with swaley sandstone facies (F5) interpreted as tempestite couplets each representing a single storm event. Upper conglomerate bed (F1) shows inverse grading representing wax stage of storm event. F) Abundant fossil wood fragments preserved at sandstone (F7) and conglomerate facies (F1) contact. G) Discontinuous lenses of poorly sorted storm lags. H-H') Planar laminated to massive bedded structure of conglomerate facies (F1). Zebra stick is 20.00 cm and black Jacob's staff is 10.00 cm each part in length.

2.4.2 East Ridge

This outcrop is located on the north-eastern side of the West Ridge, and it is elongated in an east-west orientation (Fig. 2.3). Master bedding plane measurements indicate SE and NW dip directions (Fig. 2.13A). Palaeocurrent measurements indicate eastwards flow (Fig. 2.8). The thickness of sandy facies increases and that of conglomerate facies decreases compared with outcrop section further towards the west (Fig. 2.13B).

Four different facies are observed on East Ridge (Table 2.2) (Figs. 2.7, 2.12). From bottom to top: cryptically bioturbated low-angle parallel laminated very fine-grained silty-sandstone with internal truncation surfaces and common pebbly lags (F7) overlain by highly bioturbated very fine-grained silty-sandstone (F6) including abundant *Macaronichnus* isp., *Diplocraterion* isp., moderate *Schaubcylindrichnus* isp., and rare *Planolites* isp., *Skolithos* isp., *Rosselia* isp., *Teichichnus* isp., *Rhizocorallium* isp. Other features present in bioturbated sandstone facies (F6) include soft-sedimentary deformational structures primarily near the contact with the overlying conglomerate unit, abundant organic laminae, pebble laminae, scattered pebbles, pyrite nodules and lam-scam bedding (Fig. 2.14). Massive to cross-stratified conglomerate (F1) erosively overlies highly bioturbated silty-sandstone unit (F6). Massive to planar stratified conglomerate facies (F1) are interbedded with low-angle, cross-stratified (SCS-HCS) upper fine-grained sandstone beds (F5). Sandstone interbeds are mostly thicker and more continuous compared to west, average thickness of beds is ranging between 10 to 50 cm with a decreasing upwards and westwards trend (Figs. 2.13B, C). These intercalated units are overlain by same cross-stratified conglomerate facies (F2) forming the uppermost part of East and West Ridge sections.

The stratigraphic section measured on the East Ridge is referred to as Section C. A detailed lithologic log built for Section C is presented in Figure 2.12.

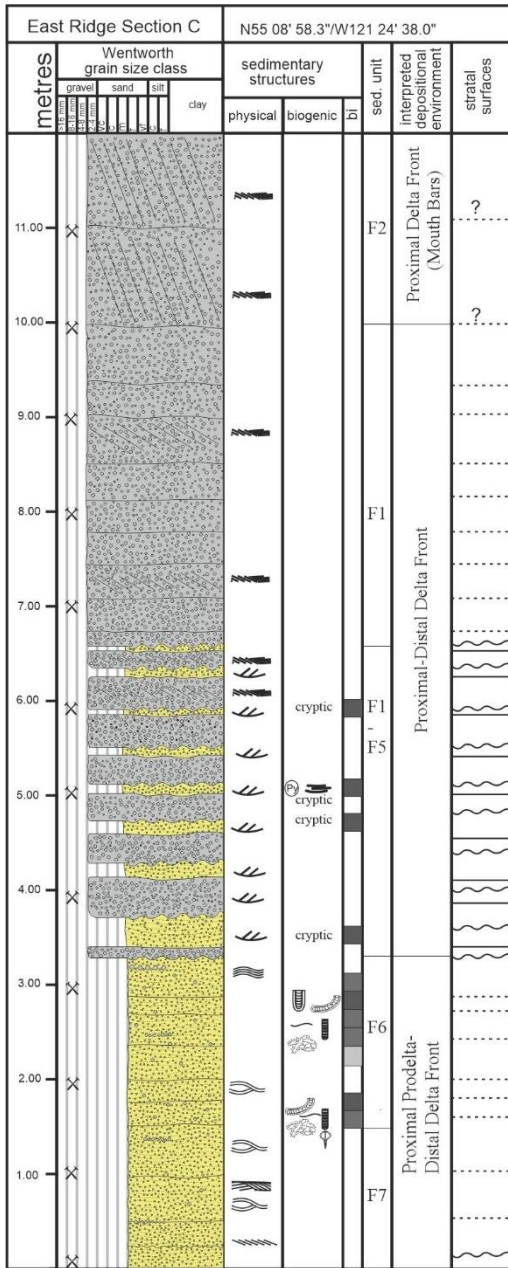


Figure 2.12. Lithologic strip log representing facies thicknesses measured on East Ridge outcrop. Compared to West Ridge increase in the abundance of sandy facies is observable (Symbols and lithofacies patterns as in legend in Fig. 2.9).

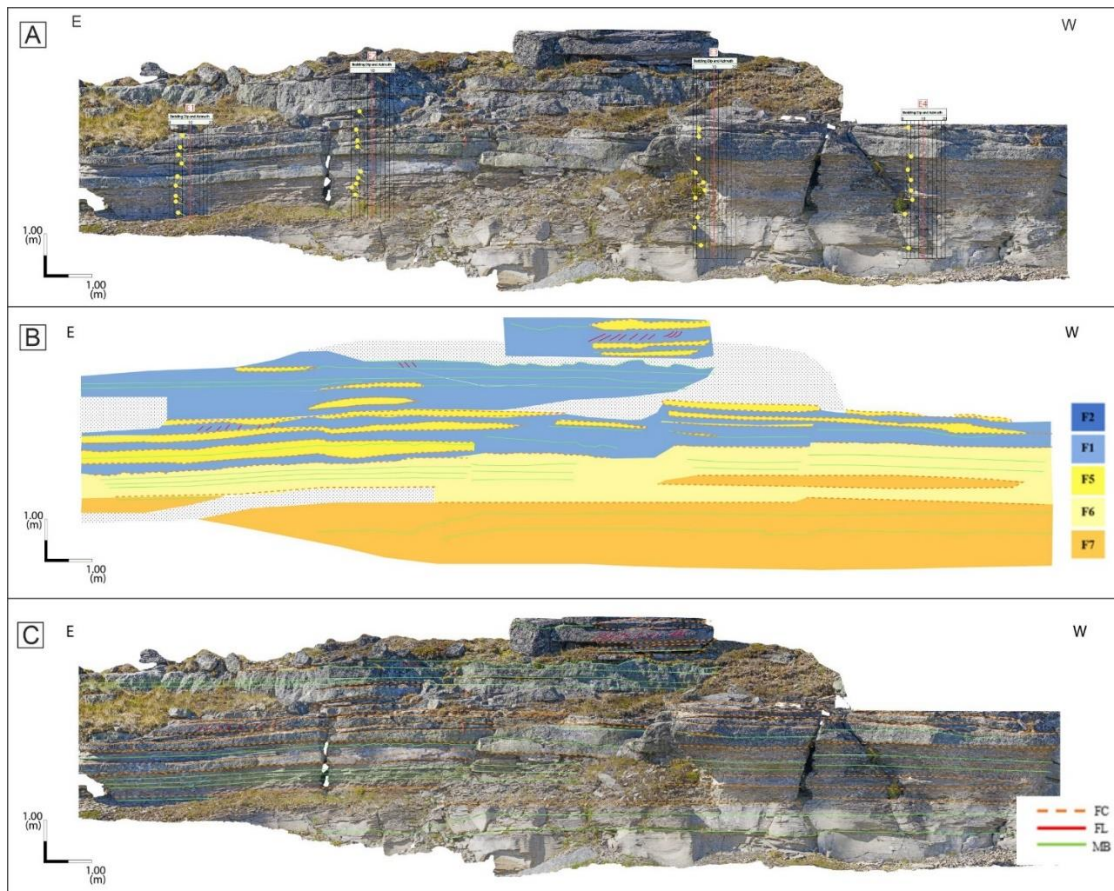


Figure 2.13. Photomosaics of East Ridge outcrop. **A)** Photomosaic shows tadpole measurements indicating SE and NW directed dip directions. This measurements inconsistency resulted by folding of the ridge. **B)** Facies shading of East Ridge outcrop, eastwards increasing abundance of sandstone lenses is observable. Gray hatched parts are covered with vegetation. The legend indicating facies colors is provided on the right. **C)** Interpreted photomosaic of East Ridge; green lines represent bedding contacts, orange dashed line represents facies contacts and red lines showing foreset laminae. Conglomerate facies thicknesses decreased compared to west ridge on the other hand sandstone facies (**F6-F7**) show an increase in thickness (**FC**: Facies Contacts, **FL**: Foreset Laminae, **MB**: Master Bedding surfaces)

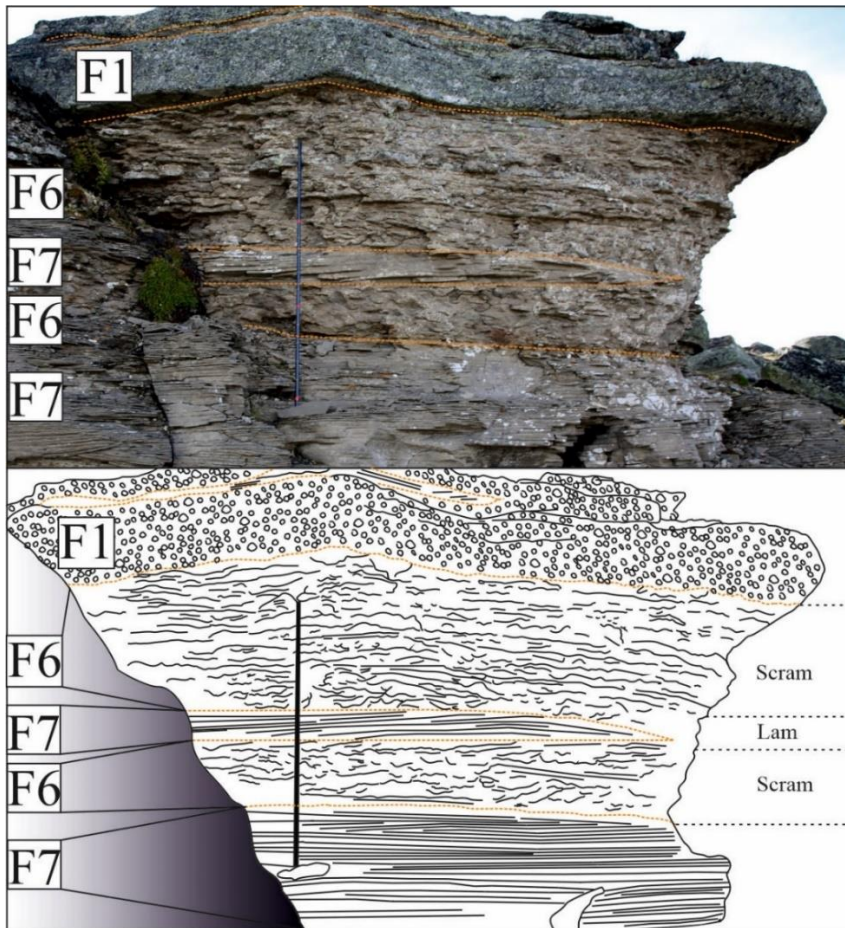


Figure 2.14. Photograph and sketch of Lam-scam bedding observed on East Ridge indicating fair-weather or waning storm conditions (scram) prevailing after strong storm events (lam). Scoured contact surface between conglomerate facies (**F1**) and bioturbated sandstone facies indicating deposition by sediment laden gravity flows formed during major storms resulted in river flooding. Soft sedimentary deformational structures and gutter casts are observable locally along contact surface. Orange dashed line represents facies contacts. Stick is 1.50 meters in length.

2.4.3 South Ridge

This outcrop is located at the south-eastern side of the West and East ridges (Fig. 2.3) and is east-west elongated. Master bedding plane measurements indicate north-west dip direction. Foreset laminae orientation measurements performed on large-scale cross-stratified sandstone facies (**F4**) (Fig. 2.7D) and cross-stratified sandstone facies with coal fragments (**F3**) (Fig. 2.7C) indicate a dominant westward palaeoflow (Fig. 2.8).

Six different facies were observed on the South Ridge (Table 2.2), (Figs. 2.7, 2.15, 2.16). From base to top the section consists of low-angle, parallel-laminated, muddy, very fine-grained sandstone (**F8**) erosively overlain by massive to planar-stratified, moderately sorted chert conglomerate (**F1**) (Fig. 2.17C). The muddy sandstone unit is rich in organic laminae and composed of very poorly-sorted, angular to subangular grains (Fig. 2.7H). Massively bedded conglomerate is overlain by low-angle, sub-parallel HCS laminated, silty-sandstone (**F7**). Above the laminated silty-sandstone facies (**F7**) there is a locally occurring, conglomeratic, large-scale, cross-stratified sandstone facies (**F4**) up to half a meter in thickness. Large-scale, cross-bedded sandstone facies overlie the low-angle, planar-laminated sandstone beds. North-south orient channelized, pebbly structures crosscut the low-angle planar cross-stratified sandstone facies (**F5**) (Figs. 2.16B, 2.17B). At the top of the section the bidirectional cross-stratified sandstone facies with coal fragments (**F3**) erosively overlies the dune scale cross-stratified sandstone facies (**F4**) (Figs. 2.16A, B, C, 2.17A). Two stratigraphic sections measured on the South Ridge are referred as Section D and Section E. In measured Section E, 10 cm thick, discontinuous lenses of laminated, organic-rich mudstone units interbedded with (**F7**) overlies conglomerate facies (**F1**). These laminated mudstone horizons are not observed in Section D. Up to 15-meter-thick ironstone concretions are frequently observed as discontinuous lenses within conglomerate (**F1**) and laminated silty-sandstone (**F1**) units (Fig. 2.17C). This ridge lacks bioturbation. Only rare occurrences of *Macaronichnus* isp. were observed in **F8** and possible cryptic bioturbation is observed in facies **F3**, **F5** and **F4**.

Section E is located west of section D, at the western side of the South Ridge. Detailed lithologic logs for Sections D and E are presented in Figure 2.15.

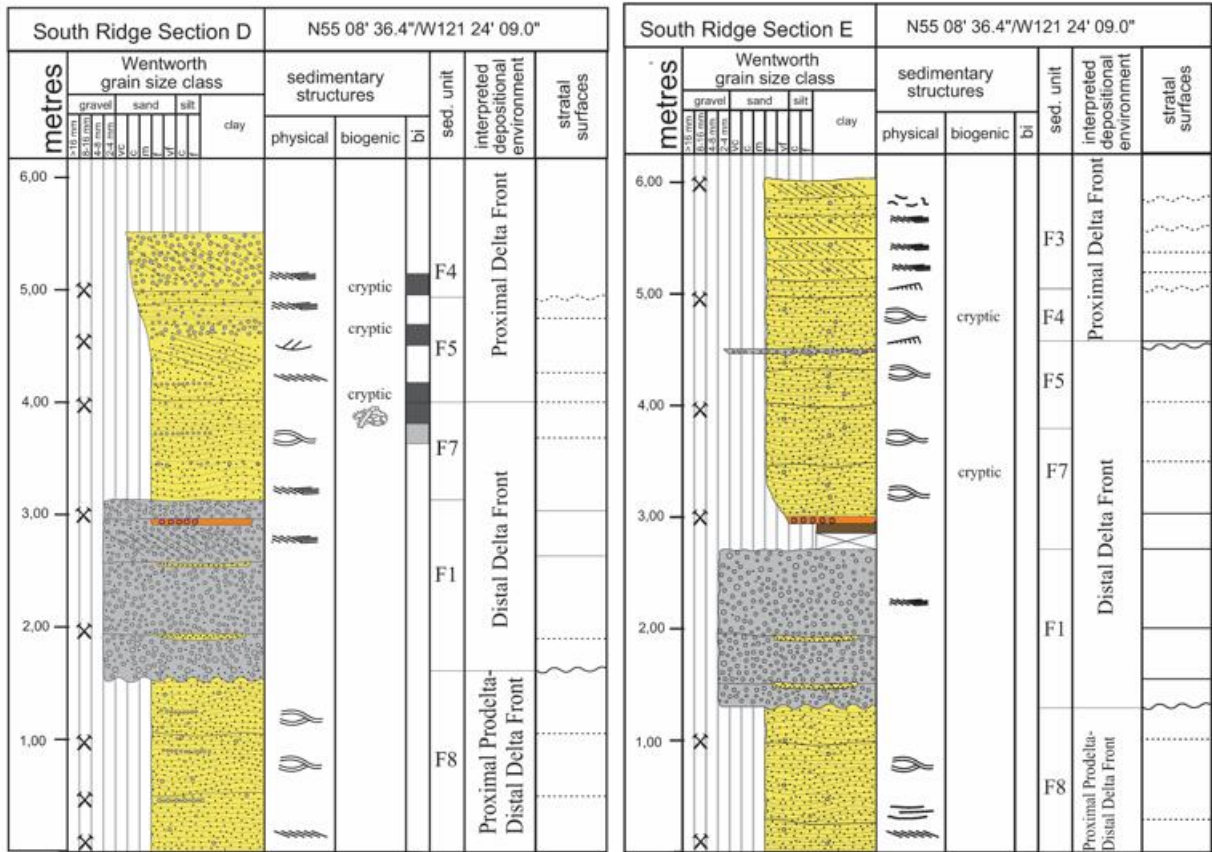


Figure 2.15. Lithologic strip logs representing facies thicknesses measured on South ridge outcrops. On South Ridge, conglomerate abundance is lowest. This site is different than the west and east outcrop successions. Mudstone, ironstone lenses and the stratigraphic section is capped by terminal distributary channel deposits. Overall facies showing low to no bioturbation unless cryptically bioturbated (Symbols and lithofacies patterns as in legend in Figure 2.9).

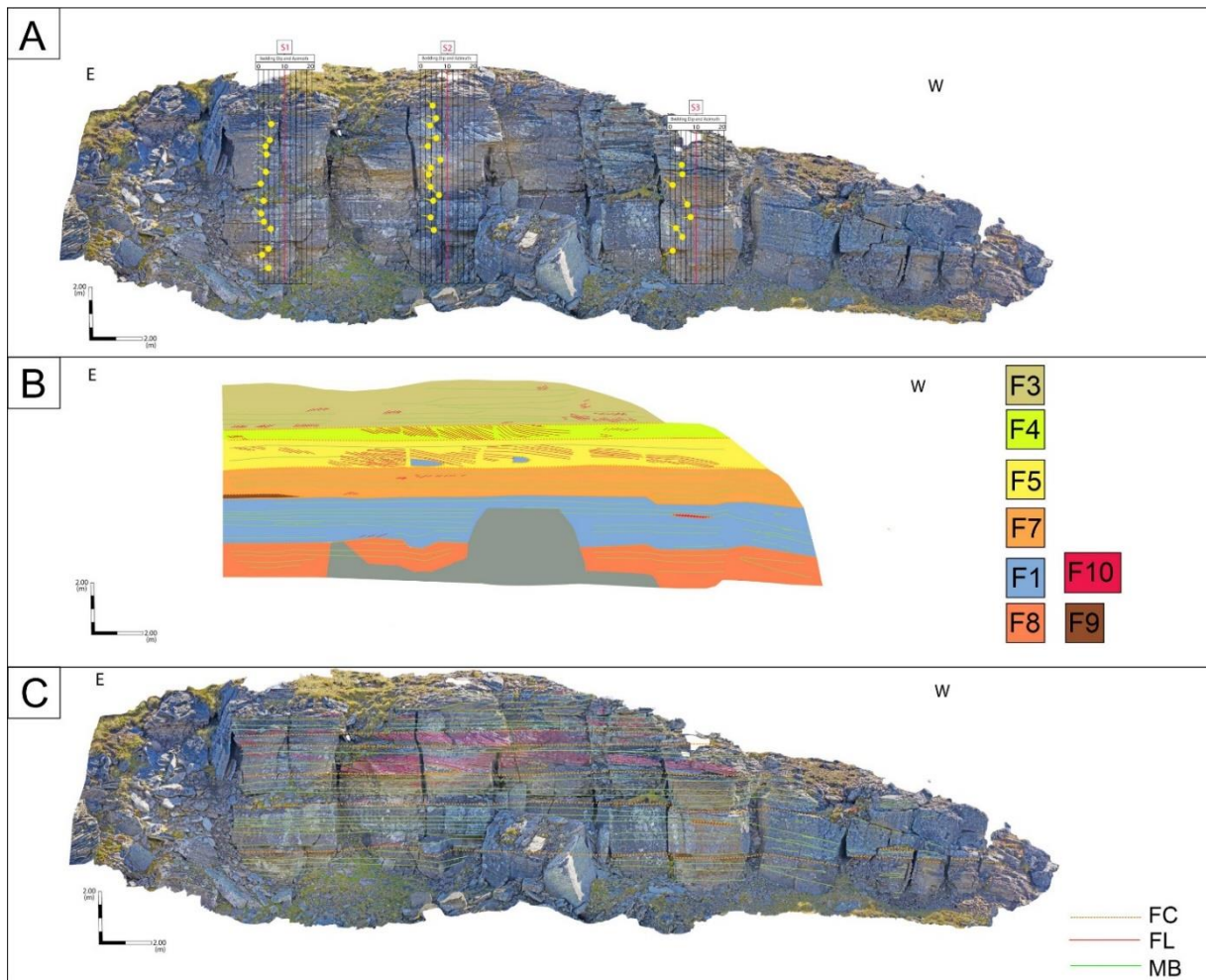


Figure 2.16. Photomosaics of South Ridge outcrops. **A)** Tadpole plots located on ridge indicating measurements taken from masterbedding surfaces. **B)** Facies shading observed on South Ridge. Legends are provided on right. gray hatch represents vegetation cover and fragmented block of rocks. **C)** Interpreted version of photomosaic master bedding planes are indicated with green lines, red lines show foreset laminae and orange dashed line represents facies contacts.

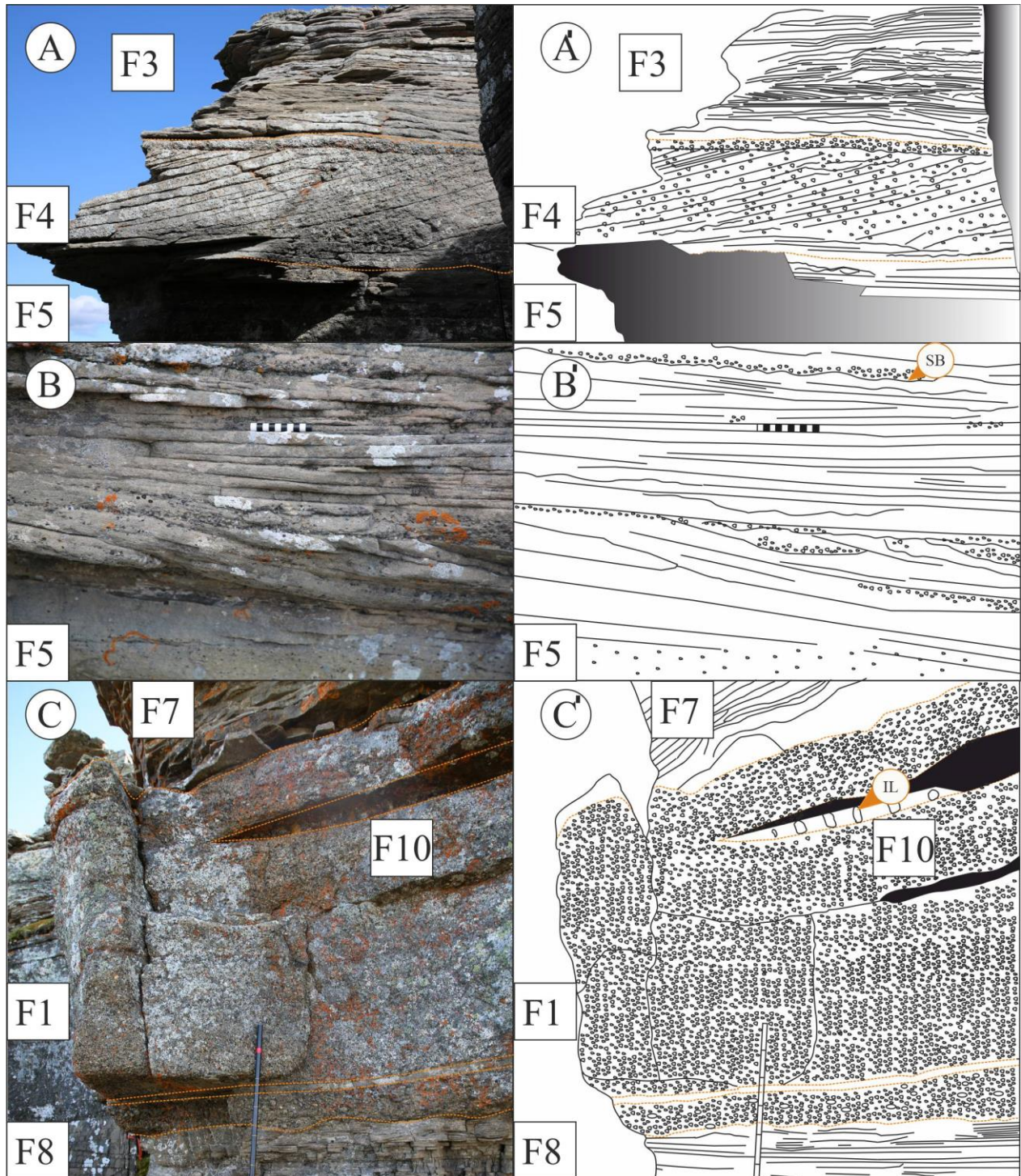


Figure 2.17. Selected facies photos and interpretation sketches from South Ridge outcrop. **A-A')** Swaley cross stratified sandstone (**F5**) overlain by conglomeratic sandstone dunes (**F4**), **F4** is half a meter in thickness. Conglomeratic sandstone dunes are overlain by subaqueous terminal distributary channel sandstone (**F3**) with a scoured contact. **B-B')** Swaley cross stratified

sandstones with pebbly storm lags and internal erosion surfaces due to erosional storm bed amalgamation. Zebra stick is 10.00 cm in length. C-C') Massive conglomerate facies (F1) erosively overlies muddy sandstone facies (F8); ironstone lens is observable within delta front conglomerate facies (F1) overlain by HCS sandstones (F7) black Jacob's stick is 10.00 cm in length for each part.

2.5 Interpretations

Each Ridge shows a distinct sedimentological architecture with different types and distributions of facies. The West and East ridges consist of similar facies with varying thicknesses whereas the South Ridge represents the highest level of lateral facies variation.

2.5.1 Facies Associations

Three facies' associations are identified from the studied outcrops: (1) Distributary Mouth Bar (FA1), (2) Delta Front (FA2), (3) Prodelta (FA3). Their constituent facies and a summary interpretation for each Facies Association are included as Table 2.3. Facies interpretations are below (Section 2.5.2).

Table 2.3. Summary of facies associations described in Falher D parasequence observed at Mount Spieker outcrops.

Facies Description	Interpretation	Facies Association
<p>F2</p> <p>Cross-stratified conglomerate</p>	<ul style="list-style-type: none"> • Abundant planar cross bedded units with irregular contacts and locally bidirectional pattern indicates deposition under shoaling storm-waves. • Thick conglomerates with erosive contacts indicate mouth bar deposition. • Local bimodal open framework texture indicates wave reworking. • Absence of bioturbation is attributed to high levels of hydraulic energy. • Represents prograding storm bars/ridges at proximal delta front (mouth bar). 	<p>FA1</p> <p>Distributary Mouth Bar</p>
<p>F1</p> <p>Massive to planar stratified conglomerate</p>	<ul style="list-style-type: none"> • Scoured bottom contact of conglomerate indicates deposition under gravity induced sediment laden hyperpycnal flows formed during relative sea level lowering and river flood or storm processes. • Recurring storm events resulted in deposition of F1-F5 tempestite couplets. • Thinning towards East indicating deposition under eastwards flowing longshore currents. • Absence of trace fossils due to high hydraulic energy and sedimentation rates combined with freshwater input at delta front. • Represents deposition at proximal to distal delta front (distal mouth bar) setting. 	<p>FA2 Delta Front</p>
<p>F3</p>	<ul style="list-style-type: none"> • Distributary terminal channel deposits in a current dominant environment. • Represents deposition at proximal delta front 	

Cross-stratified sandstone with coal fragments		
F4 Locally conglomeratic cross-stratified sandstone	<ul style="list-style-type: none"> • Deposition under shoaling storm-waves. • Large scale cross bedding represents planar to sinuous crested storm ridges or bars. • Increasing and reducing abundances of pebble clasts indicating changing storm intensity. • Represents deposition at proximal delta front 	
F5 Low-angle planar cross-stratified sandstone	<ul style="list-style-type: none"> • Deposition under storm-waves within SWB • On South Ridge N-S aligned (shore normal) channelizing pebbly structures interpreted to be formed due to storm rip currents. • Represents deposition at proximal to distal delta front. 	
F9 Organic rich mudstone	<ul style="list-style-type: none"> • Seasonal hypopycnal buoyant plumes or post storm suspended sediment fall out. • Fluid mud deposition due to high flocculation rates. • Plant fragments indicating phytodetrital pulses. • Represents deposition at proximal to distal delta front 	
F10 Ironstone	<ul style="list-style-type: none"> • Indicate freshwater (riverine) input. • Represents deposition at proximal to distal delta front 	
F6	<ul style="list-style-type: none"> • Deposition under storm-waves above SWB below FWWB. 	FA3 Prodelta

<p>Highly bioturbated silty-sandstone</p>	<ul style="list-style-type: none"> • Lam-scam bedding represents recurring storm events and following fair weather conditions. • Preserved carbonaceous laminae represents high sedimentation rates and riverine input. • Facies crossing elements of <i>Cruziana</i> and <i>Skolithos</i> ichnofacies are representing stressed version (low diversity high intensity) of Proximal <i>Cruziana</i> facies. • Opportunistic colonization. • Fossil wood preservation indicates terrigenous input and river flooding event. • Discontinuous pebble lenses are interpreted as storm lags. • Represents deposition at proximal prodelta to distal delta front. 	<p>FA3 Prodelta</p>
<p>F7 Low-angle parallel laminated silty-sandstone</p>	<ul style="list-style-type: none"> • Deposition under storm-waves supported by HCS bed-sets, • Suspended load transport increasing basinward due to elevated water turbidity by storm events inferred by thickening of sandy layers basinward. • Burrower meiofauna may transported to deep water in turbid water during storm events. • Conglomerate lenses interpreted as storm lags. • Scour and fill bedding and internal truncation surfaces represent erosional amalgamation of storm beds. • Represents deposition at proximal prodelta to distal delta front 	
<p>F8 Muddy sandstone</p>	<ul style="list-style-type: none"> • Suspension settling from turbid waters. • Represents deposition at proximal prodelta to distal delta front 	

2.5.2 Facies Interpretations

Facies 1

Massive to planar stratified conglomerate facies are observed on all ridges in varying thicknesses. Facies 1 is more abundant towards the west and decreasing eastwards, this trend of facies distribution is linked to proximity to sediment source, such as a river-mouth point source (Leckie, 1986). The moderately to poorly sorted (Fig. 2.7A), thick conglomerate beds with sparsely distributed elongated clasts (of **F1**) are also likely proximal to a fluvial sediment source (e.g., Freidman, 1961; 1967). Facies 1 erosively overlays the highly bioturbated silty-sandstone facies (**F6**), low angle parallel laminated silty-sandstone facies (**F7**) and muddy-sandstone facies (**F8**) on different ridges. The contact between these facies is characterized by moderate-scale (5-15 cm) gutter casts and abundant soft-sediment deformational structures, which are associated with rapid deposition of the conglomerate facies (**F1**) by gravity induced sediment-laden hyperpycnal flows in a delta front setting (e.g., Bhattacharya and MacEachern, 2009). These hyperpycnites were possibly initiated during major storm-related river-flooding events (Harms et al., 1975; Hamblin and Walker, 1979; Dott and Bourgeois, 1982; Mutti et al., 2003; Morsilli and Pomar, 2012). Massive bedding and normal to inverse grading observed in conglomerate facies (**F1**) is typical for deposits formed under waning then waxing hyperpycnal flows (e.g., Mulder et al., 2003; Olariu et al., 2010; Buatois et al., 2011). The preservation of abundant fossil-wood fragments near the **F7- F1** contact confirm rapid sedimentation and burial, and a fluvial sediment source (e.g., Yang et al., 2015) (Plink-Bjorklund and Steel, 2004; Petter and Steel, 2006; Myrow et al., 2008; Zavala et al., 2012 a; b). Conglomerate facies (**F1**) are interbedded with upwards-thinning and discontinuous low-angle cross-stratified, upper fine to medium-grained sandstone beds and are interpreted as swaley cross-stratification (SCS) (Fig. 2.11E). The absence of trace fossils within these facies is attributed to high hydraulic energy and sedimentation rates potentially combined with freshwater input near the delta front. In summary, these facies are interpreted to represent deposition in a wave dominated proximal to distal delta front (distal mouth bar) setting.

Facies 2

At the top of the depositional sequences of the West and East ridges, dune-scale cross-stratified conglomerate facies (**F2**) overlie massive to planar stratified conglomerate beds (**F1**). Cross-stratified conglomerate facies (**F2**) have 15-30 cm thick bed-sets with irregular and scoured bedding contacts. The abundance of matrix decreases upwards. At the upper levels where conglomerate facies (**F2**) are grain supported (Fig. 2.7B), they show an open framework texture. The coarsening upwards trend possibly indicates post depositional reworking of sediment by longshore currents and wave winnowing. Also storm erosion of ridges or reworking under low-amplitude storm-waves caused low-angle planar and scoured bedding contacts for ridges or scoured bedding contacts of storm bars might represent intermittent subaerial exposure after storm events (e.g., Caddel, 1999). Rare bidirectional cross-stratified patterns of storm bars are linked to obliquely shoreward shoaling storm-waves with different angles deflected to variable directions parallel to shoreline (Greenwood and Mittler, 1985; Davis and Clifton, 1987; MacEachern et al., 2012). The cross stratified conglomerate facies are interpreted as prograding storm ridges / bars, which were likely deposited as distributary mouth bars that were subsequently reworked by eastwards flowing storm-wave induced longshore currents (Leckie and Walker, 1982; Clifton, 2003). Palaeocurrent measurements are consistent with eastwards flowing alongshore currents (Fig. 2.11). In summary, the conglomerate facies of **F2** are interpreted as storm ridges, which were deposited as mouth bars by river, and subsequently reworked by eastwards flowing storm-wave induced longshore currents confirmed with rose plots (Leckie and Walker, 1982; Clifton, 2003) (Fig. 2.11).

Facies 3

Facies 3 is observed at the upper stratigraphic levels of the South Ridge. The sandstone beds of **F3** are current-rippled, fine upwards, and contain dm-scale cross-stratified sandstone beds. The increasing abundance of current ripples in the upper parts of the section indicates current-dominated sedimentation with flow energy decreasing upwards (e.g., Morshedien et al., 2011). Also, abundant coal fragments are noted (Fig. 2.7C) (**F3**). The presence of coal suggests a fluvial influence: coal fragments are likely derived from a riverine source. This combination of shallowing upwards sedimentation, the presence of fresh water and the proximity to a point

source are all consistent with the terminus of a distributary channel and the distributary mouth bars therein.

Terminal distributary channels are the most distal part of distributary channels in deltaic system they can extend into subaqueous delta front (Olariu and Bhattacharya, 2006). Scoured contacts (Fig. 2.17A) of the cross stratified bed-sets within these facies (**F3**) further supports the interpretation of **F3** as terminal distributary channel deposits (Olariu and Bhattacharya, 2006).

Facies 4

Facies 4 overlies swaley cross stratified sandstone facies (**F5**) with a sharp basal contact on South Ridge. The large-scale, cross-stratified, locally conglomeratic sandstone beds are interpreted as sinuous to straight-crested, subaqueous storm bars (**F4**) (Fig. 2.16B). Sinuous crested subaqueous dunes indicate deposition by interaction of a deflected shore-normal current that became nearly parallel to shoreline and shore normal currents generated by storm waves in the proximal delta-front setting (e.g., Pemberton and MacEachern, 1997; 2012).

Facies 5

Low-angle planar cross stratified to planar-parallel laminated sandstone beds of **F5** occur as discontinuous lenses interbedded with conglomerate facies (**F1**) on West Ridge. However, **F5** is present as continuous sandstone beds on East and South ridges. The laminae are gently dipping (10-15 °) or downwards concave surface. These beds are interpreted as swaley cross-stratification (SCS). Swaley cross-stratification, which is interpreted to be truncated hummocks in HCS, reflects higher energy storm deposition in shallower settings compared to HCS (Leckie and Walker, 1982). The lens style geometry and southward decreasing abundance of SCS sandstone facies (**F5**) likely is related to their bathymetric position within the delta front: i.e., positioned on slightly deeper parts of the delta (Fig. 2.10B). Each interbedded conglomerate (**F1**) – sandstone (**F5**) facies pair is interpreted as coarse-grained proximal tempestite couplet (after Aigner, 1985; Einsele, 1982; 1991; Myrow, 1992; Myrow and Southard, 1991) representing a single storm event. Storm event starts with the transportation and deposition of coarsest-grained units (**F1**) followed by the deposition of sandy facies (**F5**) due to suspension settling of sandstone during the

waning stages of the storm. The presence of abundant pebbly lags, amalgamated HCS sandstone, massive to normally graded conglomerate (**F1**) and SCS sandstone (**F5**) tempestite couplets, and irregular sharp bedding contacts of facies are also linked to sudden and recurring storm event deposition.

On South Ridge **F5** overlies **F7**, and erosive contacts support erosional amalgamation under sudden and recurring storm events (e.g., Jelby et al., 2020) (Fig. 2.16B). Shore-perpendicular (N-S directed), pebbly, channelized structures observed in SCS sandstone (**F5**) are interpreted to be deposited in storm rip channels on South Ridge (Figs. 2.16 B, C). The rip channels are formed by rip currents which are generated by water returning from shallow parts of the shoreface during storm let down (Greenwood and Mittler, 1985; Davis and Clifton, 1987; Pemberton et al., 2012). Westerly migration of these channels is observable on the photomosaic as channel scours shifting westwards and the preferential preservation of west-oriented foresets in these shallow subaqueous “channels” (Fig. 2.16B). This migration also supports the dominant westerly flow in depositional setting. The interpretations provided above show that **F5** accumulated within wave base and is interbedded with conglomerate beds (**F1**) Considering that only cryptic bioturbation is observed (see below), it is likely that freshened water was commonly present in the sedimentary environment. These characteristics and the clear NNW progradational nature of the studied strata well support the interpretation of a wave dominated proximal to distal delta front setting.

Facies 6

Facies 6 was observed on West and East ridges. In this bioturbated silty-sandstone facies (**F6**) the primary sedimentary structures are obscured by biogenic reworking. Wavy-parallel lamination, and low-angle sub-parallel HCS is observed where bioturbation intensity is low. Hummocky cross-stratification reflects storm reworking by wave oscillations, and thus occurs within storm wave base (Harms et al., 1975; Dott and Bourgeois, 1982; Dott, 1983; Walker et al., 1983; Myrow, 2008; Morsilli and Pomar, 2012).

Poorly - sorted pebbly lenses, up to ~2 cm thick, filling swales or aligning along swale laminae are abundant in the HCS bed-sets. Pebbly lenses and laminae are interpreted as storm lags, which are evidence of strong and sudden storm events (Dott and Bourgeois, 1982; Hunter and Clifton, 1982) (Fig. 2.11A). An upwards shift, from erosively-amalgamated HCS silty-sandstone beds (**F7**) to highly bioturbated wavy parallel laminated sandstone beds (**F6**) indicates

changing storm-wave influence on the seabed. Frequent storm-reworking did not allow the preservation of shallow tier burrows, but rather favored the deposition of amalgamated tempestite beds. On the other hand, fair-weather deposition favored the preservation of bioturbation (MacEachern and Pemberton, 1992; Gingras et al., 1998; Buatois et al., 2008). The thickness of the bioturbated silty-sandstone facies (**F6**) decreases towards the south (palaeolandward), likely because increasing hydraulic energy with shoaling led to the preservation of storm beds over bioturbated fair-weather units (MacEachern et al., 2012). Also, closer to the river mouth (landward) salinity and temperature fluctuations causes unfavorable conditions for burrowing infauna (MacEachern and Pemberton, 2009). The bioturbated silty-sandstone facies (**F6**) is also intercalated with low angle planar laminated silty sandstone facies (**F7**) the on West and East ridges and are interpreted as lam-scam bedding (*sensu* Howard, 1972) indicating storm events followed by fair weather deposition. The thickness of bioturbated sandstone (**F6**) is greater on East Ridge (appx. 80.00 cm *versus* 120.00 cm). This trend suggests that East Ridge contains bathymetrically deeper facies or is comparably sheltered. The abundance of carbonaceous laminae within these facies (**F6-F7**) indicates a continental source of coalified detritus and evidence rapid sedimentation resulted in the preservation of continentally-derived organic detritus carried basinward during heightened river discharge (Coates and MacEachern, 2007). Riverine input also evidenced by abundance of clay and silt size material within facies (**F6-F7**) (Reading and Collinson, 1996; Coates and MacEachern, 2007; Dafoe et al., 2010). Common HCS indicates deposition within storm wave base, minor conglomerate lenses and laminae and abundant organics are likely sourced fluvially, and the distribution of bioturbation shows an alternation between storm- and fair-weather sedimentation. The higher abundance of sandy facies towards the north was caused by bypassing of fine sediments (i.e., sand) into delta sandstone lobes in a basinal direction (Myrow, 1992). In deltaic settings catastrophic flood events can generate sediment- water mixed hyperpycnal flows (Bates, 1953; Zavala et al., 2021), which is then deposited as delta-front sandstone lobes (Mutti et al., 2000; 2003).

Facies 7

At the base of the West and East ridges silty-sandstone facies (**F7**) are interbedded with bioturbated sandstone facies (**F6**). This facies distribution indicates the alternation between storm- and fair-weather wave reworking. On South Ridge, **F7** overlies **F1** and shows no

intercalation with **F6**. Along the tempestite intervals, where there is no erosional amalgamation, occurrences of ripple laminae indicate waning stages of storm events (Kumar and Saunders, 1978). The abundance of continentally-derived organics within **F7** may be linked to heightened sedimentation and burial rates during storm events. Abundant clay-silt size material within **F7** likely indicates a fluvial source of sediment. The interpretations provided above are most consistent with **F7** sedimentation occurring within storm-wave base. Facies 7 is interbedded with prodeltaic **F6**, and owing to the presence of bioturbation, is interpreted as shallow marine. Considering that overall **BI** and trace fossil diversity are low, it is likely that intermittent changes in the amount of salinity took place at the time of deposition, due to the presence of a fluvial point source. These characteristics well support the interpretation of wave dominated proximal prodelta to distal delta front setting.

Facies 8

Muddy sandstone facies (**F8**) is only observed at the lowest level of the South Ridge. Moderate sorting, the presence of angular to sub-angular clasts, and the abundance of terrestrial organic detritus indicate a greater influence of fluvial sedimentation compared to the other localities (West and East ridges) (Freidman, 1961; 1967). Low-angle planar laminae sets are interpreted as HCS. Storm-wave reworking combined with fluvial indicators represent deposition in a proximal prodelta (e.g., Bhattacharya and Walker, 1992; Mutti et al., 2003).

Facies 9

Facies 9 occurs as discontinuous lenses interbedded with silty-sandstone facies (**F7**) on South Ridge. Mudstone facies (**F9**) rich in phytodetrital fragments (Fig. 2.7I). These mudstone lenses are interpreted as fluid muds. Fluid muds may deposit in a delta front setting either as post-storm fall-out sediment or by seasonal river plumes (Allison et al., 2000; Bhattacharya, 2006; Bhattacharya and MacEachern, 2009). Flocculation due to mixing of sediment-laden freshwater with seawater is the main process of deposition of mudstone lenses in delta front settings (e.g., McAnally et al., 2007; Bhattacharya and MacEachern, 2009). The suspension fall-out from storm-induced flows is probably the best interpretation since rapid flocculation and high sedimentation rates are required to deposit fluid muds in a delta front setting (Neill and Allison, 2005).

Fluid muds are likely to be structureless, centimeter to decimeter thick beds lacking bioturbation but including variable amounts of organic material, interbedded with sandstone or siltstone beds (Kuehl et al., 1986; Allison et al., 2000; MacEachern et al., 2005). The laminated structure of **F9** is possibly the result of strong wave agitation (e.g., Ichaso and Dalrymple, 2009). Facies 9 is likely derived from a riverine source due to their high, phytodetrital content (Bhattacharya and MacEachern, 2009). High siderite content might be linked to fluvial input to the system (Akinlotan, 2019).

Facies 10

Ironstone facies (**F10**) occurs as ~ 5-15 cm thick concretion-rich lenses within **F7** and **F1** on South Ridge. XRD results show high kaolinite, chlorite and silica peaks and indicate a mudstone origin of **F10**. The major iron mineral is goethite, which is deposited under oxidizing conditions. The kaolinite and silica are potentially indicators of fluvial inflow as terrestrial sourced detrital. The Fe to form goethite was most likely from the chlorite mineral.

2.6 Ichnofacies Interpretations -West, East, and South Ridges

The relative dominances of fluvial, wave and tidal processes influences trace fossil diversity and distribution. Ichnology can used to identify environmental factors such as salinity, hydrodynamic energy, oxygenation, sediment input and temperature (e.g. Pemberton et al., 1992; Taylor et al., 2003; Dafoe et al., 2010). Individual ichnospecies observed in Falher D parasequence are listed and described in Table 2.4.

Table 2.4. List of trace fossils, morphologies, ethologies, and environmental indications and observed on Falher D outcrops.

Trace Fossil	Morphology and Occurrence in Falher D Member	Ethology	Typical Environment	Ichnofacies	Main References
Ma <i>Macaronichnus</i> isp. "Paramacaronichnus"	Horizontal to aligned cylindrical irregularly meandering branching and cross cutting high density burrows with moderately contrasting fill with dark mantle 1.00 cm in diameter and several cm long. Branching and cross cutting behavior and lesser grain segregation differs "Paramacaronichnus" burrows from <i>Macaronichnus</i> isp.	Deposit-feeding of opheliid polychaetae feed on the microbes on the surface of quartz grains and segregating dark-colored grains.	Foreshore, delta front, shoreface environments.	<i>Skolithos</i> Ichnofacies.	Clifton and Thompson 1978; Gingras et al. 2002; Seike 2007; Dafoe 2009; Bromley et al. 2009; Pemberton et al. 2012
Di <i>Diplocraterion</i> isp.	U shaped, vertical, passively filled spreite burrows, densely located at top of the HCS sandstones several cm in size, abundantly observed on West and East ridges.	Suspension-feeding and dwelling behavior of polychaetae worms considered as deposit-feeding.	Marginal-marine environments.	<i>Skolithos</i> Ichnofacies can also occur in <i>Glossifungites</i> Ichnofacies.	Torell, 1870; Fürsich 1974b
Ro <i>Rosselia</i> isp.	Subvertical, bulbous-shaped burrows with muddy fill several cm in size, rarely observed on West and East ridges.	Detritus-feeding polychaetae dwelling behavior.	Lower, middle shoreface, marginal-marine settings.	<i>Cruziana</i> Ichnofacies also associated with <i>Skolithos</i> Ichnofacies.	Dahmer, 1937; Nara 1995

Sch <i>Schaubcylindrichnus</i> isp.	Burrows with a thick light-colored lining oriented in different directions, less than a cm in diameter, moderately observed on West and East ridges.	Funnel-feeding behavior, worms.	Common in Lower shoreface and offshore environments.	<i>Cruziana</i> and <i>Skolithos</i> ichnofacies transitional element.	Frey and Howard 1981; Frey and Pemberton; Nara 2006
Pl <i>Planolites</i> isp.	Simple horizontal actively filled burrow without lining, rarely observed on West and East ridges.	Worm like animals, arthropods, and molluscs.	All aquatic environments.	<i>Cruziana</i> and <i>Skolithos</i> Ichnofacies transitional element.	Nicholson 1983; Pemberton and Frey 1982
Rh <i>Rhizocorallium</i> isp.	Horizontal U- shaped spreite burrow, rarely observed on West and East ridges.	Suspension and deposit feeding behavior polychaetae burrow.	Marine, marginal marine, shelf, fluvial environments. High energy, shallow water, marginal marine environments.	<i>Cruziana</i> and <i>Glossifungites</i> Ichnofacies.	Zenker 1836; Uchman and Rattazzi 2016
Sk <i>Skolithos</i> isp.	Passively filled horizontal tubes, several cm in length, rarely observed on West and East ridges.	Dwelling behavior, suspension feeding organism.	Deltaic and marginal-marine environments.	<i>Skolithos</i> Ichnofacies.	Haldeman 1840; Alpert 1974
Te <i>Teichichnus</i> isp.	Vertically aligned spreite burrows without marginal tube, moderately observed on West and East ridges.	Deposit feeding behavior of worm like organisms.	Deltaic and marginal-marine environments.	<i>Cruziana</i> and <i>Zoophycos</i> Ichnofacies.	Seilacher 1955
Ct <i>Cryptic</i>	Less than a millimeter scale sinuous vertical and horizontally aligned quartz filled burrows, locally high abundance with low diversity fabric was observed on all ridges.	Feeding behavior of meiofauna.	Aquatic environments.	<i>Skolithos</i> and <i>Cruziana</i> Ichnofacies.	Howard and Frey 1975; 1985; Pemberton et al. 2008

2.6.1 Ichnofacies Interpretation of Distributary Mouth Facies Association (FA1)

At the top of the West and East Ridge sections, cross-bedded conglomerate facies (F2) are interpreted as mouth bar deposits. Facies 2 is unburrowed. The wave and fluvial energy were highest near river mouth resulting in salinity, temperature fluctuations, high hydraulic energy, and variable substrate consistency limited viable lifestyles in these deposits (MacEachern and Hobbs, 2004; Gani et al., 2004; MacEachern, 2005; Bhattacharya and MacEachern, 2009). Also, the colonization windows, under sporadically high sedimentation rates at mouth bars, limited colonization windows for benthic communities (Tonkin, 2012).

2.6.2 Ichnofacies Interpretation of Delta Front Facies Association (FA2)

The overall delta front facies display low diversity trace fossil suites, and except where cryptically bioturbated, show low BI values (BI 1-0). Cryptic bioturbation is caused by disturbance of grains and laminae by microscopic, mm scale infauna (Dashtgard et al., 2008; Greene et al., 2012). The massive to parallel-laminated conglomerate facies (F1) do not show any discernible bioturbation. However, SCS sandstone facies (F5) overlying tempestite couplets, are interpreted to be cryptically-bioturbated (Fig. 2.19I). Similar cryptically-burrowed SCS (F5) and subaqueous dunes (F4) have previously been identified in deltaic settings characterized by sporadic bioturbation within wave-dominated delta front deposits (Tonkin, 2012). Although some workers have interpreted similar features to reflect sediment dewatering, thin section analyses in this study (discussed above) clearly shows that these were produced by infauna. In contrast to the West and East ridges, on the South Ridge overall bioturbation indices are very low (BI 1-0) except for a few cryptically-bioturbated levels. In the silty-sandstone facies (F7), interpreted to be deposited in a distal delta front setting, rare *Macaronichnus* isp., *Schaubcylindrichnus* isp. traces and sporadically distributed cryptic- bioturbation are observed (Fig. 2.18C). Locally cryptic bioturbation was also observed in lithofacies interpreted to represent deposition in a high-energy proximal delta front (lithofacies F3) (Fig. 2.19G). The lack of bioturbation on this ridge is ascribed to higher freshwater input on the south-eastern side of the deltaic system. Higher wave energy counterparts (West and East ridges) create better environmental conditions for burrowing organisms since fluvial influence is weaker compared to South Ridge. The presence of unburrowed mudstone lenses (F9) (Fig. 2.7I) intercalated with bioturbated silty sandstones (F7) on South Ridge suggests that those mudstone lenses were deposited as soupy, fluid muds. The

crude mottling and destruction of burrows in soupy substrates is possibly the reason of unborrowed texture of these fluid mud lenses (Bromley, 2009; Bhattacharya and MacEachern, 2009).

2.6.3 Ichnofacies Interpretation of Prodelta Facies Association (FA3)

Facies deposited within prodelta settings show the highest burrow diversity and intensity on West and East ridges. Hummocky cross-stratified silty-sandstone facies (**F7**), deposited in a proximal prodeltaic setting, show sporadically distributed vertical and horizontal, sinuous, quartz-filled, mm-thick, cryptic-bioturbation, and rare *Schaubcylindrichnus* isp. burrows (Fig. 2.18C). This type of bioturbation commonly presents a ‘fuzzy’ texture, which blurs laminae due to small scale grain displacements (Pemberton et al., 2008). Local distribution of microscopic laminae and micro-scale grading disruptions with horizontal and vertically aligned sinuous tubular structures provide evidence for cryptic bioturbation (Fig. 2.19G, H, I, J). The random orientation (including horizontal), sinuous shapes, and consistent diameters of the tubes excludes fluid escape or other soft-sediment deformation features (Greene et al., 2012). For cryptically burrowed intervals within facies (**F7**), the bioturbation index (**BI**) is 5. Notably the bioturbated intervals are sporadically distributed. The distribution, along with low diversities of trace fossils in the prodelta, may have resulted from several physico-chemical stress conditions including salinity changes, elevated turbidity, and sedimentation rates due to storm and river flooding events (Bhattacharya and MacEachern, 2009).

Cryptic burrows occur primarily in high-energy shallow marine environments (proximal upper shoreface and foreshore) (Saunders et al., 1994), but during storm events burrowing meiofauna can be carried to deeper waters in association with the sediment that they occupy (Butman, 1987). Storm-waves introduce oxygenated water to the substrate, and allow infauna to colonize these sediments (e.g., Gingras et al., 2002; Bhattacharya and MacEachern, 2009). These faunas exploit storm-buried nutrients in settings with high sedimentation rates. During fair-weather combined with the degradation of phytodetrital material carried to deep waters, reducing conditions could take place in the low energy prodelta. The diminutive size and sporadic distribution of trace fossils in **F7** are linked to fluctuating oxygen levels in the proximal prodelta.

The highly bioturbated silty-sandstone (**F6**) exhibits bioturbation indices ranging between 3-4 with an increasing upwards trend. Fossil burrows observed within these facies include abundant *Macaronichnus* isp., *Diplocraterion* isp., moderate *Schaubcylindrichnus* isp., and rare *Planolites* isp, *Skolithos* isp, *Rosselia* isp, *Teichichnus* isp. and *Rhizocorallium* isp. burrows. At some levels within **F6** monospecific assemblage of *Macaronichnus* isp (Figs. 2.18A, B, C, D, E). burrows and cryptic- bioturbation were observed. Exceptionally large *Macaronichnus*-like burrows are also referred to herein as “Paramacaronichnus ” (Hoffman, 2008; Dafoe, 2009). *Macaronichnus* isp. and “*Paramacaronichnus* ” show variations in terms of their morphologies. “Paramacaronichnus ” are the burrows of infaunal deposit feeders are easily confused with *Palaeophycus* isp. “Paramacaronichnus ” are typically ~ 1 cm thick and commonly branch or cross-cut each other. Their lack of a mucus lining, and grain segregation features differentiate “*Paramacaronichnus* ” burrows from *Palaeophycus* isp. burrows (Dafoe, 2009). *Macaronichnus* isp. burrows do not display branching geometries and the mineral-focussed grain segregation is higher compared to “Paramacaronichnus” burrows (Hoffman 2008; Dafoe et al., 2008; Dafoe, 2009).

This low diversity / high-intensity trace fossil suite within **F6** includes facies-crossing elements of the *Skolithos* and *Cruziana* ichnofacies. The dominance of deposit feeder structures and facies-crossing trace fossils in a proximal prodelta setting is consistent with a proximal *Cruziana* ichnofacies (MacEachern et al., 2007). The proximal *Cruziana* ichnofacies is dominated by the burrows of deposit-feeding organisms and lacks the burrows of infaunal filter feeders due to elevated turbidity in storm-dominated settings. Elevated water turbidity was likely caused by gravity-induced hyperpycnal flows and/or strong wave agitation which winnowed and kept clay size materials in suspension. The increasing amount of suspended sediment clogs the apertures of filter-feeding fauna (MacEachern and Bann, 2008) so paucity of filter feeding-organism burrows interpreted to indicate elevated turbidity. Recurring storm events elevated the effects of hydraulic energy on the substrate. Near the upper contact of the bioturbated silty-sandstone facies (**F6**) with overlying conglomerate facies (**F1**) *Diplocraterion* isp. burrows are abundant, representing post-storm initial colonization of opportunistic (R- selected) fauna on top of tempestite beds (Vossler and Pemberton, 1988; 1989; Pemberton and MacEachern, 1997). Preserved low-angle planar-laminated beds alternating with bioturbated equivalents in **F6** are

interpreted as lam-scan bedding, which preserves storm events as the laminated/cross-stratified component and post-storm recolonization as the bioturbated components.

Preservation of HCS beds interbedded with highly bioturbated sandstone beds might be the result of several factors, such as: low amounts of erosional amalgamation, low bed penetration by burrowers, the existence of sensitive infauna, and slow rates of recolonization (Pemberton and MacEachern, 1997). Some trace fossils like *Rosselia* isp. and *Schaubcylindrichnus* isp. observed on the East Ridge indicate episodic nearly marine conditions. In contrast, the prodeltaic muddy sandstone facies (**F8**) of South Ridge show no bioturbation, which we attribute to elevated fresh-water input combined with high-frequency storm reworking.

2.6.4 Overall Ichnofacies Distribution

The ichnology of the studied ridges supports a wave-dominated deltaic interpretation. The most critical observation being the presence of impoverished trace-fossil assemblages in comparison with equivalent shoreface successions (MacEachern et al., 2012). The sporadic trace fossil distribution and low-moderate **BI** values likely resulted from a combination of factors associated with river flooding and storm events resulting in elevated sedimentation rates, freshwater input. These events also promoted frequent storm-reworking and disruption of shallow tier burrows, elevated water turbidity and soupy substrates cause impoverishment of trace fossil distribution (Pemberton and MacEachern, 1997; Gingras et al., 2011; Bhattacharya et al., 2020). Rapid and high sedimentation rates on delta front deposits are reflected by the lack of bioturbation in conglomeratic facies (**F1, F2**), whereas within the prodeltaic intervals (**F6-F7**) mobile and sessile deposit feeding structures are common (Bhattacharya and MacEachern, 2009).

River flood and storm induced hyperpycnal flows caused the sporadic distribution and facies-crossing character of the trace fossil suites. Increased depositional rates may have resulted in destruction of domiciles and may have buried nutrients beyond the reach of deep tiering deposit feeders. These conditions commonly result in a decrease of bioturbation intensity in deltaic environments (Bhattacharya and MacEachern, 2009). Wave-dominated deltaic settings, due to delta asymmetry with updrift (west - east) and downdrift (south) sides, show comparatively different ichnological assemblages. Compared with the downdrift side; the updrift side facies exhibit higher **BI** values due to better substrate consistency, fewer salinity variations, and persistent oxygenation conditions resulting from strong wave agitation (MacEachern, 2007).

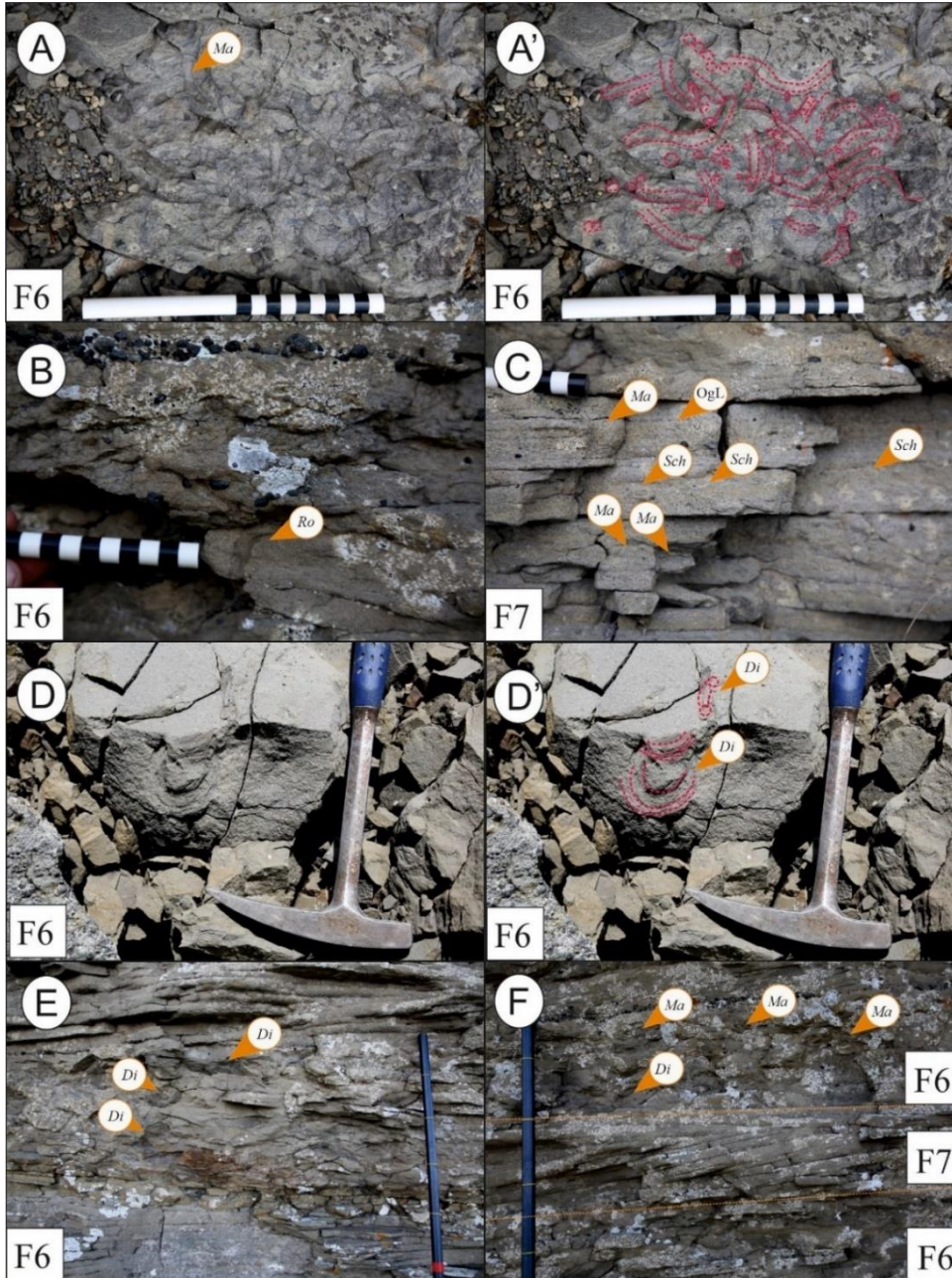


Figure 2.18. Selected trace fossils observed on outcrop. **A)** Bedding plane perpendicular view of selective deposit feeding polychaete burrow *Macaronichnus* isp. (Clifton and Thompson, 1978). (Ma) Burrows showing monospecific assemblage locally. **B)** Truncated vertical cone of clay-silt material filled burrow of *Rosselia* isp. (Ro) in sandy substrate, burrow truncation indicate erosive storm amalgamation. **C)** *Macaronichnus* isp. burrows (Ma) (or *Paramacaronichnus*), organic laminae (OgL), *Schaubcylindrichnus* isp. burrows. **D-E)** *Diplocraterion* isp. (Di) vertical U-shaped

spreiten burrows. *Diplocraterion* isp.; dwelling burrow of a suspension-feeding organism (Fürsich, 1947). F) *Macaronichnus* isp. (Ma) (or *Paramacaronichnus*), and *Diplocraterion* isp. (Di) burrows.

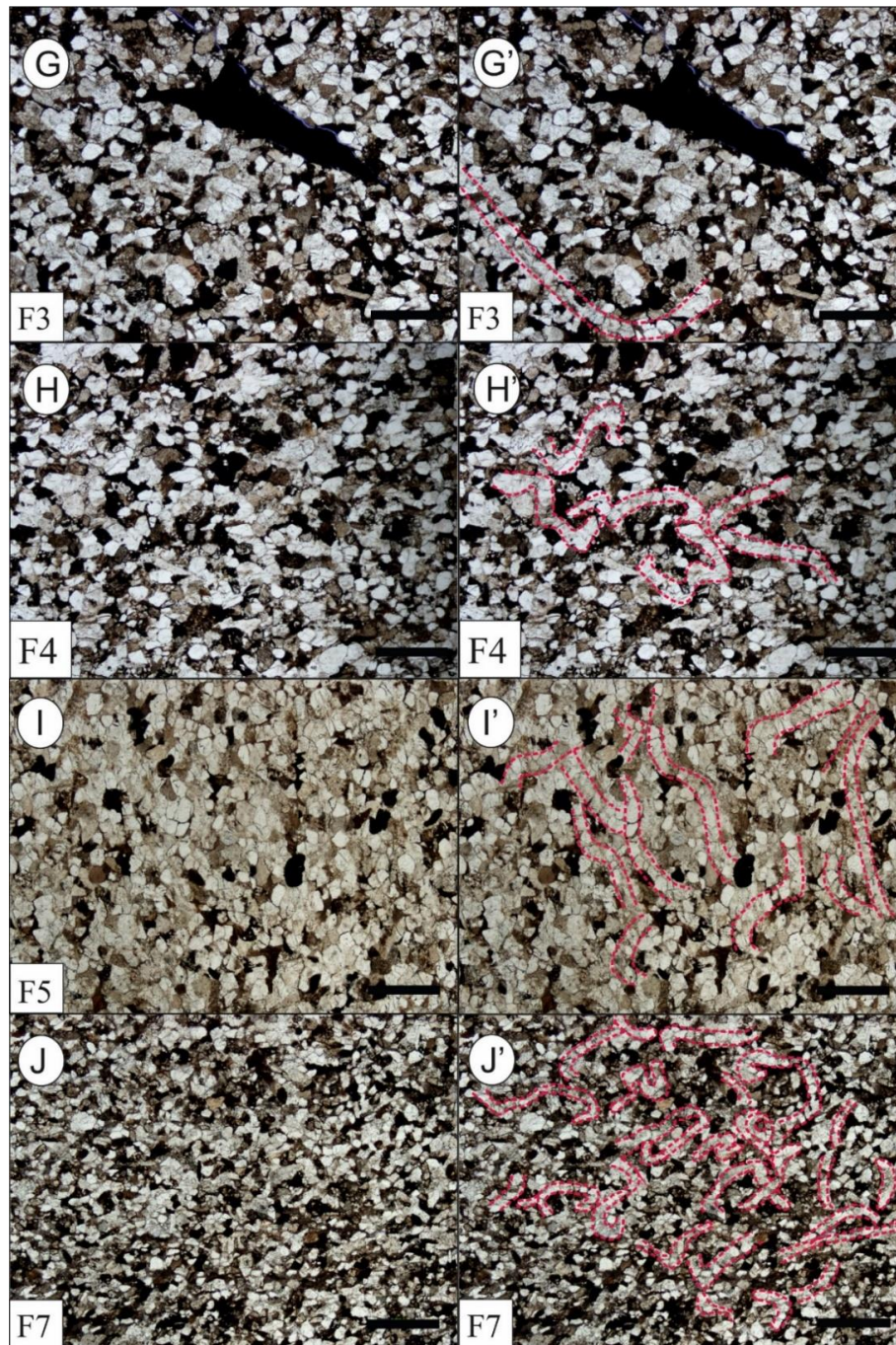


Figure 2.19. Selected photomicrographs and interpretations of facies representing *Cryptic*-bioturbated intervals with less than a mm thick, sinuous, vertical to horizontally aligned and quartz filled (grain selective) burrows. Bar scale is 1.00 mm in length.

2.7 Orientation Interpretations

2.7.1 West Ridge

Tadpole plots indicate a north-northwest directed dip amount varying between 2-8° with a northward (palaeobasinward) increasing trend. In a dip-oriented direction, dip amounts in the north range from 4-8° whereas those in the south are limited to 2-4°, which may indicate a palaeobasinward increasing depositional dip slope or differential structural deformation.

Northwards downlapping clinoforms traced on photomosaics are consistent with master bedding plane palaeodip directions (Fig. 2.11A). Proximal facies, which consist of coarser sediment, have a higher angle of repose, and thus exhibit higher dip angles. In contrast, underlying distal finer-grained facies show more gentle dip angles illustrating the strong progradational aspect of deltaic facies geometries (Olariu et al., 2010). The minor southerly component of the palaeocurrent measurements for the ridges is interpreted to represent the landward migration of longshore bars under fair-weather conditions (Davies et al., 1971; Cook and Gorsline, 1972; Greenwood and Davidson-Arnott, 1976; Clifton, 2003). The thickest abundance of conglomerate facies on this ridge is linked to proximity to a westerly sediment source (Stott, 1968).

2.7.2 East Ridge

Tadpole plots indicate folding along the ridge. Along strike parallel section dip amounts range from 2-10°. Rose plots built from measurements on foreset laminae of conglomerate facies (F1) confirm deposition due to eastwards flowing longshore currents consistently with the West Ridge measurements. Deposition under eastwards flow is also reflected by overall decrease in grain size towards the east. Increased thickness of sandstone facies on East Ridge compared to West Ridge resulted from sediment bypassing from proximal areas and deposited as sandstone lobes in this more northern (basinward) location.

2.7.3 South Ridge

Tadpole plots indicate a northward dip direction, like that observed on the West Ridge. On the other hand, palaeocurrent measurements in sandy facies (F4-F5) indicate westward flow in contrast with West and East ridges. This may be the result of shoaling storm-waves being deflected / reflected in different directions (Greenwood and Mittler, 1985; Davis and Clifton,

1987; Pemberton et al., 2012). This ridge is located on the south-eastern side of the study area and shows the highest level of facies variation compared to other ridges. The sharp increase in the abundance of sandy facies on this ridge is best explained by updrift to downdrift (West-East) facies changes in case of a delta asymmetry. The updrift high energy counterparts (West and East ridges) rich in conglomeratic facies while downdrift side dominantly consist of sandy facies. The wave dominated delta asymmetry further explained in discussion part 2.8.

2.8 Discussion -Wave-dominated delta asymmetry

The heterogeneity of Falher D sedimentary facies within the same parasequence implies a case of wave-dominated delta asymmetry. In deltaic depositional environments, sediments are fluvially sourced and the geometry is controlled by the relative influence of marine and fluvial processes (Fig. 2.20) (Galloway, 1975; Bhattacharya, 2006). Wave-dominated deltas show arcuate-cusate geometry due to strong longshore transport (Coleman and Wright, 1975; Weise, 1980; Bhattacharya and Walker, 1992; Nienhuis et al., 2015). In wave-dominated delta systems under high net longshore transport downdrift deflection of river mouth may occur (Wright, 1977). Also, during heightened river discharge, riverine flow can behave as a barrier (Todd, 1968; Komar, 1973). These wave and fluvial energy variations along the coast result in facies heterogeneity at updrift and downdrift sides of the delta (Bhattacharya and Giosan, 2003). While the coarser material is deposited at updrift side, where the wave reworking rate is higher, relatively fine-grained material is transported to the downdrift side, where fluvial processes much in evidence (Fig. 2.21) (Bhattacharya and Giosan, 2003; Li et al., 2011).

A deltaic interpretation for Falher D lithofacies is linked to a fluvial source of sediments evidenced by the existence of elevated amounts of clay sediment and organic detritus, the presence of fluid mud lenses, sporadically distributed and impoverished ichnofossil suites, and abundant terrestrial fossil fragments (Gingras et al., 1998; MacEachern et al., 2005; Coates and MacEachern, 2007). Palaeocurrent measurements in the study area represent dominant W-E directed longshore flow paralleling the depositional strike. (Coleman and Wright, 1975; Weise, 1980; Bhattacharya and Walker, 1992). Hyperpycnal flow deposition due to episodic storm and flooding events is evidenced by abundant convolute lamination and preservation of organic detritus on all ridges (Myrow et al., 2008). The thick, amalgamated bed-sets of tempestite origin and poorly sorted storm lags confirms subsequent storm wave reworking (Myrow, 1992; 2005).

Evidence of asymmetry interpretation is presented by the strong facies' heterogeneity among the ridges.

The updrift side of the interpreted delta is represented by the West and East ridges, which are characterized by thick conglomerate facies including parallel to subparallel bed-sets, prograding storm ridges, and better sorted sandstone facies confirming strong wave reworking. Also, higher overall **BI** values with higher ichnodiversity, and an absence of fluid mud lenses is linked to less freshwater influence and reduced salinity fluctuations due wave agitation and mixing. The occurrence and abundance of some trace fossils, such as *Schaubcylindrichnus* isp. and *Rosselia* isp. observed in updrift sites, indicates more strongly marine-influenced conditions occurred at the West and East Ridge locations.

In contrast, the downdrift side is represented by the South Ridge section, which is more argillaceous, and fluvial indicators are both conspicuous and abundant. Thick, poorly sorted sandstone intervals on the South Ridge show overall low **BI** values, which are a function of stresses produced by higher fluvial input. The occurrence of organic-rich, fluid-mud deposition on the delta fronts due to high flocculation rates is also consistent with fresh-water influx and riverine-sourced phytodetrital pulses. Overall low bioturbation and sediment sorting, which characterizes sandstone facies on the South Ridge, was also caused by elevated river-sourced clay and freshwater input as physico-chemical stress factors.

The strong longshore currents deflected the delta mouth towards the downdrift side and, concomitantly, fluvial stress conditions such as salinity fluctuations, influx of clay- and silt-sized material, and phytodetrital pulses (which via degradation lowered oxygen conditions) disproportionately affected the downdrift side of the delta, as is evidenced by greatly reduced infaunal diversity and abundance. On the other hand, wave-dominated deposition, showing higher bioturbation intensities due to wave processes inhibiting fluvial stresses occurred on the updrift side (*sensu* MacEachern et al., 2005). In figure 2.22, a model for a Falher D delta is proposed, wherein deflection of the river mouth is caused by longshore transport from west to east. Another plausible explanation of lateral facies variation between ridges could be the "groin" or barrier effect caused by high fluvial discharge (Dominguez, 1996). This groin effect may have created a barrier for sediments moving downdrift. Later when fluvial discharge decreased, intermittent downdrift deflection of river mouth may have occurred.

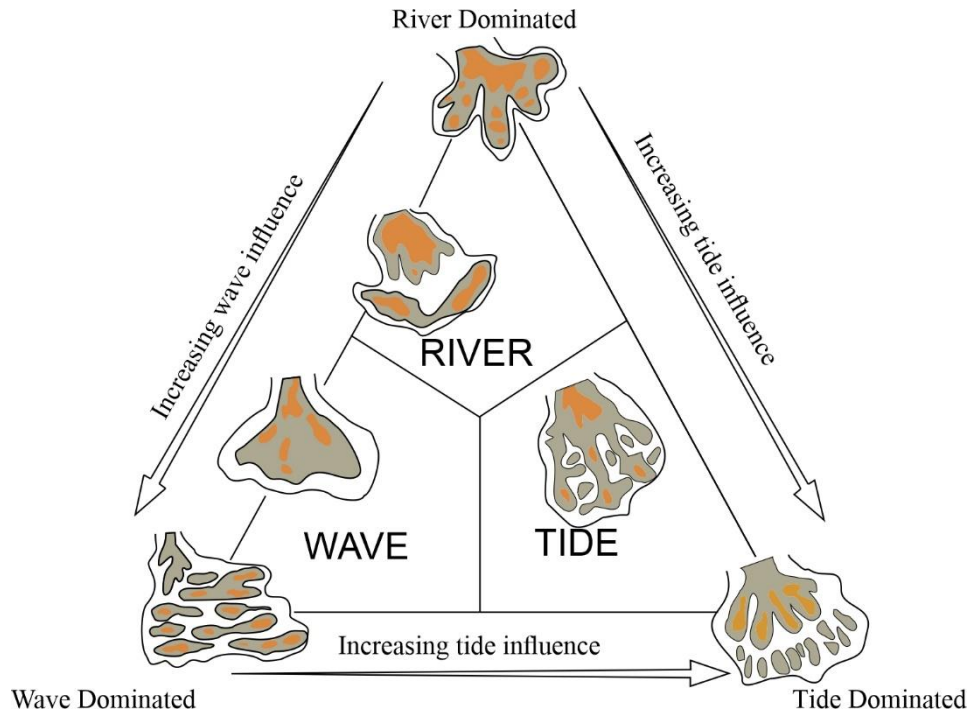


Figure 2.20. Tripartite model showing delta geometries changing related to relative energies of shallow marine processes (Galloway, 1975).

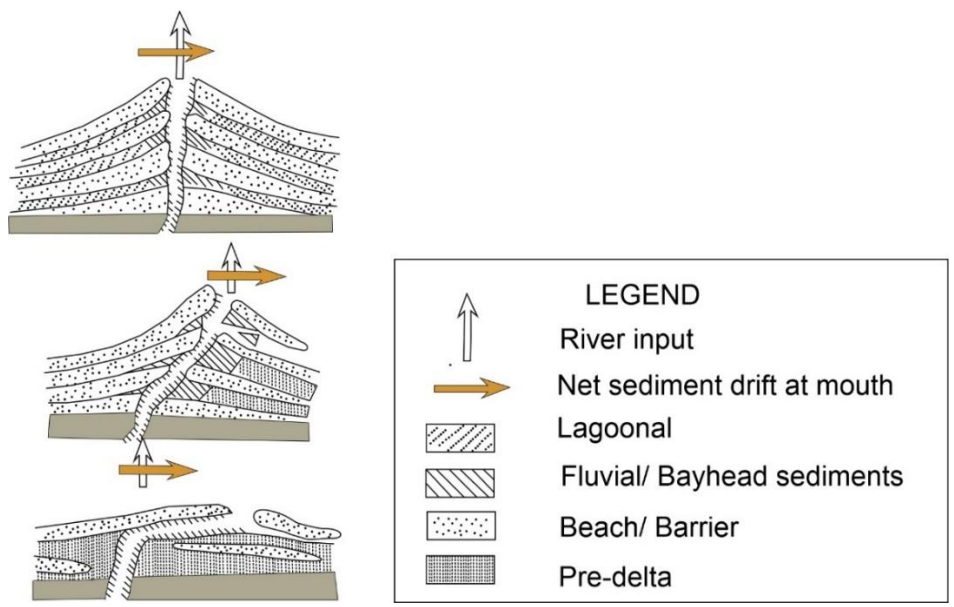


Figure 2.21. Model shows deflection of river mouth from symmetric to asymmetric due to strong longshore transport outpacing groin effect of river (Li et al., 2011).

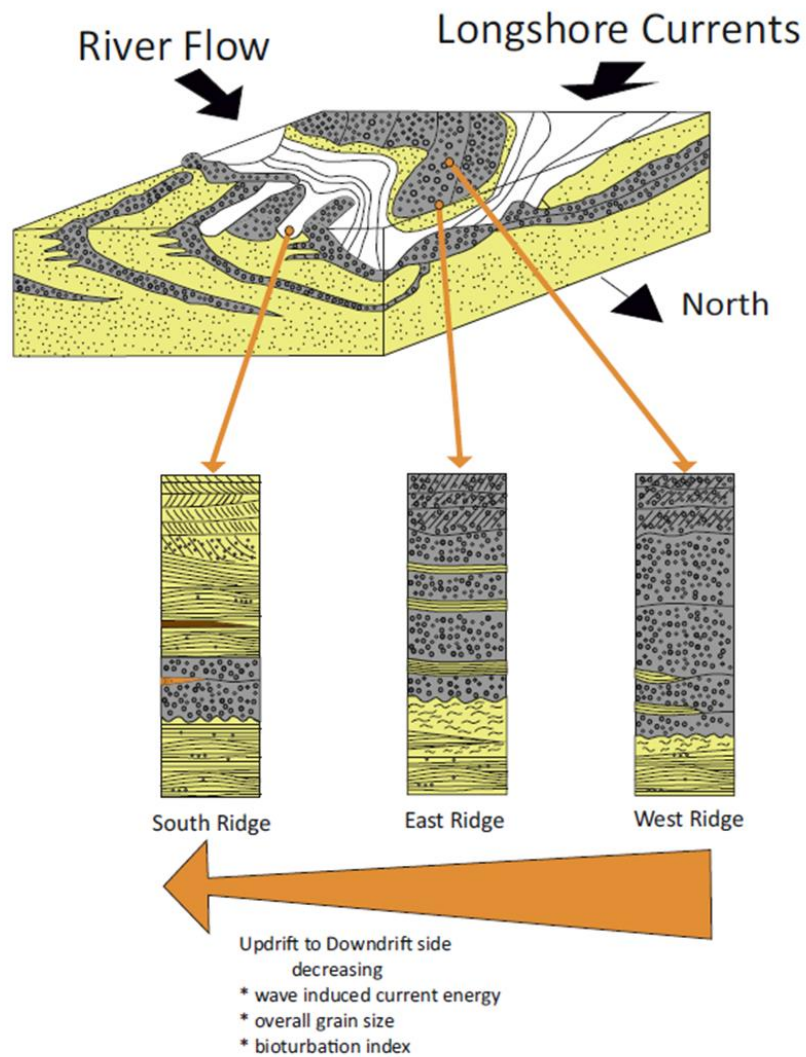


Figure 2.22. Model shows deflection of river mouth from symmetric to asymmetric due to longshore transport. Vertical sections representing hypothetical palaeo-depositional locations of West, East, and South ridges (modified from Bhattacharya et al., 2003) Downdrift deflection of river mouth is caused by longshore currents. Gray facies represent conglomerate and yellow represents sandstone.

2.9 Conclusion

- 1) Detailed facies analysis of the Falher D parasequence indicates deposition in a wave-dominated delta setting strongly affected by longshore currents, storm events and gravity induced hyperpycnal flows. Ten facies were described and grouped into three facies associations (**FA1-3**), representing prodelta to mouth bar deltaic sub-environments. The presence of hummocky and swaley cross stratified sandstone units and abundant pebbly lags on all ridges confirm storm wave reworking. The significant amount of dispersed organic detritus, massive to laminated conglomerate facies with inverse to normal grading are revealing deposition under gravity induced hyperpycnal flows (e.g., Steel et al., 2018).
- 2) The photogrammetry models were used to validate delta morphology interpretations. The delta front facies gently northward dipping consistent with previous studies (Leckie and Walker, 1982) and on West Ridge clinof orm surfaces were observed along dip section. The basinward (northward) and downdrift (eastward) thinning of conglomerate units is attributed to
1) Deposition of conglomerate facies as distal and proximal mouth bars, 2) Transportation and reworking of conglomerate units under eastwards dominant longshore currents.
- 3) The heterogeneity of facies distribution on different ridges indicates an asymmetry. The West and East ridges consist of thick conglomerate and bioturbated silty-sandstone facies representing updrift side of delta. However, South Ridge consist of more argillaceous facies with little or no bioturbation intercalated with fluid mud lenses representing the downdrift side. The proposed depositional model suggests that longshore current and river flow played a critical role in facies distribution. The longshore currents blocked the coarse sediment at river mouth and dispersed finer grained sediments towards downdrift. Also, deflection of river mouth due to strong longshore currents resulted in the abundance of fluvial indicators on downdrift side. The storm wave-dominated deposition surpassing fluvial stress represented by higher bioturbation intensities observed on the updrift side.

The understanding of facies distribution in wave dominated delta settings is important for targeting reservoir units since along strike facies distribution show variations within short distances.

CHAPTER 3 : Storm-Wave Orbital Diameter Calculations from Photogrammetric Datasets

3.1 Introduction

Hummocky cross-stratification is commonly related to storm events (Duke, 1985; Duke et al., 1991; Cheel and Leckie, 1993). It forms under large oscillatory storm-waves acting on shallow marine substrates because of their high preservation potential between fair weather and storm-wave base (Dott and Bourgeois, 1982; Dumas and Arnott, 2006; Morsilli et al., 2012). A thick succession of low-angle planar to sub-parallel laminated beds with convex up and concave up structures observed in very fine-grained sandstone facies is identified at Mount Spieker outcrops as hummocky cross-stratification. The lamina-sets present low angle-internal and basal truncation surfaces. Also, pebbly storm lags were locally observed at bedding contacts on West, East, and South ridges (Mount Spieker, British Columbia). Abundant HCS and SCS bed-sets with pebble lags confirm that recurring storm events took place during deposition of the study interval.

HCS wavelengths vary from 10-20 cm to several meters depending on environmental factors (Harms et al., 1975; Dott and Bourgeois 1982; Yang and Dalrymple, 2006). One of the factors controlling the variability in wavelength is wave orbital diameter (d_o) forming the hummock and swales (Harms et al., 1975; Yang and Dalrymple et al., 2006). Wave orbital diameter increases up to the breaker zone and decreases above this zone due to frictional wave dissipation (Yang and Dalrymple et al., 2006) (Fig. 3.7). Thus, HCS wavelength measurements can be used to make depth interpretations in shallow marine settings between storm-wave base and the breaker zone. This study aims to show the wavelength and amplitude variation along a progradational stratigraphic succession.

3.2 Study Area and Methods

This study focuses on HCS bed sets of the Lower Cretaceous Falher D Member equivalent outcrop successions located at Mount Spieker, northeastern British Columbia (Fig. 3.1). Measurements were performed on three different outcrop sections within the same Falher D parasequence. Outcrop sections are referred as West, East and South Ridges and are shown on map (Fig. 3.2) (Table 3.1). Three-dimensional outcrop models were built using Agisoft Metashape software using algorithms of structure from motion (SfM) photogrammetry linked

with multi-view stereo MVS method. Image data were gathered via DJI Mavic Pro-2 drone type UAV with a Hasselblad 20MP camera. Collected drone data consists of a series of images with at least 60% sidelap and vertically- overlapping georeferenced images taken approximately 5 to 10 meters from the outcrop. Large scale sedimentary structures, such as HCS, are clearly observable on photomosaics and convenient for measurements. The wavelength measurements were carried out on 3D orthogrammetry models. HCS laminae sets were traced, and deflection points were indicated on photomosaic outputs. The grain size of the HCS facies were recorded in the field and on hand samples in the laboratory using a petrographic microscope.

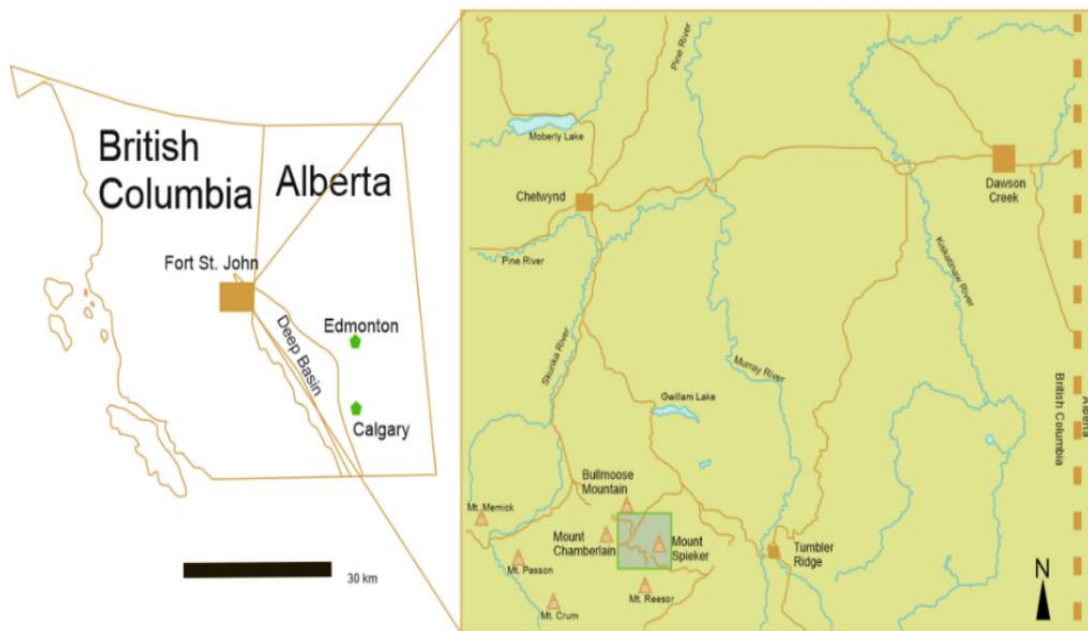


Figure 3.1. Location map showing the Deep Basin and the location of the outcrop study area at Mount Spieker (Caddel et al., 2004). Note that excellent exposure of Falher C, D and F equivalent stratigraphic successions occurs are Mounts Spieker, Bullmoose and Chamberlain (Leckie and Walker, 1982; Leckie 1985b; Moslow and Schink, 1995; Moslow, 1998; Caddel, 2000; Caddel and Moslow, 2004; Zonneveld and Moslow, 2004).

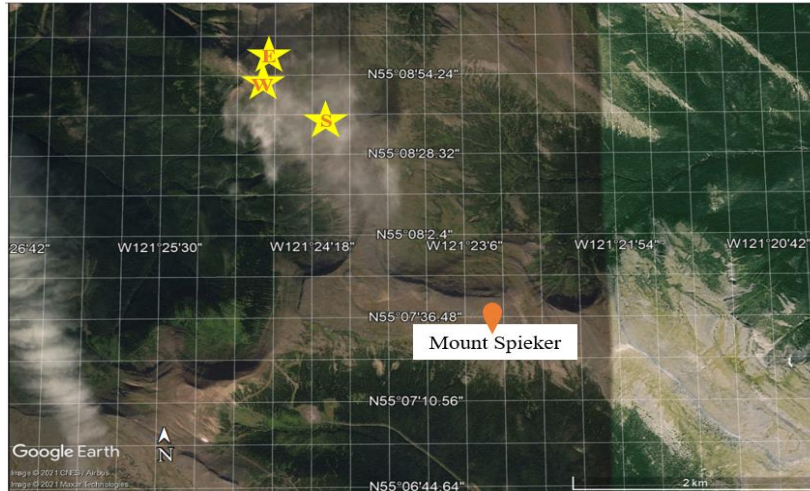


Figure 3.2. Google Earth satellite image of study area; measurement locations are labelled with yellow stars (W: West Ridge, E: East Ridge, S: South Ridge).

Table 3.1. Study locations GPS Coordinates

Ridge	GPS Coordinate
West Ridge	N55° 08' 53.0" W121° 24' 41.2"
East Ridge	N55° 08' 58.3" W121° 24' 38.0"
South Ridge	N55° 08' 36.4" W121° 24' 09.0"

3.3 Results and Interpretation

The wavelength and amplitude measurements on photomosaics were performed on 2nd and 3rd order HCS laminae surfaces (Fig. 3.3) for the silty-sandstone (F6-F7) and muddy sandstone facies (F8) which were previously described as lithofacies representing a prodeltaic setting (Chapter 2). The dominant grain size is very fine sand (0.0625-0.125 mm on the Wentworth-Udden). On the West Ridge, sandy facies thicknesses are comparably thin and limited in their exposure, so only 2 measurements were performed. Measurements range from 4 to 6 cm in amplitude, and 1.2 to 2.8 meters in wavelength (Fig. 3.4). On the East Ridge wavelengths range between 1.3 and 2.8 meters and wave amplitude are between 1 cm to 6 cm again with a decreasing upwards trend (Fig. 3.5). The South Ridge has 2 facies that exhibit HCS: muddy

sandstone (F8); and low-angle parallel laminated sandstone beds (F7) with amplitudes that vary between 6 to 8 cm and wavelength measurements that vary from 1.4 to 1.9 meters (Fig. 3.6). Amplitudes exhibit a decreasing-upwards trend whereas wavelengths exhibit an increasing-upwards trend within all successions studied (Table 3.2, Table 3.3, and Table 3.4). The interpreted depositional wave-orbitals are thereby expressed as “Estimated $\lambda = 0.75d_0$ ” in tables 3.2, 3.3 and 3.4, below) (Dalrymple, 2006).

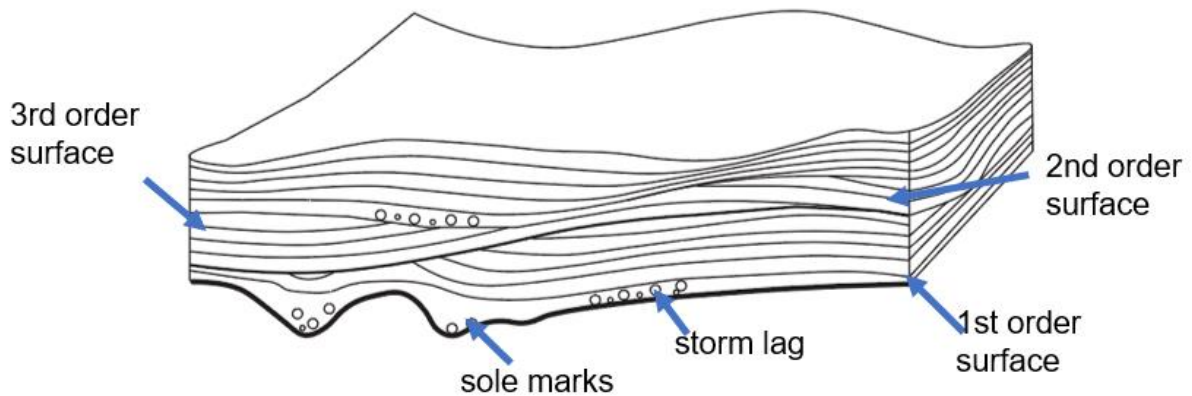


Figure 3.3. HCS illustration showing order of surfaces (modified from Harms et al., 1975).

Table 3.2. *West Ridge– Hummocky cross-stratification wavelength and amplitude measurements in low-angle planar-laminated silty-sandstone facies (F7) and highly bioturbated silty-sandstone (F6).*

M#	Facies #	Elevation from section base (m)	HCS amplitude (cm)	HCS $\frac{1}{2}$ wavelength $\frac{1}{2}\lambda$ (cm)	Estimated $d_0=\lambda/0.75$
M1	F7	0.90	6.00	60	160
M2	F6	3.20	4.00	140	373



Figure 3.4. Figure shows the measurements performed on West Ridge facies F7 and F6 (M1: Measurement 1, M2: Measurement 2).

Table 3.3. *East Ridge – Hummocky cross-stratification wavelength and amplitude measurements in low-angle planar-laminated silty-sandstone facies (F7) and highly bioturbated silty-sandstone (F6).*

M#	Facies #	Elevation from section base(m)	HCS amplitude (cm)	HCS $\frac{1}{2}$ wavelength $1/2\lambda$ (cm)	Estimated $d_0=\lambda/0.75$
M1	F7	1.2	6	65	173
M2	F6	1.8	5	115	306
M3	F6	2.4	1	140	373

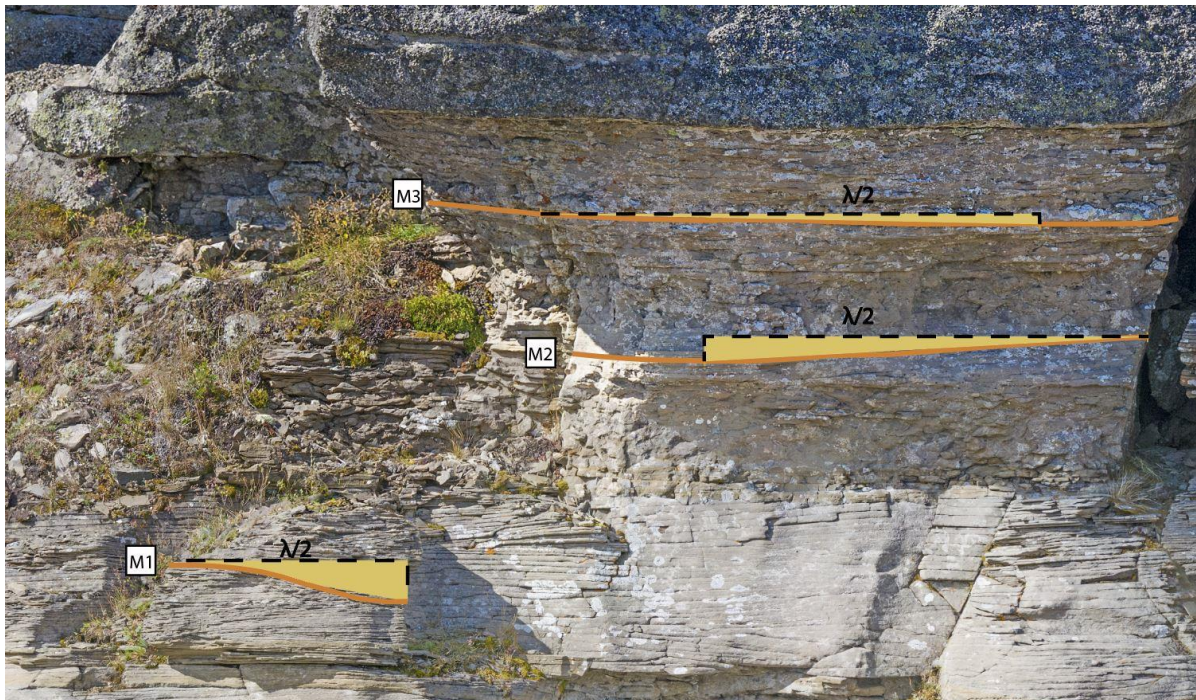


Figure 3.5. Figure shows the measurements performed on East Ridge facies F7 and F6 (M1: Measurement 1, M2: Measurement 2, M3: Measurement 3).

Table 3.4. *South Ridge – Hummocky cross-stratification wavelength and amplitude measurements in low-angle planar-laminated silty-sandstone facies (F7) and muddy sandstone facies (F8).*

M#	Facies #	Elevation from section base(m)	HCS amplitude (cm)	HCS $\frac{1}{2}$ wavelength $\frac{1}{2}\lambda$ (cm)	Estimated $d_0=\lambda/0.75$
M1	F8	0.9	8	70	187
M2	F7	3.3	7	85	226
M3	F7	3.6	6	95	253

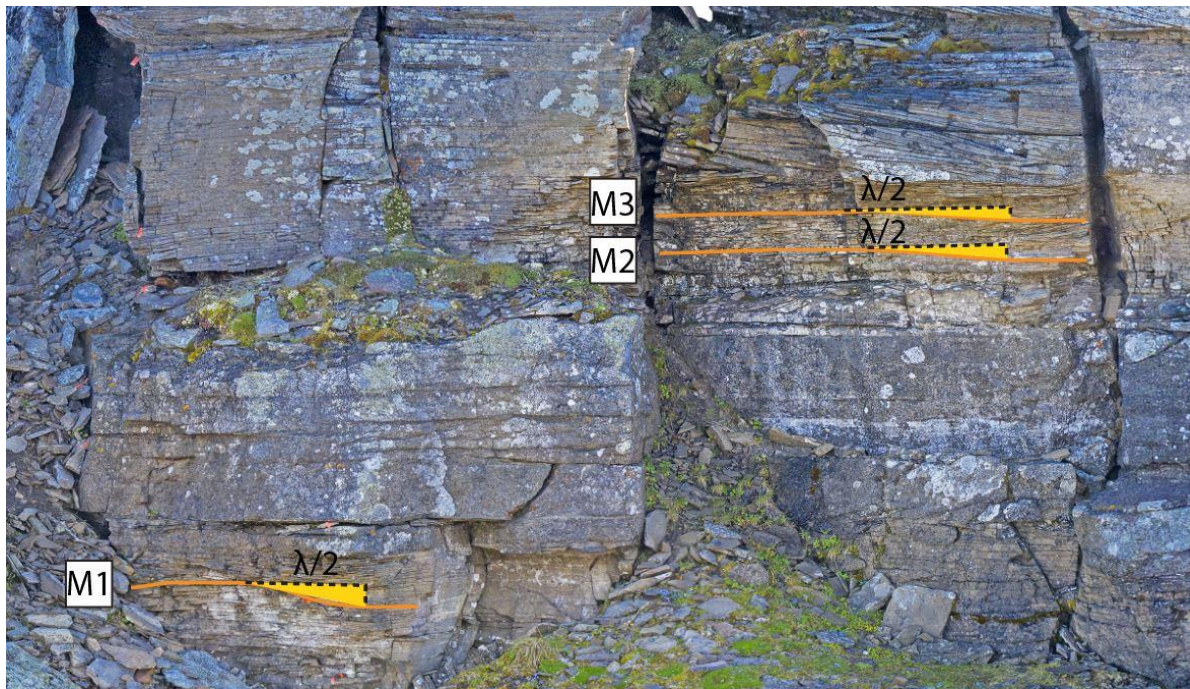


Figure 3.6. Figure shows the measurements performed on South Ridge facies **F8** and **F7** (M1: Measurement 1, M2: Measurement 2, M3: Measurement 3).

3.4 Discussion

As a general trend, results are consistent with upwards increasing wave orbital diameters indicating decreasing water depth and suggesting progradation of each ridge (Figs. 3.7, 3.8). The variation of average orbital diameters observed between different ridges may have resulted from variations in storm event intensity, changes in prevailing wind direction during the storms and/or varying fluvial discharge rates combined with fluctuations in flow conditions. Also, measurements were done by assuming the preserved hummocky cross stratification was symmetrical following deposition.

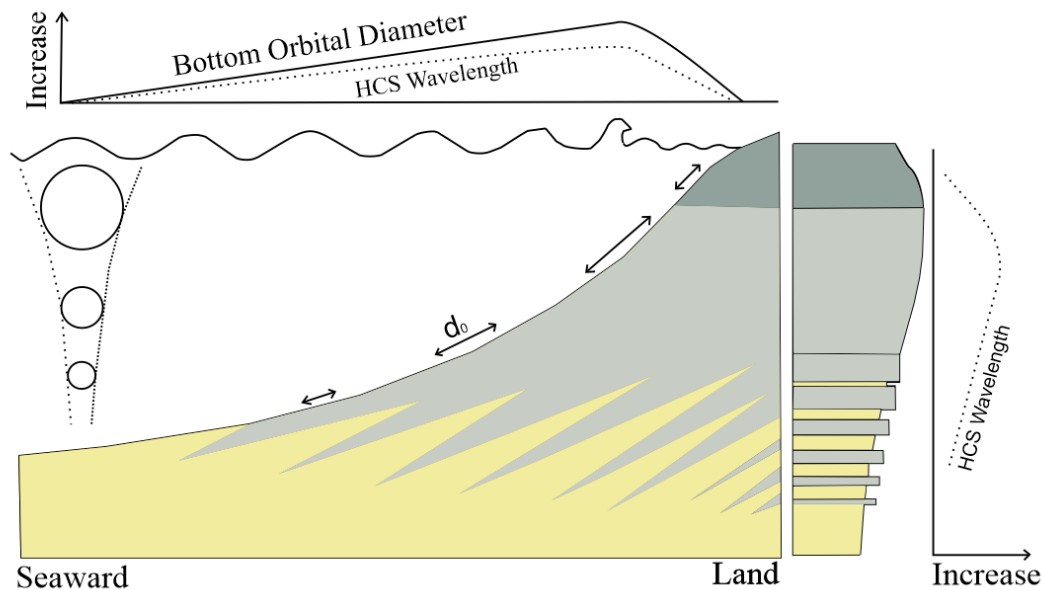


Figure 3.7. Diagram shows wave orbital diameter vs. HCS wavelength change (Yang and Dalrymple et al., 2006).

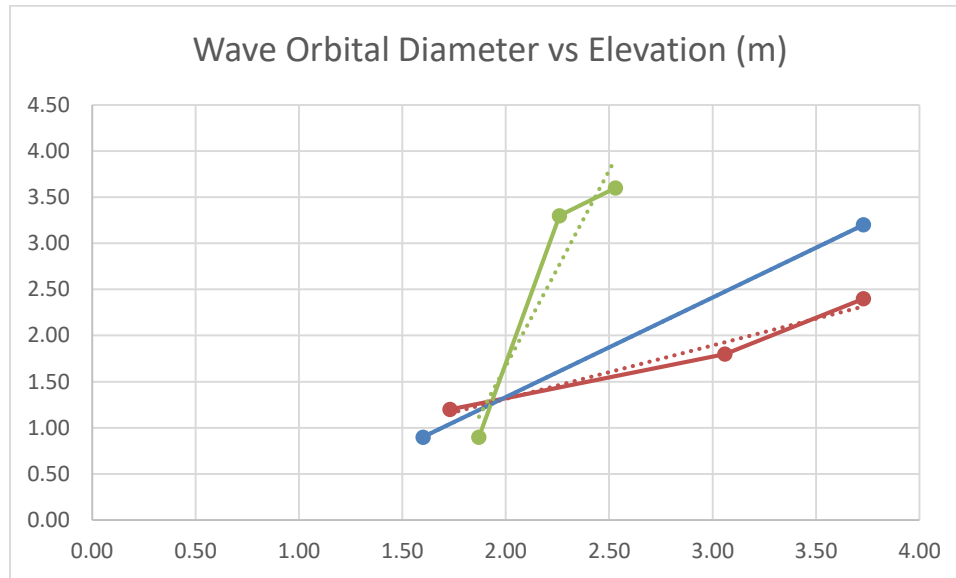


Figure 3.8. Graph showing wave orbital diameter values (x-axis) plotted against elevation (y-axis) values. Measurement elevations increase corresponds to shallowing in depth. The shallower depths represent higher wave orbital diameter values. Red line: East Ridge measurements, Blue line: West Ridge measurements, Green line: South Ridge measurements.

3.5 Conclusion

In conclusion several measurements were collected from different outcrops representing Falher D delta. The wavelength and amplitude measurements on photomosaics were performed on 2nd and 3rd order HCS laminae surfaces (Fig. 3.3) for the silty-sandstone (F6, F7) and muddy sandstone facies (F8) which are previously described as facies representing prodelta setting (see Chapter 2).

Measurements indicate increase in wave orbital diameter with increasing measurement elevation. This observation is consistent with the previous studies showing wave orbital diameter distribution with shallowing depths as HCS wavelength increase from lower shoreface till the breaker zone (e.g., Yang and Dalrymple et al., 2006). The variations in HCS wavelength can potentially be used to determine relative depth in palaeoenvironments.

Observation of different average orbital diameters among different ridges may have resulted from variations in storm event intensity, changes in prevailing wind direction during the storms and/or varying fluvial discharge rates combined with fluctuations in flow conditions.

CHAPTER 4: Conclusion

Outcrops of the Lower Cretaceous Falher D Member are investigated in terms of their sedimentology and ichnology. Ten individual lithofacies are grouped into three facies associations as distributary mouth (**FA1**), delta front (**FA2**) and prodelta (**FA3**). The deltaic interpretation is based on impoverished and sporadically distributed trace fossils, abundant continentally derived organic material, and argillaceous material. The abundance of tempestite beds among all outcrops indicate strong storm-wave reworking. The scoured bottom contacts and inverse to normal graded structure of conglomerate units representing deposition under gravity induced hyperpycnal flows which are possibly formed due to storm related river flooding events.

The facies distribution shows strong heterogeneity. The downdrift represents robust fluvial input with the occurrence of fluid muds and argillaceous facies whereas the updrift side consists of thick conglomerate facies interbedded with sandstone lenses. The heterogeneity in facies distribution is linked to the regional longshore drift orientation. In wave-dominated deltas strong net longshore drift causes morphological and facies asymmetry in updrift and downdrift sides of the delta (e.g., Li et al., 2011). Trace fossil distributions were also used as an important proxy for differentiation of updrift and downdrift deltaic deposition. Bioturbation values are overall higher on the updrift side due to lowering of stresses caused by fluvial input.

3D orthogrammetry models were also used to visualize the facies distribution between the updrift and downdrift sides of the deltaic succession. All the facies were traced on the outcrop models and their continuity is documented herein. Palaeocurrent and orientation measurements were performed on foreset laminae and master bedding surfaces. The presence of strong longshore currents was documented by palaeocurrent measurements performed on 3D photomosaics. The dip and strike measurements on West Ridge indicates northward dipping palaeobasin and presence of westerly shore – parallel longshore currents. Photomosaics have also allowed us to measure wavelengths of hummocky cross stratified sandstone facies. The upwards increasing wave orbital diameters representing progradation within same facies.

BIBLIOGRAPHY

Adani, N. 2019. Sedimentology, Ichnology, Sequence Stratigraphy, and Petrography of the Falher F Unit, Wapiti Area, Northwestern Alberta. Unpublished M.Sc. thesis, University of Alberta, Edmonton, 267 p.

AEUB. 1999. Alberta's Reserves. (1998). Alberta Energy and Utilities Board Reserve Report, Statistical Series 18, p. 4-1 to 4-207.

Aigner, D.K. 1985. Storm depositional systems: Dynamic stratigraphy in modern and ancient shallow-marine sequences. Lecture Notes in Earth Science, v. 3, p. 174.

Akinlotan, O. 2019. Sideritic ironstones as indicators of depositional environments in the Weald Basin (Early Cretaceous) SE England. Geological Magazine, v. 156, p. 533-546.

Alberta Study Group, 1954. Lower Cretaceous of the Peace River Region. In: Western Canada Sedimentary Basin: A Symposium. L.M. Clark (Eds.). American Association of Petroleum Geologists, Rutherford Memorial Volume, p. 268–278.

Allison, M.A., Kineke, G.C., Gordon, E.S. and Goni, M.A. 2000. Development and reworking of a seasonal flood deposit on the inner continental shelf off the Atchafalaya River. Continental Shelf Research, v. 20, p. 2267-2294.

Alpert S.P. 1974. Systematic review of the genus *Skolithos*. Journal of Paleontology, v. 48, p. 661–669.

Armitage, I.A., Pemberton, S.G. and Moslow, T.F. 2004. Facies succession, stratigraphic occurrence, and paleogeographic context of conglomeratic shorelines within the Falher “C”, Spirit River Formation, Deep Basin, west-central Alberta. Bulletin of Canadian Petroleum Geology, v. 52, p. 39-56.

Arnott, R.W.C. 1993. Sedimentological and sequence stratigraphic model of the Falher “D” Pool, Lower Cretaceous, northwestern Alberta. Bulletin of Canadian Petroleum Geology, v. 41, p. 453-463.

Badgley, P.C. 1952. Notes on the subsurface stratigraphy and oil and gas geology of the Lower Cretaceous series in central Alberta. Geological Survey of Canada, Paper 52-11, p. 23.

Bann, K.L., Tye, S.C., MacEachern, J.A., Fielding, C.R. and Jones, B.G. 2008. Ichnological and sedimentologic signatures of mixed wave-and storm-dominated deltaic deposits: Examples from the Early Permian Sydney Basin, Australia. In: Hampson G. J., Steel, R. J., Burgess, P. M., and Dalrymple, R. W., eds., Recent Advances in Models of Siliciclastic Shallow-Marine Stratigraphy. SEPM Society for Sedimentary Geology, v. 90, p. 0.

Bates, C. C. 1953. Rational theory of delta formation. AAPG Bulletin, v. 37, p. 2119-2162.

Bhattacharya, J. P., and Giosan, L. 2003. Wave-influenced deltas: Geomorphological implications for facies reconstruction. *Sedimentology*, v. 50, p. 187-210.

Bhattacharya, J. P., and MacEachern, J. A. 2009. Hyperpycnal rivers and prodeltaic shelves in the Cretaceous seaway of North America. *Journal of Sedimentary Research*, v. 79, p. 184-209.

Bhattacharya, J.P., and Walker, R.G., 1992, Deltas. In: Walker, R.G., and James, N.P. (Eds.). *Facies Models. Response to Sea Level Change*. Geological Association of Canada, p. 157-177.

Bhattacharya, J. P., Howell, C. D., MacEachern, J. A., and Walsh, J. P. 2020. Bioturbation, sedimentation rates, and preservation of flood events in deltas. *Palaeogeography, Palaeoclimatology, Palaeoecology*, v. 560, p. 110049.

Bilmes, A., D'Elia, L., Lopez, L., Richiano, S., Varela, A., Alvarez, M. del P., Bucher, J., Eymard, I., Muravchik, M., Franzese, J., and Ariztegui, D. 2019. Digital outcrop modelling using “structure-from-motion” photogrammetry: Acquisition strategies, validation, and interpretations to different sedimentary environments. *Journal of South American Earth Sciences*, v. 96, p. 102325.

Buatois, L. A., Santiago, N., Parra, K., and Steel, R. 2008. Animal-substrate interactions in an early Miocene wave-dominated tropical delta: Delineating environmental stresses and depositional dynamics (Tacata field, Eastern Venezuela). *Journal of Sedimentary Research*, v.78, p. 458-479.

Buatois, L. A., Saccavino, L. L., and Zavala, C. 2011. Ichnologic signatures of hyperpycnal flow deposits in Cretaceous river-dominated deltas, Austral Basin, southern Argentina. In: R. M. Slatt and C. Zavala. (Eds.). *Sediment transfer from shelf to deep water- Revisiting the delivery system*. AAPG, *Studies in Geology*, v. 61, p. 153-170.

Butman, C. A. 1987. Larval settlement of soft-sediment invertebrates: the spatial scales of pattern explained by active habitat selection and the emerging role of hydrodynamical processes. *Oceanography Marine Biology*, v. 25, p. 113-165.

Bromley, R. G., Milan, J., Uchman, A., and Hansen, K. S. 2009. Rheotactic *Macaronichnus*, and human and cattle trackways in Holocene beachrock, Greece: reconstruction of paleoshoreline orientation. *Ichnos*, v. 16, p. 103-117.

Caddel, E. M. 1999. Sedimentology and stratigraphy of the Falher C Member, Spirit River Formation, northeastern British Columbia. M.Sc. Thesis, University of Calgary, Alberta, Canada, 242 p.

Caddel, E. M., and Moslow, T. F. 2004. Outcrop sedimentology and stratal architecture of the Lower Albian Falher C sub-member, Spirit River Formation, Bullmoose mountain, northeastern British Columbia. *Bulletin of Canadian Petroleum Geology*, v. 52, p. 4-22.

Cant, D. J. 1983. Spirit River Formation - a stratigraphic- diagenetic gas trap in the Deep Basin of Alberta. *American Association of Petroleum Geologists Bulletin*, v. 67, p. 577-587.

Cant, D.J. 1988. Regional structure and development of the Peace River Arch, Alberta: a Paleozoic failed-rift system? *Bulletin of Canadian Petroleum Geology*, v. 36, p. 284-295.

Cant, D. J., & Ethier, V. G. 1984. Lithology-Dependent Diagenetic Control of Reservoir Properties of Conglomerates, Falher Member, Elmworth Field, Alberta. *American Association of Petroleum Geologists Bulletin*, v. 68, p. 1044-1054.

Casas, J. E., and Walker, R. G. 1997. Sedimentology and depositional history of Units C and D of the Falher Member, Spirit River Formation, west-central Alberta. *Bulletin of Canadian Petroleum Geology*, v. 45, p. 218-238.

Cheel, R. J., and Leckie, D. A. 1993. Hummocky cross-stratification. *Sedimentology review*, v. 1, p. 103-122.

Clifton, H. E. 2003. Supply, segregation, successions, and significance of shallow marine conglomeratic deposits. *Bulletin of Canadian Petroleum Geology*, v. 51, p. 370-388.

Clifton, H. E., and Thompson, J. K. 1978. Macaronichnus segregatis; a feeding structure of shallow marine polychaetes. *Journal of Sedimentary Research*, v. 48, p. 1293-1302.

Coates, L., MacEachern, J.A. 2007. The ichnological signatures of river- and wave-dominated delta complexes: Differentiating deltaic and non-deltaic shallow marine successions, Lower Cretaceous Viking Formation and Upper Cretaceous Dunvegan Formation, west-central Alberta. In: MacEachern, J.A., Bann, K.L., Gingras, M.K., Pemberton, S.G. (Eds.). *Applied Ichnology. SEPM, Short Course Notes*, v. 52, p. 227-254.

Coleman, J.M., and Wright, L.D. 1975. Modern River deltas: variability of processes and sand bodies. In: Broussard, M.L. (Eds.). *Deltas, Models for Exploration*. Houston Geological Society, p. 99-149.

Cook, D.O., and Gorsline, D.S. 1972. Field observations of sand transport by shoaling waves. *Marine Geology*, v. 13, p. 31-55.

Davis, R.A., and Clifton, H.E. 1987. Sea-level change and the preservation potential of wave-dominated and tide-dominated coastal sequences. In: Nummedal, D., Pilkey, O.H., and Howard, J.D. (Eds.). *Sea-level Fluctuations and Coastal Evolution*. SEPM, Special Publication 41, p. 167-178.

Dafoe, L.T. 2009. Building upon ichnological principles: modern biogenic structures, ichnotaxonomic classification, and paleoecological and stratigraphic significance of ichnofossil assemblages. M.Sc. Thesis, University of Alberta, Canada, Edmonton, 371 p.

Dafoe, L.T., Gingras M.K., Pemberton, S.G. 2008. Analysis of mineral segregation in *Euzonus mucronata* burrow structures: one possible method in the construction of ancient *Macaronichnus segregatis*. *Ichnos*, v. 15, p. 91-102.

Dafoe, L. T., Gingras, M. K., and Pemberton, S. G. 2010. Wave-influenced deltaic sandstone bodies and offshore deposits in the Viking Formation, Hamilton Lake area, south-central Alberta, Canada. *Bulletin of Canadian Petroleum Geology*, v. 58, p. 173-201.

Dahmer, G. 1937. Lebensspuren aus dem Taunusquarzit und den Siener Schichten: Preussischen Geologischen Landesanstalt zu Berlin, *Jahrbuch*, v. 57, p. 523-539.

Dashtgard, S. E., Gingras, M. K., and Pemberton, S. G. 2008. Grain-size controls on the occurrence of bioturbation. *Palaeogeography, Palaeoclimatology, Palaeoecology*, v. 257, p. 224-243.

DeMille, G. 1958. Pre-Mississippian history of the Peace River Arch. *Journal of the Alberta Society of Petroleum Geologists*, v. 6, p. 61-68.

Dott, R. H. 1983. Episodic Sedimentation. *Journal of Sedimentary Petrology*, v. 53, p. 5-23.

Dott, R. H., and Bourgeois, J. 1982. Hummocky stratification: significance of its variable bedding sequences. *Geological Society of America Bulletin*, v. 93, p. 663-680.

Duke, W.L., 1985, Hummocky cross-stratification, tropical hurricanes, and intense winter storms: *Sedimentology*, v. 32, p. 167–194.

Duke, W.L., Arnott, R.W.C. and Cheel, R.J. 1991. Shelf sandstones and hummocky cross-stratification: new insights on a stormy debate. *Geology*, v. 19, p. 625–628.

Dumas, S., Arnott, R. W. C., & Southard, J. B. 2005. Experiments on oscillatory-flow and combined-flow bed forms: Implications for interpreting parts of the shallow-marine sedimentary record. *Journal of Sedimentary Research*, v. 75, p. 501–513.

Einsele, G., and Seilacher, A. 1982. Paleogeographic significance of tempestites and periodites. In: *Cyclic and event stratification*. Springer, Berlin, Heidelberg, p. 531-536.

Einsele, G., Ricken, W. and Seilacher, A. 1991. Cycles and events in stratigraphy-basic concepts and terms. In: Einsele G., Ricken, W. and Seilacher, A. (Eds.). *Cycles and Events in Stratigraphy*. Springer, Berlin, p. 1- 19

Fernández, O. 2005. Obtaining a best fitting plane through 3D georeferenced data. *Journal of Structural Geology*, v. 27, p. 855–858.

Frey, R.W., and Howard, J.D. 1981. *Conichnus* and *Schaubcylindrichnus*: redefined trace fossils from the Upper Cretaceous of the Western Interior. *Journal of Paleontology*, v. 55, p. 800-804.

Frey, R.W., and Howard, J.D. 1985. Trace fossils from the Panther Member, Star Point Formation (Upper Cretaceous), Coal Creek Canyon, Utah. *Journal of Paleontology*, v. 59, p. 370-404.

Frey, R. W., and Pemberton, S. G. 1991. The ichnogenus *Schaubcylindrichnus*: morphological, temporal, and environmental significance. *Geological Magazine*, v. 128, p. 595-602.

Freidman, G.M. 1961. Distinction between dune, beach, and river sands from their textural characteristics. *Journal of Sedimentary Petrology*, v. 31, p. 514-529.

Freidman, G.M. 1967. Dynamic processes and statistical parameters compared for size frequency distribution of beach and river sands. *Journal of Sedimentary Petrology*, v. 37, p. 327-354.

Fürsich, F. T. 1974b. On Diplocraterion Torell 1870 and the significance of morphological features in vertical, spreiten-bearing, U-shaped trace fossils. *Journal of Paleontology*, v. 48, p. 952-962.

Galloway, W.E. 1975. Process framework for describing the morphologic and stratigraphic evolution of deltaic depositional systems. In: Broussard, M.L. (Eds.). *Deltas: models for exploration*, p. 87-98.

Gani, M.R., Bhattacharya, J.P., and MacEachern, J.A. 2004. Using ichnology to determine relative influence of waves, storms, tides and rivers in deltaic deposits: examples from Cretaceous delta complexes in the Western Interior Seaway, Wyoming–Utah, USA. In: American Association of Petroleum Geologists, Annual Convention, Dallas, Texas, (abstract), p. A49.

Gingras, M.K., MacEachern, J.A., and Pemberton, S.G. 1998. A comparative analysis of the ichnology of wave- and river-dominated allomembers of the Upper Cretaceous Dunvegan Formation. *Bulletin of Canadian Petroleum Geology*, v. 46, p. 51–73.

Gingras, M.K., MacMillan, B., Balcom, B.J., Saunders, T., and Pemberton, S.G. 2002. Using magnetic resonance imaging and petrographic techniques to understand the textural attributes and porosity distribution in *Macaronichnus*-burrowed sandstone. *Journal of Sedimentary Research*, v. 72, p. 552-558.

Gingras, M.K., MacEachern, J.A., and Dashtgard, S.E. 2011. Process ichnology and the elucidation of physico-chemical stress. *Sedimentary Geology*, v. 237, p. 115-134.

Gingras, M.K., MacEachern, J.A., Dashtgard, S.E. et al. 2012a. Estuaries. In: Knaust D, Bromley R.G. (Eds.). *Trace fossils as indicators of sedimentary environments. Developments in Sedimentology*, v. 64, p. 463-505.

Greene, T.J., Gingras, M.K., Gordon, G.S., and McKeel, D.R. 2012. The significance of deep-water cryptic bioturbation in slope-channel massive sand deposits of the lower Rio Dell Formation, Eel River basin, California. *Marine and Petroleum Geology*, v. 29, p. 152-174.

Greenwood, B., and Davidson-Arnott, R.G. 1979. Sedimentation and equilibrium in wave-formed bars: a review and case study. *Canadian Journal of Earth Sciences*, v. 16, p. 312-332.

Greenwood, B., and Mittler, P.R. 1985. Vertical sequence and lateral transitions in the facies of a barred nearshore environment. *Journal of Sedimentary Research*, v. 55, p. 366-375.

Haldeman, S. S. 1840. Supplement to number one of "A monograph of the Limniades, and other freshwater univalve shells of North America," containing descriptions of apparently new animals in different classes, and the names and characters of the subgenera in *Paludina* and *Anculosa*. J. Dobson, Philadelphia, p. 3.

Hamblin, A.P. and Walker, R.G. 1979. Storm-dominated shallow marine deposits: the Fernie-Kootenay (Jurassic) transition, southern Rocky Mountains. *Canadian Journal of Earth Sciences*, v. 16, p. 1673-1690.

Harms, J.C., Southard, J.B., Spearing, D.R., and Walker, R.G. 1975. Depositional environments as interpreted from primary sedimentary structures and stratification sequences, Dallas. *SEPM, Short Course 2*, v. 2, p. 161.

Hayes, D.A., Timmer, E.R., Deutsch, J.L., Ranger, M.J., and Gingras, M.K. 2017. Analyzing dune foreset cyclicity in outcrop with photogrammetry. *Journal of Sedimentary Research*, v. 87, p. 66-74.

Hayes, D.A., Timmer, E.R., Ranger, M.J., Kavanaugh, J.L., and Gingras, M.K. 2018. Using Structure-From-Motion Photogrammetry to Recognize Lateral Versus Forward Accretion Bedforms in the Lower Cretaceous McMurray Formation, NE Alberta, Canada. *Bulletin of Canadian Petroleum Geology*, v. 66, p. 725-751.

Hoffman, T.A. 2008. Lateral Variability of Sedimentological and Ichnological Characteristics of the Falher "D" Member, West-Central Alberta, Canada. M.Sc. Thesis, University of Alberta, Edmonton, 267 p.

Howard, J.D. 1972. Trace fossils as criteria for recognizing shorelines in stratigraphic record. In: Rigby, J.K., Hamblin, W.K. (Eds.). Recognition of Ancient Sedimentary Environments. SEPM, Special Publication, v. 16, p. 215-225.

Howard J.D., Frey R.W. 1975. Estuaries of the Georgia coast, U.S.A.: sedimentology and biology. II. Regional animal-sediment characteristics of Georgia estuaries. *Senckenb Marit*, v. 7, p. 33–103.

Howard J.D., Frey R.W. 1985. Physical and biogenic aspects of backbarrier sedimentary sequences, Georgia coast, U.S.A. *Marine Geology*, v. 63, p. 77–127.

Hunter, R.E., and Clifton, E.H. 1982. Cyclic deposits and hummocky cross-stratification of probable storm origin in Upper Cretaceous rocks of the Cape Sebastian area, southwestern Oregon. *Journal of Sedimentary Research*, v. 52, p. 127-143.

Ichaso, A.A., and Dalrymple, R.W. 2009. Tide- and wave-generated fluid mud deposits in the Tilje Formation (Jurassic), offshore Norway. *Geology*, v. 37, p. 539-542.

Jackson, P.C. 1984. Paleogeography of the Lower Cretaceous Mannville Group of Western Canada. In: Elmworth: Case study of a deep basin gas field, Masters, J.A. (Eds.). American Association of Petroleum Geologists, Memoir 38, p. 49-77.

James, M.R., and Robson, S. 2012. Straightforward reconstruction of 3D surfaces and topography with a camera: Accuracy and geoscience application. *Journal of Geophysical Research*, v. 117, p. 117.

Jelby, M.E., Grundvag, S.A., Helland-Hansen, W., Olaussen, S., and Stemmerik, L. 2020. Tempestite facies variability and storm-depositional processes across a wide ramp: Towards a polygenetic model for hummocky cross-stratification. *Sedimentology*, v. 67, p. 742-781.

Keighley D.G., Pickerill R.K. 1995. The ichnotaxa *Palaeophycus* and *Planolites*: historical perspectives and recommendations. *Ichnos*, v. 3, p. 301–309.

Knaust, D. 2012. Methodology and Techniques. In: Knaust, D., Bromley, R. G. (Eds.). Trace fossils as indicators of sedimentary environments, *Developments in Sedimentology*. Elsevier, v. 64, p. 245-271

Komar, P.D. 1973. Computer models of delta growth due to sediment input from rivers and longshore transport. *Geological Society of America Bulletin*, v. 84, p. 2217-2226.

Lamb, M. P., and Mohrig, D. 2009. Do hyperpycnal-flow deposits record river-flood dynamics?. *Geology*, v. 12, p. 1067-1070.

Leaman, M., and McIlroy, D. 2017. Three-dimensional morphological and permeability modelling of Diplocraterion. *Ichnos*, v. 24, p. 51-63.

Leckie, D.A. 1985b. The Gates Formation (Falher Member), northeastern British Columbia; a wave-dominated strandplain system: outcrop and subsurface. *Canadian Society of Petroleum Geologists Reservoir*, v. 12, p. 1-2.

Leckie, D. 1986. Rates, controls, and sand-body geometries of transgressive-regressive cycles: Cretaceous Moosebar and Gates Formations, British Columbia. *AAPG Bulletin*, v. 70, p. 516-535.

Leckie, D.A. and Smith, D.G. 1992. Regional setting, evolution, and depositional cycles of the western Canada foreland basin. In: *Foreland basins and foldbelts*. R.W. Macqueen and D.A. Leckie (Eds.). American Association of Petroleum Geologists, Memoir 55, p. 9-46.

Leckie, D.A., and Walker, R.G. 1982. Storm- and tide-dominated shorelines in Cretaceous Moosebar-lower Gates interval - outcrop equivalents. *AAPG Bulletin*, v. 66, p. 138-157.

Li, W., Bhattacharya, J.P., and Wang, Y. 2011. Delta asymmetry: Concepts, characteristics, and depositional models. *Petroleum Science*, v. 8, p. 278-289.

Lorenz, J.C. 1982. Lithospheric flexure and the history of the Sweetgrass Arch in northwestern Montana. In: Geological Studies of the Cordilleran Thrust Belt: R.B. Powers (ed.). Rocky Mountain Association of Geologists, Denver, Colorado, p. 77-89.

Löwemark L., Nara M. 2010. Morphology, ethology, and taxonomy of the ichnogenus *Schaubeylindrichnus*: notes for clarification. *Palaeogeography, Palaeoclimatology, Palaeoecology*, v. 297, p. 184-187.

MacDonald, D.E., Langenberg, C.W., and Strobl, R.S. 1988. Cyclic marine sedimentation in the Lower Cretaceous Luscar Group and Spirit River Formation of the Alberta foothills and Deep Basin. In: *Sequences, Stratigraphy, Sedimentology: Surface and Subsurface*, James, D.P., and Leckie, D.A. (Eds.). Canadian Society of Petroleum Geologists 15, p. 143-154.

MacEachern, J.A., and Bann, K.L. 2008. The role of ichnology in refining shallow marine facies models, in Hampson, G.J. Steel, R.J., Burgess, P.M., and Dalrymple R.W. (Eds.). *Recent Advances in Models of Siliciclastic Shallow-Marine Stratigraphy*. SEPM, Society for Sedimentary Geology, v. 90, p. 0.

MacEachern, J.A. and Hobbs, T.W. 2004. The ichnological expression of marine and marginal marine conglomerates and conglomeratic intervals, Cretaceous Western Interior Seaway, Alberta and northeastern British Columbia. *Bulletin of Canadian Petroleum Geology*, v. 52, p.77-104.

MacEachern, J.A., Bann, K.L., Bhattacharya, J.P., Howell, C.D. 2005. Ichnology of deltas: Organism responses to the dynamic interplay of rivers, waves, storms and tides. In: Gioson, L., Bhattacharya, J.P. (Eds.). *River Deltas: Concepts Models and Examples*. SEPM, Special Publication 83, p. 49–85.

MacEachern, J.A., Bann, K.L., Gingras, M.K., Zonneveld, J.-P., Dashtgard, S.E., Pemberton, S.G. 2012. The ichnofacies paradigm, Trace Fossils as Indicators of Sedimentary Environments. In: Knaust, D., Bromley, R.G. (Eds.). *Developments in Sedimentology*: Elsevier 64, p. 103-138.

McAnally, W.H., Friedrichs, C., Hamilton, D., Hayter, E., Shrestha, P., Rodriguez, H., and ASCE Task Committee on Management of Fluid Mud. 2007. Management of fluid mud in estuaries, bays, and lakes. I: Present state of understanding on character and behavior. *Journal of Hydraulic Engineering*, v. 133, p. 9-22.

McLean, J.R. 1977. The Cadomin Formation: stratigraphy, sedimentology, and tectonic implications. *Bulletin of Canadian Petroleum Geology*, v. 25, p. 792-827.

Monger, J.W.H. 1989. Overview of Cordilleran geology. In: *Western Canada Sedimentary Basin: A Case History*. B.D. Ricketts (ed.). Canadian Society of Petroleum Geologists, p. 9-32.

Monger, J., and Price, R. 2002. The Canadian Cordillera: geology and tectonic evolution. *CSEG Recorder*, v. 27, p. 17-36.

Morsilli, M., and Pomar, L. 2012. Internal waves vs. surface storm-waves: A review on the origin of hummocky cross-stratification. *Terra Nova*, v. 24, p. 273-282.

Moslow, T.F. 1998. Reservoir architecture and predictability of shoreface conglomerates in the Deep Basin of Western Canada: insights from outcrop. *Canadian Society of Petroleum Geologists Reservoir*, v. 25, p. 6-7.

Moslow, T.F., and Schink, A. 1995. Reservoir characterization and facies analysis from outcrop exposures: Falher D Member (Lower Cretaceous). *Canadian Society of Petroleum Geologists Reservoir*, v. 22, p. 3-4.

Mulder, T., Syvitski, J.P., Migeon, S., Faugères, J.C., and Savoye, B. 2003. Marine hyperpycnal flows: initiation, behavior, and related deposits. *Marine and Petroleum Geology*, v. 20, p. 861-882.

Mutti, E., Tinterri, R., di Biase, D., Fava, L., Mavilla, N., Angella, S., and Calabrese, L. 2000. Delta-front facies associations of ancient flood-dominated fluvio-deltaic systems. *Revista Sociedad Geologica de España*, v. 13, p. 165-190.

Mutti, E., Tinterri, R., Benevelli, G., di Biase, D. and Cavanna, G. 2003. Deltaic, mixed and turbidite sedimentation of ancient foreland basins. *Marine Petroleum Geology*, v. 20, p. 733-755.

Myrow, P.M. 1992. Bypass-zone tempestite facies model and proximity trends for an ancient muddy shoreline and shelf. *Journal of Sedimentary research*, v. 62, p. 99-115.

Myrow, P.M. 2005. Storms and storm deposits. In: Selley, R.C., Cocks, R., Pilmer, I. (Eds.). *Encyclopedia of Geology*. Elsevier, p. 580-587.

Myrow, P.M., and Southard, J. B. 1991. Combined-flow model for vertical stratification sequences in shallow marine storm-deposited beds. *Journal of Sedimentary Research*, v. 61, p. 202-210.

Myrow, P.M., Lukens, C., Lamb, M.P., Houck, K., and Strauss, J. 2008. Dynamics of a transgressive prodeltaic system: Implications for geography and climate within a Pennsylvanian intracratonic basin, Colorado, U.S.A. *Journal of Sedimentary Research*, v. 78, p. 512-528.

Nara M. 1995. *Rosselia socialis*: a dwelling structure of a probable terebellid polychaete. *Lethaia*, v. 28, p. 171–178.

Nara M. 2006. Reappraisal of *Schaubcylindrichnus*: a probable dwelling/feeding structure of a solitary funnel feeder. *Palaeogeography Palaeoclimatology Palaeoecology*, v. 240, p. 439-452.

Neill, C.F., and Allison, M.A. 2005. Subaqueous deltaic formation on the Atchafalaya Shelf, Louisiana. *Marine Geology*, v. 214, p. 411-430.

Newitt, D. J., and Pedersen, P. K. 2015. Depositional Environments within the Wilrich Member, Spirit River Formation–North Central Alberta. *Geoconvention 2015, New Horizons*, Calgary, Alberta, 2 p.

Newitt, D., and Pedersen, P. K. 2022. Observational Data-Based Sequence Stratigraphy of a Clastic Wedge within an Active Foreland Basin, Spirit River Formation, West-Central Alberta, Canada. SSRN Electronic Journal, p. 1-35.

Nicholson, H.A. 1873. Contributions to the study of the errant annelides of the older Palaeozoic rocks. Proceedings of the Royal Society of London., v. 21, p. 288-290.

Nienhuis, J.H., Ashton, A.D., and Giosan, L. 2015. What makes a delta wave-dominated?. *Geology*, v. 43, p. 511-514.

Nodwell, B.J., and Hart, B S. 2006. Deeply-rooted paleobathymetric control on the deposition of the Falher F conglomerate trend, Wapiti Field, Deep Basin, Alberta. *Bulletin of Canadian Petroleum Geology*, v. 54, p. 1-21.

O'Connell, S.C., Dix, G.R., and Barclay, J.E. 1990. The origin, history, and regional structural development of the Peace River Arch, Western Canada. *Bulletin of Canadian Petroleum Geology*, v. 38A, p. 4-24.

Olariu, C., and Bhattacharya, J.P. 2006. Terminal distributary channels and delta front architecture of river-dominated delta system. *Journal of Sedimentary Research*, v. 76, p. 212-233.

Olariu, C., Steel, R.J., and Petter, A.L. 2010. Delta-front hyperpycnal bed geometry and implications for reservoir modeling: Cretaceous Panther Tongue delta, Book Cliffs, Utah. *AAPG Bulletin*, v. 94, p. 819-845.

Pemberton, S.G., Frey R.W. 1982. Trace fossil nomenclature and the Planolites-Palaeophycus dilemma. *Journal of Paleontology*, v. 56, p. 843–881.

Pemberton, S.G. and MacEachern, J.A. 1997. The ichnological signature of storm deposits: the use of trace fossils in event stratigraphy. In: Brett, C.E. (Eds.). *Paleontological Event Horizons: Ecological and Evolutionary Implications*. Columbia University Press, p.73-109.

Pemberton, S.G., Van Wagoner, J.G., and Wach, G.D. 1992. Ichnofacies of a wave dominated shoreline. In: Pemberton, S.G., eds., Applications of Ichnology to Petroleum Exploration. Society of Economic Paleontologists and Mineralogists, Core Workshop 17, p. 339-382.

Pemberton, S.G., MacEachern, J.A., Gingras, M.K., and Saunders, T.D.A. 2008. Biogenic chaos: Cryptobioturbation and the work of sedimentologically friendly organisms. *Palaeogeography, Palaeoclimatology, Palaeoecology*, v. 270, p. 273-279.

Pemberton, S.G., MacEachern, J.A., Dashtgard, S.E. et al. 2012. Shorefaces. In: Knaust D, Bromley R.G. (Eds.). Trace fossils as indicators of sedimentary environments: Developments in Sedimentology, v. 64, p. 563-604.

Petter, A.L. and Steel, R.J. 2006. Hyperpynal flow variability and slope organization on an Eocene shelf margin, Central Basin, Spitsbergen. *AAPG Bulletin*, v. 90, p. 1451-1472.

Plint, A.G. 1988. Sharp-based shoreface sequences and “offshore bars” in the Cardium Formation of Alberta; their relationship to relative changes in sea level. In: Wilgus, C.K., Hastings, B.S., Kendall, C.G.S.C., Posamentier, H.W., Ross, C.A., Van Wagoner, J.C. (Eds.). *Sea Level Changes—An Integrated Approach*. SEPM, Special Publication 42, p. 357-370.

Plink-Bjorklund, P. and Steel, R.J. 2004. Initiation of turbidity currents: outcrop evidence for Eocene hyperpynal-flow turbidites. *Sedimentary Geology*, v. 165, p. 29-52.

Price, R.A. 1981. The Cordilleran Thrust and Fold Belt in the southern Canadian Rocky Mountains. In: Thrust and nappe tectonics. McClay, K.R. and Price, N.J. (Eds.). Geological Society of London, Special Publication no. 9, p. 427-448.

Podruski, J.A. 1988. Contrasting character of the Peace River and Sweetgrass arches, Western Canada Sedimentary Basin. *Geoscience Canada*, v. 15, p. 94-97.

Porter, J.W., Price, R.A. and McCrossan, R.G. 1982. The Western Canadian Sedimentary Basin. *Philosophical Transactions of the Royal Society of London Series A*, v. 305, no. 1489, p. 169–192.

Reading, H.G., and Collinson, J.D. 1996. Clastic coasts. In: Reading, H.G. (Eds.). *Sedimentary Environments: Processes, Facies and Stratigraphy*, Third Edition: Oxford, U.K., Blackwell Science, p. 154-231.

Saunders, T.D.A., MacEachern, J.A., Pemberton, S.G. 1994. Cadotte Member Sandstone: progradation in a boreal basin prone to winter storms. In: Pemberton, S.G., James, D.P., Wightman, D.M. (Eds.). *Mannville Core Conference*. Canadian Society of Petroleum Geologists, p. 331–350.

Schmidt, G.A., and Pemberton, S.G. 2004. Stratigraphy and palaeogeography of a conglomeratic shoreline: The Notikewin Member of the Spirit River Formation in the Wapiti area of west-central Alberta. *Bulletin of Canadian Petroleum Geology*, v. 52, p. 57-76.

Schultheis, N.H., and Mountjoy, E.W. 1978. Cadomin conglomerate of western Alberta—a result of early Cretaceous uplift of the Main Ranges. *Bulletin of Canadian Petroleum Geology*, v. 26, p. 297-342.

Seike, K. 2007. Palaeoenvironmental and palaeogeographical implications of modern *Macaronichnus segregatis*-like traces in foreshore sediments on the Pacific coast of central Japan. *Palaeogeography, Palaeoclimatology, Palaeoecology*, v. 252, p. 497-502.

Seilacher A. 1955. Spuren und Fazies im Unterkambrium. In: Schindewolf OH, Seilacher A. (Eds.). *Beiträge zur Kenntnis des Kambriums in der Salt Range (Pakistan)*. Akademie der Wissenschaften und der Literatur zu Mainz, Abhandlung Mathematisch - Naturwissenschaftliche Klasse, p. 373–399.

Seitz, S.M., Curless, B., Diebel, J., Scharstein, D., and Szeliski, R. 2006. A comparison and evaluation of multi-view stereo reconstruction algorithms. *Proceedings of the IEEE Computer Society Conference on Computer Vision and Pattern Recognition*, v. 1, p. 519-526.

Smith, D.G., Zorn, C.E., Sneider, R.M. 1984. The palaeogeography of the Lower Cretaceous of Western Alberta and Northeastern British Columbia in and adjacent to the Deep Basin of the Elmworth area. In: Masters, J.A. (Eds.). *Elmworth - Case Study of a Deep Basin Gas Field*. AAPG Memoir, v. 38, p. 79-114.

Snavely, N., Seitz, S. M., and Szeliski, R. 2008. Modeling the world from internet photo collections. *International Journal of Computer Vision*, v. 80, p. 189-210.

Stelck, C.R., and Kramers, J.W. 1980. Frobaldiceras from the Grand Rapids Formation of north-central Alberta. *Bulletin of Canadian Petroleum Geology*, v. 28, p. 509-521.

Stott, D.F. 1968. Lower Cretaceous Bullhead and Fort St. John Groups between Smoky and Peace Rivers, Rocky Mountain Foothills, Alberta and British Columbia. *Geological Survey of Canada, Bulletin*, p. 152-279.

Stott, D.F. 1973. Lower Cretaceous Bullhead Group between Bullmoose Mountain and Tetsa River, Rocky Mountain Foothills, northeastern British Columbia. *Geological Survey of Canada Bulletin*, v. 219, p. 219-228.

Tavani, S., Granado, P., Corradetti, A., Girundo, M., Iannace, A., Arbués, P., Muñoz, J. A., and Mazzoli, S. 2014. Building a virtual outcrop, extracting geological information from it, and sharing the results in Google Earth via OpenPlot and Photoscan: An example from the Khaviz Anticline (Iran). *Computers and Geosciences*, v. 63, p. 44-53.

Taylor, A., Goldring, R., and Gowland, S. 2003. Analysis and application of ichnofabrics. *Earth-Science Reviews*, v. 60, p. 227-259.

Todd, T.W. 1968. Dynamic diversion; influence of longshore current-tidal flow interaction on chenier and barrier island plains. *Journal of Sedimentary Research*, v. 38, p. 734-746.

Torell O. 1870. Petrificata suecana formationis Cambricæ. *Lunds Universitets Årsskrift 6. Afdelningen*, v. 8, p. 1–14.

Uchman A., Rattazzi B. 2016. *Rhizocorallium hamatum* (Fischer- Ooster 1858), a Zoophycos-like trace fossil from deep-sea Cretaceous-Neogene sediments. *Historical Biology*, v. 3, p. 395-410.

Ullman, S. 1979. The Interpretation of Structure from Motion. Proceedings of the Royal Society of London. Series B, Biological Sciences, v. 203, p. 405-426.

Umeorah, E.M. 1987. Depositional environment and facies relationships of the Cretaceous ironstone of the Agbaja Plateau, Nigeria. Journal of African Earth Sciences, v. 6, p. 385-390.

Vossler, S.M., and Pemberton, S.G. 1988. *Skolithos* in The Upper Cretaceous Cardium Formation: An Ichnofossil Example of Opportunistic Ecology. Lethaia, v. 21, p. 351-362.

Vossler, S.M., and Pemberton, S.G. 1989. Ichnology and paleoecology of offshore siliciclastic deposits in the Cardium Formation (Turonian, Alberta, Canada). Palaeogeography, Palaeoclimatology, Palaeoecology, v. 74, p. 217-239.

Yang, B., Dalrymple, R. W., & Chun, S. 2006. The significance of hummocky cross-stratification (HCS) wavelengths: evidence from an open-coast tidal flat, South Korea. Journal of Sedimentary Research, 76(1), 2-8.

Wadsworth, J., Boyd, R., Diessel, C., and Leckie, D. 2003. Stratigraphic style of coal and non-marine strata in a high accommodation setting: Falher Member and Gates Formation (Lower Cretaceous), western Canada. Bulletin of Canadian Petroleum Geology, v. 51, p. 275-303.

Walker, R.G., Duke, W.L., and Leckie, D.A. 1983. Hummocky stratification: Significance of its variable bedding sequences. Bulletin of the Geological Society of America, v. 94, p. 1245-1249.

Weise, B.R. 1980. Wave-dominated deltaic systems of the Upper Cretaceous San Miguel Formation, Maverick Basin, South Texas: Austin, Texas. Texas Bureau of Economic Geology, Report of Investigations, v. 107, p. 39.

Westoby, M.J., Brasington, J., Glasser, N.F., Hambrey, M.J., and Reynolds, J.M. 2012. "Structure-from-Motion" photogrammetry: A low-cost, effective tool for geoscience applications. Geomorphology, v. 179, p. 300-314.

Williams, G. D., and Stelck, C. R. 1975. Speculations on the Cretaceous palaeogeography of North America. In: Caldwell, W. G. E. (Eds.). The Cretaceous System in the western interior of North America. The Geological Association of Canada Special Paper 13, p. 1-20.

Woodcock, N.H. 1977. Specification of fabric shapes using an eigenvalue method. Geological Society of America Bulletin, v. 88, p. 1231-1236.

Wright, G.N., McMechan, M.E., Potter, D.E.G., Mossop, G.D., and Shetsen, I. 1994. Structure and architecture of the Western Canada sedimentary basin. Geological Atlas of the Western Canada Sedimentary Basin, v. 4, p. 25-40.

Yang, R., Jin, Z., Sun, D., Han, Z., and Fan, A. 2015. Coexistence of Hyperpycnites, Debrisites and Turbidites and Their Geological Significances of Unconventional Petroleum. Acta Geologica Sinica - English Edition, v. 89, p. 117-119.

Zavala, C., Arcuri, M. and Blanco Valiente, L. 2012a. The importance of plant remains as a diagnostic criteria for the recognition of ancient hyperpycnites. Paleobiology, v. 11, p. 457-469.

Zavala, C., Arcuri, M. and Valiente, L.B. 2012b. Plant remains in recent deposits of the Orinoco fan: a direct evidence of hyperpycnal discharges of the Orinoco River. In: GSTT 5th Geological Conference, p. 3-5.

Zenker J.C. 1836. Historisch-topographisches Taschenbuch von Jena und seiner Umgebung. Friedrich Frommann, Jena, p. 338.

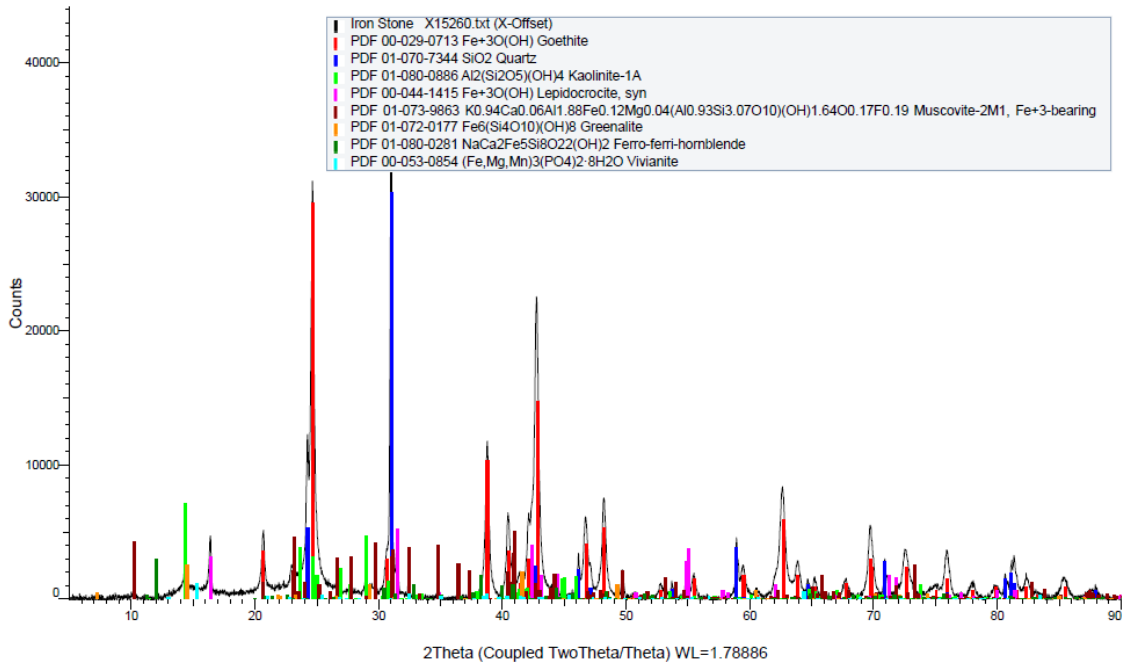
Zavala, C., Arcuri, M., Di Meglio, M., Zorzano, A., Otharan, G., Irastorza, A., and Torresi, A. 2021. Deltas: a new classification expanding Bates's concepts. Journal of Palaeogeography, v. 10, p. 1-15.

Zonneveld, J-P., and Moslow, T.F. 2004. Exploration potential of the father G shoreface conglomerate trend: Evidence from outcrop. Bulletin of Canadian Petroleum Geology, v. 52, p. 23-38.

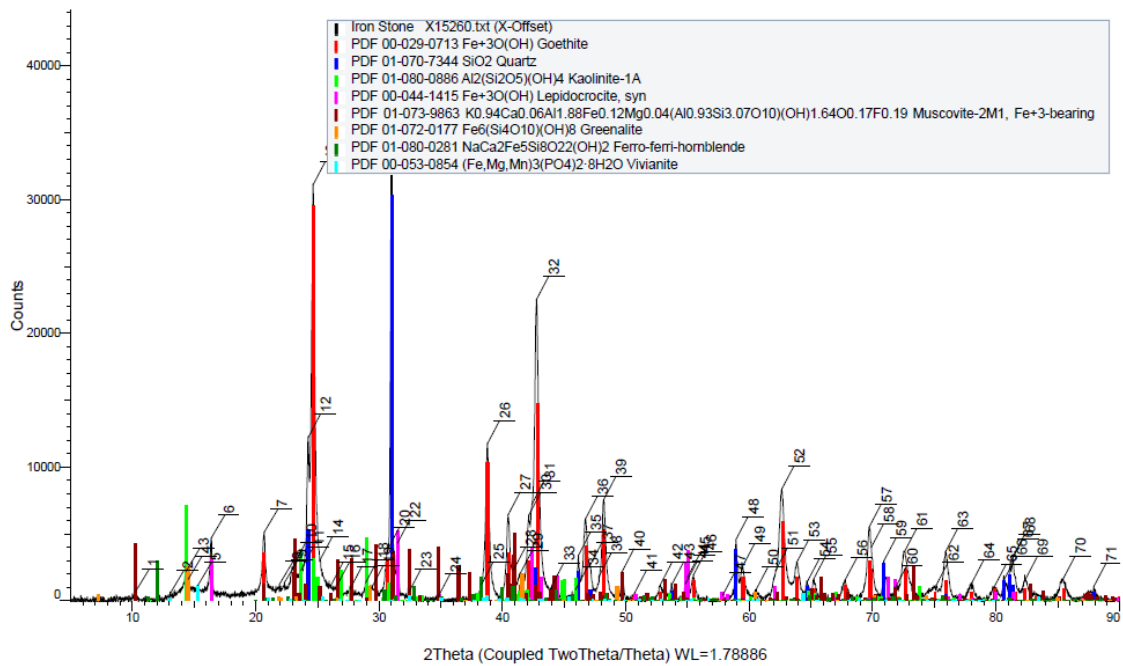
Zonneveld, J-P., Tisdale, D. and Legault, F. 2017. Analysis of contrasting adjacent tight sand reservoirs: the Falher F and Falher G (upper Wilrich) sandstone successions in the Kakwa region, Alberta. CSPG Core Conference, Abstract, p. 50–53.

APPENDIX I: X-RAY DIFFRACTION RESULTS – IRONSTONE

(Coupled TwoTheta/Theta)



(Coupled TwoTheta/Theta)



Peak List #1

Visible	Index	Angle	d Value	Intensity	Net Intensity	Rel. Intensity	FWHM
Yes	1	10.258 °	10.00455 Å	653.112	653	1.6%	0.331
Yes	2	13.069 °	7.85969 Å	546.890	547	1.4%	0.344
Yes	3	14.356 °	7.15810 Å	2199.663	2200	5.5%	0.450
Yes	4	14.529 °	7.07329 Å	1591.920	1592	4.0%	0.450
Yes	5	15.313 °	6.71336 Å	1137.276	1137	2.8%	0.444
Yes	6	16.404 °	6.26951 Å	4694.571	4695	11.7%	0.199
Yes	7	20.687 °	4.98159 Å	5100.411	5100	12.8%	0.244
Yes	8	21.936 °	4.70115 Å	1224.913	1225	3.1%	0.281
Yes	9	22.336 °	4.61789 Å	1344.459	1344	3.4%	0.277
Yes	10	23.091 °	4.46898 Å	2657.414	2657	6.6%	0.544
Yes	11	23.685 °	4.35840 Å	2264.003	2264	5.7%	0.160
Yes	12	24.268 °	4.25516 Å	12214.040	12214	30.5%	0.160
Yes	13	24.661 °	4.18833 Å	31109.990	31110	77.8%	0.289
Yes	14	25.232 °	4.09510 Å	3060.281	3060	7.7%	0.160
Yes	15	26.104 °	3.96053 Å	1150.812	1151	2.9%	0.308
Yes	16	26.618 °	3.88541 Å	1166.579	1167	2.9%	0.375
Yes	17	27.654 °	3.74258 Å	858.239	858	2.1%	0.300
Yes	18	28.916 °	3.58241 Å	1330.862	1331	3.3%	0.297
Yes	19	29.388 °	3.52616 Å	925.496	925	2.3%	0.402
Yes	20	30.652 °	3.38403 Å	3733.155	3733	9.3%	0.160
Yes	21	31.017 °	3.34518 Å	39997.970	39998	100.0%	0.157
Yes	22	31.494 °	3.29570 Å	4297.210	4297	10.7%	0.189
Yes	23	32.415 °	3.20455 Å	617.839	618	1.5%	0.110
Yes	24	34.784 °	2.99235 Å	294.085	294	0.7%	0.237
Yes	25	38.282 °	2.72784 Å	1191.813	1192	3.0%	0.160
Yes	26	38.788 °	2.69354 Å	11742.960	11743	29.4%	0.301
Yes	27	40.457 °	2.58685 Å	6400.986	6401	16.0%	0.288
Yes	28	40.888 °	2.56070 Å	2274.419	2274	5.7%	0.160
Yes	29	41.439 °	2.52811 Å	2036.809	2037	5.1%	0.381
Yes	30	42.133 °	2.48834 Å	6382.548	6383	16.0%	0.160
Yes	31	42.408 °	2.47292 Å	7242.851	7243	18.1%	0.160
Yes	32	42.763 °	2.45336 Å	22512.520	22513	56.3%	0.344
Yes	33	43.993 °	2.38799 Å	1091.044	1091	2.7%	0.262
Yes	34	45.936 °	2.29213 Å	810.193	810	2.0%	0.247
Yes	35	46.153 °	2.28193 Å	3382.751	3383	8.5%	0.199
Yes	36	46.721 °	2.25575 Å	6089.158	6089	15.2%	0.360
Yes	37	47.109 °	2.23822 Å	2658.425	2658	6.6%	0.160
Yes	38	47.858 °	2.20519 Å	1854.170	1854	4.6%	0.160
Yes	39	48.194 °	2.19071 Å	7526.874	7527	18.8%	0.320
Yes	40	49.691 °	2.12873 Å	2159.697	2160	5.4%	0.192
Yes	41	50.696 °	2.08924 Å	542.255	542	1.4%	0.321
Yes	42	52.797 °	2.01171 Å	1179.450	1179	2.9%	0.334
Yes	43	53.735 °	1.97913 Å	1206.044	1206	3.0%	0.219
Yes	44	54.835 °	1.94244 Å	1257.016	1257	3.1%	0.358
Yes	45	54.986 °	1.93751 Å	1726.951	1727	4.3%	0.358
Yes	46	55.488 °	1.92135 Å	1918.917	1919	4.8%	0.311

Yes	47	57.859 °	1.84903 Å	395.731	396	1.0%	0.186
Yes	48	58.935 °	1.81821 Å	4557.052	4557	11.4%	0.218
Yes	49	59.449 °	1.80392 Å	2529.672	2530	6.3%	0.381
Yes	50	60.533 °	1.77457 Å	776.259	776	1.9%	0.272
Yes	51	62.138 °	1.73317 Å	2234.514	2235	5.6%	0.160
Yes	52	62.652 °	1.72036 Å	8352.954	8353	20.9%	0.417
Yes	53	63.857 °	1.69125 Å	2845.328	2845	7.1%	0.396
Yes	54	64.713 °	1.67125 Å	1424.734	1425	3.6%	0.269
Yes	55	65.256 °	1.65887 Å	1657.869	1658	4.1%	0.237
Yes	56	67.739 °	1.60492 Å	1475.784	1476	3.7%	0.345
Yes	57	69.730 °	1.56466 Å	5488.578	5489	13.7%	0.372
Yes	58	69.904 °	1.56127 Å	3986.316	3986	10.0%	0.372
Yes	59	70.910 °	1.54195 Å	2950.150	2950	7.4%	0.193
Yes	60	71.802 °	1.52532 Å	890.474	890	2.2%	0.273
Yes	61	72.595 °	1.51092 Å	3684.787	3685	9.2%	0.452
Yes	62	75.152 °	1.46673 Å	1139.934	1140	2.8%	0.502
Yes	63	75.916 °	1.45416 Å	3653.358	3653	9.1%	0.353
Yes	64	78.031 °	1.42079 Å	1300.111	1300	3.3%	0.357
Yes	65	79.860 °	1.39352 Å	1017.642	1018	2.5%	0.393
Yes	66	80.682 °	1.38171 Å	1589.281	1589	4.0%	0.288
Yes	67	81.170 °	1.37483 Å	2853.976	2854	7.1%	0.410
Yes	68	81.358 °	1.37221 Å	3233.470	3233	8.1%	0.383
Yes	69	82.381 °	1.35816 Å	1571.996	1572	3.9%	0.275
Yes	70	85.440 °	1.31841 Å	1618.049	1618	4.0%	0.413
Yes	71	87.933 °	1.28837 Å	1053.106	1053	2.6%	0.190

**APPENDIX II: ORIENTATION MEASUREMENTS M&K
VALUES**

Pointfile (Master Bedding)	DIP	DDIR	M	K
5.MB_W5_B.txt	3.5	272	9.25	0.52
5.MB_W1_N.txt	2.9	292.6	9.22	0.16
5.MB_W5_C.txt	6.7	282.4	16	0.66
5.MB_W2_D.txt	3.5	296.5	17.84	0.54
8.MB_E2_R.txt	3.9	294.1	10.22	1.67
9.MB_W1_U.txt	3.5	329	14.66	0.77
9.MB_W1_L.txt	1.6	351.3	16.04	0.89
5.MB_W1_F.txt	1.5	321.3	9.35	0.38
5.MB_W1_S.txt	2.7	327.1	10.2	0.42
5.MB_W1_Y.txt	1.8	316.1	9.83	0.37
2.MB_E1_X.txt	5.2	291.6	7.41	0.68
5.MB_W5_I.txt	5.6	281.4	9.42	0.29
2.MB_E1_Y.txt	3.5	289.3	7.87	0.33
5.MB_W3_F.txt	3.7	279.9	11.35	0.39
1.MB_W5_C.txt	7.6	327.7	6.69	0.59
732.MB_W1_V	2	345.4	9.41	0.96
1.MB_W4_Z.txt	3.7	282.3	9.99	0.82
MB_E1_T.txt	2.5	277.4	13.96	0.8
11.MB_W1_H.txt	6.6	281.1	11.66	0.82
5.MB_W5_K.txt	2.1	302.4	8.77	0.49
5.MB_W2_N.txt	2.7	280.8	9.53	0.29
9.MB_W3_S.txt	3.9	271.1	9.09	1
12.MB_W1_J.txt	1.1	279.9	9.94	0.68
5.MB_W6_B.txt	0.4	327.7	11.82	0.36
5.MB_W7_C.txt	0.7	284.2	8.3	0.61
5.MB_W6_L.txt	2.7	298.4	12.74	0.17
13.MB_W1_L.txt	2.7	298.4	12.74	0.17
5.MB_W6_A.txt	4.5	317.6	7.98	0.6
12.MB_W2_J.txt	3.3	342	8.65	2.6
13.MB_W1_A.txt	3.8	307.5	8.3	2.6
4.MB_W1_P	4.6	311.4	9.33	0.6
2.MB_E3_M.txt	2.2	311	7.08	0.6
1.MB_W11_Z.txt	3.2	270.3	9.35	0.62
5.MB_W6_X.txt	0.8	317.7	10.82	0.45
1.MB_W9_J.txt	3.2	274.6	7.54	0.49
1.MB_W8_Z.txt	5.3	263.5	8.35	0.99
1.MB_W8_I.txt	5.2	286.2	41.68	0.09
2.MB_E3_E.txt	2.4	285.4	8.94	0.94
3.MB_W2_G.txt	1.4	277	9.63	0.59
4.MB_W2_A.txt	1.9	277.7	9.5	1.19
4.MB_W2_B.txt	0.4	334.7	11.17	0.35
3.MB_W2_F.txt	2.8	284.5	8.35	0.73

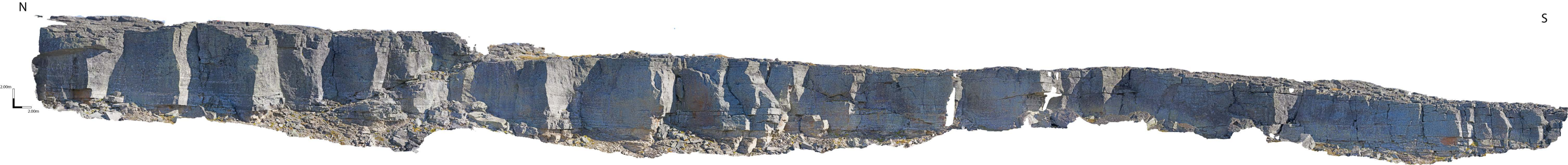
2.MB_E4_I.txt	2.6	300.5	9.96	0.56
12.MB_W2_O.txt	3.6	287.1	12.97	1.15
12.MB_W2_L.txt	3.6	349.8	13.16	0.37
732.MB_W2_D	2.4	265.7	7.6	0.68
4.MB_W2_E.txt	1.3	287	10.45	0.31
1.MB_S11_H.txt	3	237.1	8.63	0.75
1.MB_S11_L.txt	4.1	302.9	6.95	0.54
1.MB_S11_N.txt	3.9	299.1	8.79	0.79
1.MB_S14_Z.txt	6	274.3	8.77	0.33
1.MB_S2_A.txt	4.4	230.1	41.3	0.04
1.MB_S3_R.txt	2.3	180.2	10.22	0.92
1.MB_S3_XX.txt	2.6	240.4	7.92	0.9
1.MB_S4_C.txt	4.6	262.8	9.97	0.73
1.MB_S4_G.txt	3.2	4.8	6.64	1.59
1.MB_S4_R.txt	5	292.5	6.93	0.17
1.MB_S5_B.txt	1.3	298.5	7.04	0.83
1.MB_S5_E.txt	1.5	309.5	9.12	0.67
1.MB_S5_F.txt	4.2	279.9	7.97	0.47
1.MB_S5_I.txt	8.8	268.6	9	1.04
1.MB_S6_H.txt	1.9	286.5	8.14	0.36
1.MB_S6_K.txt	6.7	310.4	6.7	0.32
1.MB_S6_R.txt	5.1	284.5	7.61	0.41
1.MB_S8_XX.txt	4.4	280	8.93	0.54
1.MB_S9_D.txt	2.8	317.8	7.83	0.61
2.MB_S3_G.txt	7.8	288.2	10.87	0.7
2.MB_S3_O.txt	3.3	307	9.44	0.83
2.MB_S3_Z.txt	2.5	318.1	16.29	2.46
2.MB_S2_E.txt	4.1	284.6	9.8	0.83
2.MB_S2_Z.txt	1.6	264.1	12.56	0.81
3.MB_S1_H.txt	6.1	283.5	8.06	0.84
3.MB_S3_D.txt	4.3	333.8	7.46	2
4.MB_S8_B.txt	7.8	326.9	9.52	0.07
4.MB_S15_C.txt	5.3	281.3	8.02	0.22
4.MB_S30_B.txt	5.9	302.1	6.4	-3.64
5.MB_S1_L.txt	3.6	263.6	9.48	1.53
5.MB_S3_E.txt	1.2	319.3	10.02	1.04
5.MB_S1_W.txt	4.5	338.7	8.77	1.43
6.MB_S1_H.txt	6.1	283.5	8.06	0.84
MB_E3_S.txt	3.2	351.9	9.42	0.8
MB_E11_E.txt	2.8	349.1	7.21	1.28
MB_E20_G.txt	1.4	334.9	44.65	0.06
MB_E18_I.txt	4.7	331.2	10.06	0.57
MB_E6_P.txt	2.6	322.2	7.46	0.42

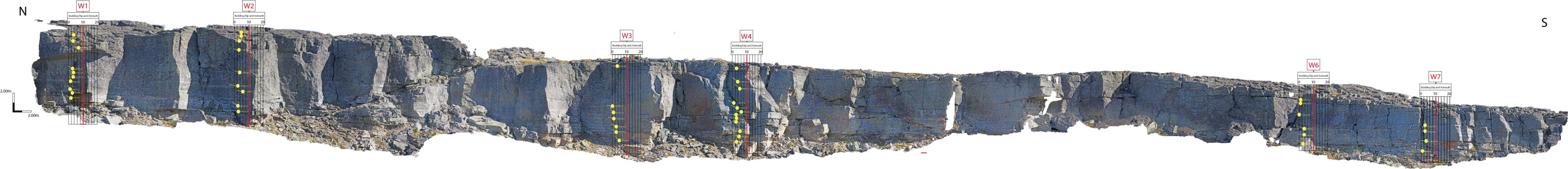
MB_E19_F.txt	6.2	304.5	7.6	0.54
MB_E16_E.txt	1.2	299.8	9.21	0.31
MB_E10_L.txt	4.2	291.6	9.47	0.64
MB_E17_B.txt	2.3	291.2	9.84	0.53
MB_E19_E.txt	5.1	274.5	12.48	0.44
MB_E10_S.txt	4.5	264.4	10.33	0.58
MB_E24_A.txt	1.5	263.3	10.03	0.45
MB_E21_B.txt	2.4	161.6	7.83	1.15
MB_E14_L.txt	2.7	161	7.4	1.36
MB_E12_A.txt	3.9	141.9	7.45	2.27
MB_E4_G.txt	2.7	141.1	7.42	0.79
MB_E1_N.txt	5	139.4	7.89	0.46
MB_E2_G.txt	6	130.3	6.23	0.13
MB_E3_K.txt	3.1	125.8	9.32	0.7
MB_E9_K.txt	1.5	124.6	7.97	0.71
MB_E6_F.txt	3.9	124.3	7.03	0.32
MB_E4_A.txt	4.5	124	11.36	0.42
MB_E3_E.txt	4.2	123.7	9.07	1.67
MB_E14_G.txt	3.3	121.1	7	1.61
MB_E5_B.txt	5.9	116.4	8.85	0.73
MB_E6_A.txt	2.6	113.1	8.88	0.76
MB_E7_C.txt	3.3	110.1	8.42	0.68
MB_E1_F.txt	3.7	109.6	8.32	0.61
MB_E8_C.txt	3.8	109.3	6.48	0.35
MB_E7_G.txt	2.1	107.8	8.83	0.78
MB_E18_L.txt	5.4	29.5	8.4	0.91
MB_E19_B.txt	1.3	19	7.19	1.51
1.MB_E11_S	5.8	317.7	8.46	0.59
1.MB_E11_R	2.2	357.5	9.76	0.71
1.MB_E11_H	1.5	312.2	8.35	0.35
MB_E18_I.txt	4.7	331.2	10.06	0.57

Pointfile (Foreset Laminae)	DIP	DDIR	M	K
CB_S1	6.5	330.6	4.86	-0.88
CB_S2	12	219.3	40.13	0.03
CB_S3	21.6	240.1	38.53	0.11
CB_S4	8.9	260.6	6.29	0.24
CB_S5	14.6	240	8.54	0.29
CB_S6	21.5	255.1	5.67	0.29
CB_S7	16.9	259.4	7.14	0.42
CB_S8	16.3	244.4	7.83	0.42

CB_S9	16.8	264.1	6.09	0.56
CB_S10	7.1	223.5	6.74	0.64
CB_S11	7.2	221.9	6.97	0.64
CB_S12	17.7	267.7	9.26	0.7
CB_S13	11.1	256.6	8.99	0.71
CB_S14	15.8	322.8	7.86	0.94
CB_S15	15.7	276.4	6.88	0.97
CB_E1	28	110.2	3.79	0.45
CB_E2	32.4	105.4	5.35	0.56
CB_E3	29.5	96.8	3.34	0.92
CB_E4	26.5	111.6	4.51	0.91
CB_E5	26.2	135.9	6.37	1.01
CB_E6	26.9	93.2	7.45	0.47
CB_W1	59.2	25.4	8.11	0.32
CB_W2	54.7	31.4	4.32	0.79
CB_W3	78.3	27.7	4.18	1.16
CB_W4	25.8	124.4	37.89	0.05
CB_W5	18.1	83.4	5.41	1.01
CB_W6	20.1	63.3	5.54	0.31
CB_W7	87.8	27.8	6.29	1.64
CB_W8	21.4	101.6	12.46	0.23
CB_W9	22	90	38.39	0.07
CB_W10	23.5	124.6	6.31	1.61
CB_W11	25.8	48.1	4.65	0.83
CB_W12	26	89.5	7.79	0.86
CB_W13	30.3	88.6	17.18	0.27
CB_W14	30.6	85.6	4.33	1.19
CB_W15	30.7	72.9	2.52	-1.7
CB_W16	30.9	85.8	4.06	1.38
CB_W17	31.2	76.3	2.51	-1.42
CB_W18	32.5	91.6	2.6	-1.29
CB_W19	34	62.6	1.94	-1.35
CB_W20	34.1	87.4	2.66	-1.65
CB_W21	34.5	76.2	38.52	0.08
CB_W22	35	96.9	2.37	0.88
CB_W23	36.5	97	2.39	-1.17
CB_W24	39.8	77.4	3.93	-5.11

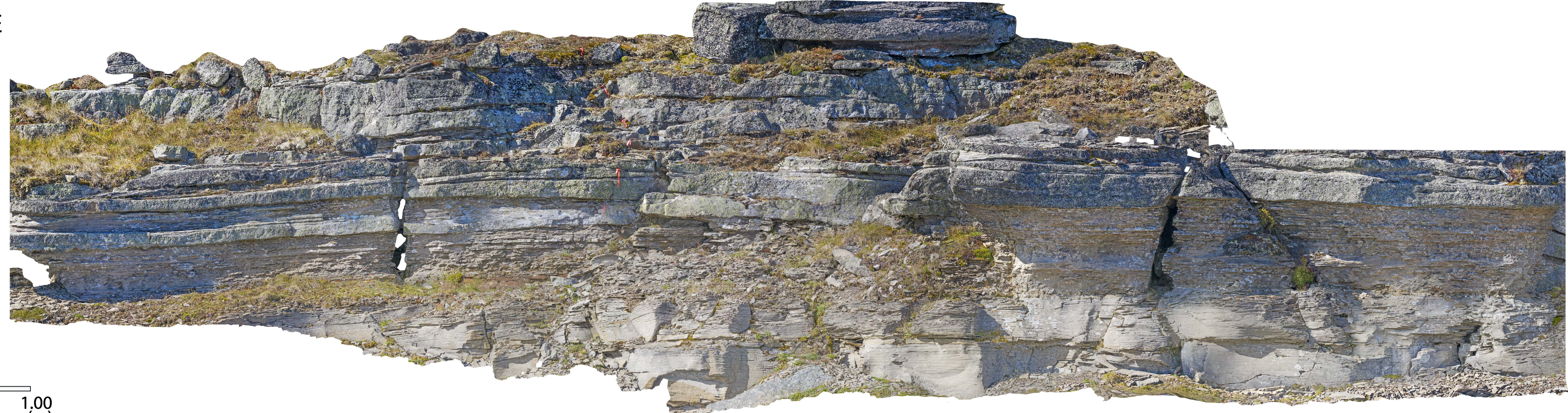
APPENDIX III: PHOTOMOSAICS





E

W

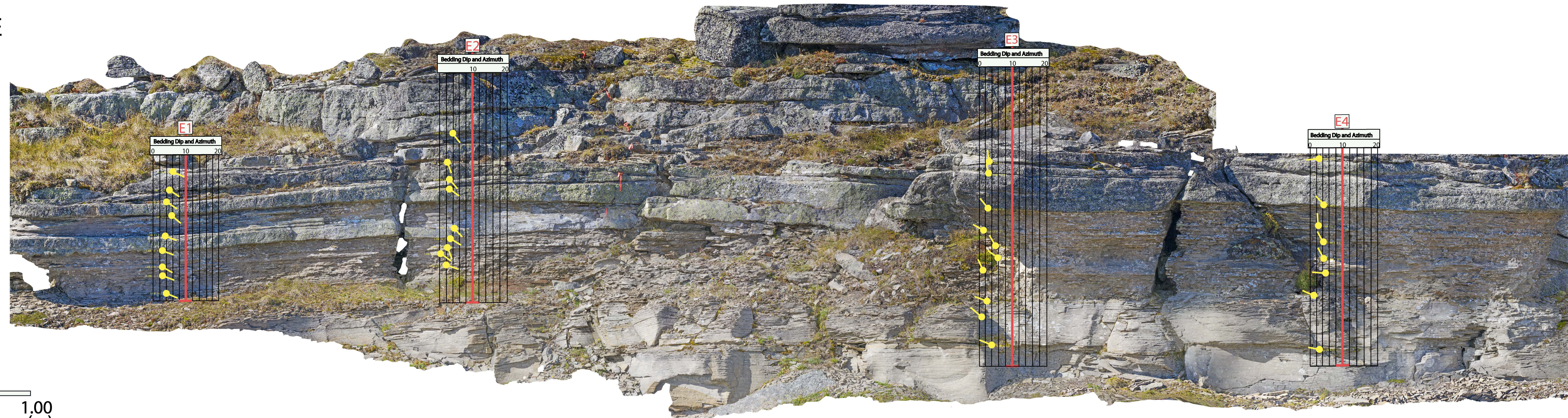


1.00
(m)

1.00
(m)

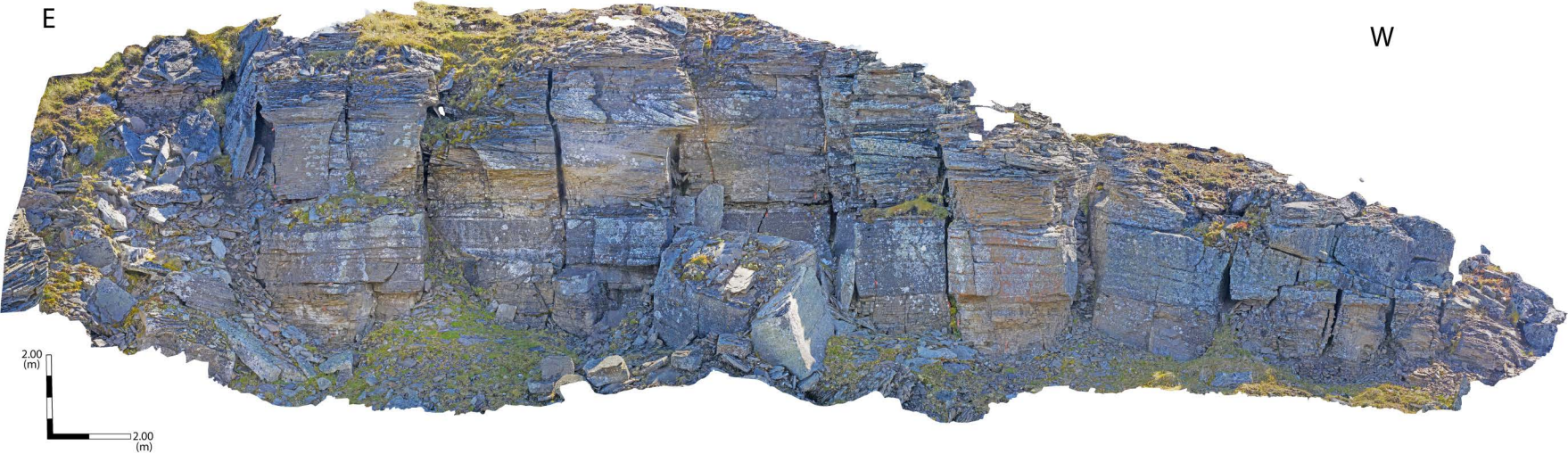
E

W



1.00
(m)

1.00
(m)



E

W

2.00
(m)

2.00
(m)

